Broadening the Frequency Bandwidth of Piezoelectric Energy Harvesters Using Coupled Linear Resonators

by

Soheil Sadeqi

B.Sc., University of Tehran, 2011

Thesis Submitted In Partial Fulfillment of the
Requirements for the Degree of
Master of Applied Science

in the
School of Engineering Science
Faculty of Applied Science

SIMON FRASER UNIVERSITY

Spring 2013

Approval

Name: **Soheil Sadeqi**

Degree: **Master of Applied Science**

Title of Thesis: ***Broadening the Frequency Bandwidth of Piezoelectric Energy Harvesters Using Coupled Linear Resonators***

Examining Committee: **Chair:** Dr. Ahmad Rad
Professor

Dr. Siamak Arzanpour
Senior Supervisor
Assistant Professor, P. Eng _____

Dr. Farid Golnaraghi
Supervisor
Professor _____

Dr. Mehrdad Moallem
Internal Examiner
Professor _____

Date Defended/Approved: April 3, 2013

Partial Copyright Licence

Abstract

The desire to reduce power consumption of current integrated circuits has led design engineers to focus on harvesting energy from free ambient sources such as vibrations. The energy harvested this way can eliminate the need for battery replacement, particularly, in low-energy remote sensing and wireless devices. Currently, most vibration-based energy harvesters are designed as linear resonators, therefore, they have a narrow resonance frequency. The optimal performance of such harvesters is achieved only when their resonance frequency is matched with the ambient excitation. In practice, however, a slight shift of the excitation frequency will cause a dramatic reduction in their performance. In the majority of cases, the ambient vibrations are totally random with their energy distributed over a wide frequency spectrum. Thus, developing techniques to extend the bandwidth of vibration-based energy harvesters has become an important field of research in energy harvesting systems.

This thesis first reviews the broadband vibration-based energy harvesting techniques currently known in some detail with regard to their merits and applicability under different circumstances. After that, the design, fabrication, modeling and characterization of three new piezoelectric-based energy harvesting mechanism, built typically for rotary motion applications, is discussed. A step-by-step procedure is followed in order to broaden the bandwidth of such energy harvesters by introducing a coupled spring-mass system attached to a PZT beam undergoing rotary motion. It is shown that the new strategies can indeed give rise to a wide-band frequency response making it possible to fine-tune their dynamical response. The numerical results are shown to be in good agreement with the experimental data as far as the frequency response is concerned.

Keywords: Energy harvesting, band width extension, rotary motion, piezoelectric beam, power output, wireless sensor, tire pressure monitoring systems.

Acknowledgements

Foremost, I would like to express my sincerest gratitude to my senior supervisor Prof. S. Arzanpour for his continuous support, patience, motivation, enthusiasm, and immense knowledge in the course of this work. His kind advice and guidance during my studies have been invaluable to me. Above all, I would like to thank my supervisor for teaching me how to think and how to become an independent intellectual in research and in everyday life. It has been my greatest honor and pleasure having had the chance to collaborate with Prof. Arzanpour. I would also like to thank Dr. Golnaraghi and Dr. Moallem for kindly reviewing the thesis.

I would also like to thank my fellow friends and roommates whom also happened to be my labmates, Hossein Dehghani and Arash Tavassoli, for all those stimulating discussions, for all those unforgettable times we shared, and for all those memorable times we had together. My utmost gratitude also goes to Mehran Ahmadi, Maryam Yazdanpour, Fattaneh Nadimi, and specially Dordaneh Esfandiari, who have made my life in Vancouver a beautiful and meaningful one. I also would like to thank my friends Kambiz Hajikolaei and Amir Maravandi for sharing their ideas with me during my research activities. All the people who participated in my study were generous with their time in a way that I can never repay.

Last but not least, I would like to thank my loving parents and also my charming little sister, Pardis, for their constant support and encouragement during my studies. I would like to give my sincerest thanks to my father for his belief in me, and his never-ending advice and guidance. I am honourably dedicating this thesis to my loving mother for all her pure blessings and all those sleepless nights she went through because of me over and over.

It is true that I went through several hardships and distractions in the course of finishing my thesis work, but I have reached to the conclusion that they were not so unfortunate as they have made me a stronger and more tolerable person.

Table of Contents

List of Tables

List of Figures

1. Introduction

Tires are an essential part of all wheeled vehicles. They meet different purposes chief among them is the vehicle's safety and efficiency. The inflation pressure of a tire plays a crucial role in dictating its dynamic behaviour. Key factors like braking distance and lateral stability require the inflation pressure to be adjusted and kept in the range as specified by the vehicle's manufacturer. Extreme under-inflation (caused, say, by accidental puncture) can lead to severe thermal and mechanical overload with a subsequent, sudden destruction of the tire. On the other hand, fuel efficiency and tire wear are severely affected by its under-inflation. The fact is that, tires not only leak air if punctured, they also leak air naturally (which might amount to roughly 10% of its initial pressure). Obviously, tire pressure plays an important role in its safe and reliable operation. Therefore, it is desirable to have a tire pressure monitoring system (TPMS) which maintain proper tire pressure to ensure driving safety. Smart tires equipped with embedded sensors can meet this purpose through monitoring the tire strain, and/or its pressure and temperature in order to activate certain precautionary means [1,2]. Ever since car industries introduced the very first Tire Pressure Monitoring System (TPMS), manufacturers have been struggling hard to solve two major technical challenges: developing a TPMS that requires as little power as possible to operate and a robust and a rugged, liable power source.

A major problem with regard to smart tires is that, because of the rotation of the wheels, the sensors housed inside the tire cannot have a fixed connection to the measurement system so that troublesome slip rings should be used. Existing techniques often rely on active sensors which send signals over antennas to a decoding system fixed at the body of the vehicle. Therefore, they need a battery. But, batteries have the drawback that they eventually run out, leaving car owners with a non-functioning TPMS and the replacement issues. The use of wireless sensors has solved the problems with the slip rings, but these sensors also need batteries. In current designs, the wireless sensors are buried under the rubber, and hence an onboard power supply is mandatory. In recent years,

energy-harvesting devices are taking a prominent role in smart tire applications to provide passively the energy needed by these sensors. A micro power energy harvester would be an ideal source [1] of energy to power up delicate wireless sensors. Recent advancement in power circuit designs and the continuous reduction in their size and power consumption has resulted in a new era of wireless sensors in industrial and automotive applications, i.e., whenever the power required is very small. This order of scaling has enabled micro-power energy harvesting systems quite appealing in wireless applications. The main objective is to relinquish the bulky, high cost, chemical batteries and also the required wirings from the TPMS housed inside the tire through developing battery-less TPMS's [3–9]. A novel idea is the incorporation of energy harvesting techniques from rotary assemblies in order to intermittently power the TPMS. And, there are currently several strategies available for this purpose: i) electrostatic, ii) electromagnetic, and iii) piezoelectric[3]. Among them, piezoelectric transducers (PZTs) appear to be more promising for use in smart tires where vibration is a common effect[4]. Also, the energy density of PZTs is almost three times higher than electrostatic and electromagnetic transducers making them a good candidate for use in smart tires[5].

Energy harvesting is the conversion of dispersed energy present in the environment into usable electrical energy. To that end, mechanical vibrations are very appealing (particularly, for low-power electronics) thanks to their versatility and abundance in the ambient. The most common way of harvesting mechanical vibration is based on the use of linear resonant structures composed of a spring-mass system [10–12]. But these linear resonating systems produce a very narrow bandwidth in the operating frequency spectrum, and this severely limits their range of applicability [3], [13]. To overcome this limitation, two main approaches could be used: i) tuning the resonance frequency of the structure with respect to the ambient frequency, ii) widening the energy harvester bandwidth by special means[14] In the past few years, many intriguing methods have been employed to tune the resonant frequency of the harvester to fully match the frequency of the ambient vibration. To reach this goal, these methods rely on varying the length of the PZT cantilever[15] and/or the spring stiffness [16] [17]. There are also methods which can widen the frequency spectrum of energy generators through increasing the mechanical damping of the system with the price being that the maximum power attainable is reduced [18], [19]. Most energy harvesters reported in the literature

rely on the vibrations induced from the base excitations. In a recent study[20], it has been shown that a gravity component can be used in rotary motion to cause a beam to vibrate in such a way that the harmonic oscillation generated in the transvers direction becomes quite similar to the base excitation. This mechanism was shown to produce sufficient amount of energy to recharge batteries in a tire pressure-monitoring-system.

1.1. Research Objectives

The use of linear resonating structures in harvesting mechanisms, forces the system to have a very narrow bandwidth in the frequency spectrum. This makes the harvester to become completely inefficient whenever the ambient excitation is not matched to the resonance frequency of the harvester. Our main objective in this research is to come up with a new design (typically of spring/mass structure) which can remedy this drawback. The new design should enable an increase in the bandwidth of energy harvesting capability of spring/mass resonators. In tire pressure monitoring systems, the host structure does undergo continuous rotation. This thesis aims to demonstrate that such a rotational motion could be used effectively for harvesting energy and actively powering up wireless sensors embedded in the wheel-tire assembly. More explicitly, the main objectives of this research are:

- Deriving a valid coupled electromechanical model of our proposed mechanism which could reasonably predict the amount of power acquisition when subjected to a constant and continuous rotary motion. The model should also be able to predict the influence of linear resonating parameters such as spring stiffness and load mass values on the total performance of the energy harvesting substructure.
- Validating the analytical model by fabricating a test bed which could simulate the rotary motion. Fabricating a prototype of our proposed mechanism and conducting a full experimental study is also one of our objectives.

1.2. Thesis Structure

This thesis is organized into eight chapters. A quick review of the chapters is as follows:

- Chapter 2 presents practical methods for energy harvesting which are basically used to harvest energy out of ambient vibration. The chapter will introduce available techniques currently being used for boosting up the bandwidth of linear resonating harvesting mechanisms.
- Chapter 3 provides an introduction to energy harvesting using piezoelectric effects. A phenomenology of piezoelectricity effect and how it operates will be discussed. Also, the capability of piezoelectric energy harvesting systems will be discussed in different applications.
- Chapter 4 draws a step by step procedure for deriving a valid coupled electromechanical model for practical energy harvesting mechanisms and shall also introduce fundamentally effective parameters present for such harvesting mechanisms.
- Chapter 5 elaborates on a detailed analytical study for estimating the power acquisition from a tangent piezoelectric cantilever beam mounted on the inner side of a wheel/hub which acts as a rotating host. In consideration of the dynamic modeling of the rotating cantilever beam, a Lagrangian approach shall take place and a solution for estimating vibration response and output voltage of the harvester will be provided. The study shall follow up by estimating the maximum power using the optimal resistive load. A finite element analysis has also been done in order to define the safety factor of such harvester to predict whether it undergoes failure or not.
- Chapter 6 provides a feasibility analysis on our novel coupled linear resonating energy harvesting prototype. To that end, a base excitation problem has been defined for the prototype, and a comprehensive study is done both numerically and experimentally, and the results will be compared and analyzed.
- Chapter 7 shall introduce the proposed coupled linear resonating structure which was analyzed in chapter 6, in a rotary motion application. A comprehensive analytical study is carried out for such a mechanism undergoing rotary motion.

Furthermore, governing equations are derived for predicting the dynamic motion and the amount of the acquired power out of the harvester. The chapter continues by introducing a test bed, designed for this project and. The analytical results are shown to compare reasonably well with the experimental results extracted from the prototype.

- Chapter 8 summarizes the work reported in this thesis and makes some suggestions for future works.

2. Energy Harvesting

The use of wireless systems is becoming ever-present as they offer several advantages over existing wire-based technologies. This advantage rises from their ability to retrofit into systems without having to consider about cabling issues. Moreover, due to factors like flexibility, ease of implementation and installation especially in inaccessible locations, wireless devices could be beneficial for condition-based monitoring (CBM) applications [21]. In such systems, wires or any other associated connector, may become the main cause of failure and introduce a considerable cost issue.

At present, many wireless sensors are battery-based devices which operate in an extremely low power (order of micro-watt) state [22]. These low power wireless sensor devices have opened up a new era for investigating alternative types of power source to traditional batteries, enabling us to mitigate the environmental impact caused by issues surrounding the disposal of the batteries. The ultimate goal in this aspect is to power such small electronic so that the need for an external power source or periodic battery replacement can be removed or at least minimized [23–26].

Ambient, free energy sources from which it is possible to harvest energy can be classified as: i) kinetic, and ii) non-kinetic energy resources. Kinetic energy sources rely on ambient or more typically vibration-based motions present in the surrounding environment or mechanical host structure [3][27]. On the other hand, non-kinetic energy sources can be obtained by generating electrical energy from solar energy caused by the radiation of the sun [28][29], or thermal energy arising from thermally conducting materials [30–33].

2.1. Working Mechanisms of Kinetic Energy Harvesters

In this section, the working mechanisms of kinetic energy harvesters will be discussed. A transducer is a device that converts energy from one form to another. In energy harvesting terms, the transducer has the role of extracting energy from an ambient source and converting it into usable electrical power. To achieve this goal, a mechanical system is needed which couples environmental displacement to an electrical signal. The coupling between the mechanical system and the transducer depends entirely on the characteristics the environmental motion surrounding it. Kinetic energy harvesters, which are typically vibration–based energy harvesters, employ various extraction mechanisms such as piezoelectric, electromagnetic and electrostatic [3] to harvest ambient energy from the environment. Such transducers are well suited to be modeled by a conventional second-order spring-mass system together with a linear damper as shown in Figure 2-1.

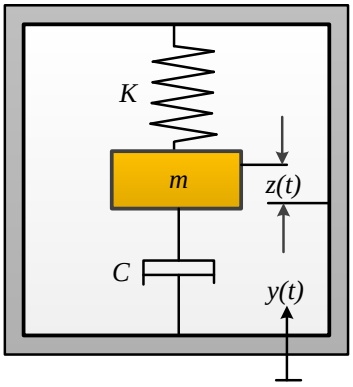

Figure 2- 1. Model of a linear, inertial generator

This simple model is easily able to encompass important aspects of inertial (i.e., vibration-based) generators and could provide with a good insight on how such generator behave. In Figure 2-1, m corresponds to the seismic mass, and k stands for the stiffness. All energy losses within the system (comprising parasitic losses and electrical energy extracted by the transducer mechanism) are represented by the damping coefficient, c_T. Having assumed that the system is undergoing a sinusoidal vibration of the form: $y(t) = Ysin(\omega t)$, the suspended inertial mass within the frame will subsequently produce a relative displacement, $z(t)$, between itself and the frame. Thus,

it induces a resonant frequency to the system which can be tuned to match the characteristic frequency of the ambient vibrations. The differential equation of such a system is given by,

$$m\ddot{z}(t) + c_T\dot{z}(t) + kz(t) = -m\ddot{y}(t). \tag{2-1}$$

Where m, *is the mass,* C_T *is the damping and* k *is the equivalent stiffness.* Energy is extracted from the relative movement between the mass and the inertial frame. Equation 2-1, can also be written in terms of damping constant and natural frequency. Having introduced a damping factor ζ, , which is a dimensionless number defined as the ratio of system damping to critical damping, and $\omega_n = \sqrt{k/m}$, known as the natural frequency of the structure, the ratio of output $z(t)$ and input $y(t)$ can be obtained by applying Laplace transform with zero initial condition as,

$$\left|\frac{Z(s)}{Y(s)}\right| = \frac{s^2}{s^2 + 2\zeta\omega_n s + \omega_n^2}. \tag{2-2}$$

Applying the inverse Laplace would give us the time domain of the response,

$$z(t) = \frac{\left(\frac{\omega}{\omega_n}\right)^2}{\sqrt{\left(1 - \left(\frac{\omega}{\omega_n}\right)^2\right)^2 + \left(2\zeta\frac{\omega}{\omega_n}\right)^2}} Y sin(\omega t - \phi) \tag{2-3}$$

where ϕ is the phase angle given by,

$$\phi = \tan^{-1}\left(\frac{c_T\omega}{k - \omega^2 m}\right) \tag{2-4}$$

The power extracted by the transducer mechanism is given by,

$$P(t) = \frac{m\zeta Y^2 \left(\frac{\omega}{\omega_n}\right)^3 \omega^3}{\left(1 - \left(\frac{\omega}{\omega_n}\right)^2\right)^2 + \left(2\zeta \frac{\omega}{\omega_n}\right)^2} \quad (2\text{-}5)$$

The maximum power can be extracted when the excitation frequency matches the natural frequency of the system, $\omega_n = \sqrt{k/m}$; that is,

$$P_{max} = \frac{mY^2\omega_n^3}{4\zeta} \quad (2\text{-}6)$$

The aforementioned equations clearly indicate that an increase in damping effects can broaden the bandwidth response and provide us with a generator which is less sensitive to the frequency.

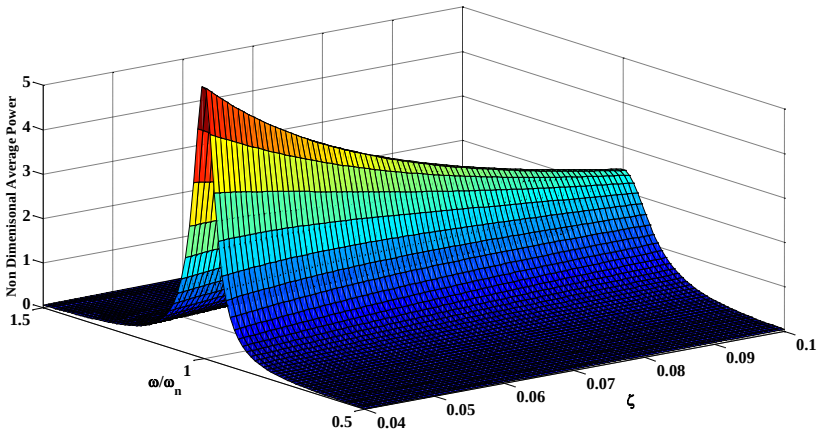

Figure 2- 2. Dependency of power acquisition to damping and frequency ratio

Furthermore, the mass of the mechanical structure should be maximized within the given constraints in order to maximize the electrical power output. In the following, we will introduce current vibration-based extraction mechanisms which are in practice nowadays.

2.1.1. Electromagnetic Energy Harvesting

Electro-magnetism has been used to generate electricity after Faraday's fundamental breakthrough in electromagnetic induction in 1831. Electromagnetic induction is the generation of electric current in a conductor (typically having the form of a coil) moving within a magnetic field. The electricity so generated is due to either relative movement between the magnet and the coil, or because of variations in the magnetic field itself. Electromagnetic generators can be used to harvest micro- to milli-Watt levels of power using both rotational and linear devices. Although these systems present a formidable technique for power harvesting, yet attempts to miniaturize the technique should take place in order to enable these methods to be deployed in real applications. However, it should be noted that using micro-engineering technology to fabricate a generator of such type, would undoubtedly reduce efficiency levels considerably [4][34].

One of the most effective methods for energy harvesting is to generate electromagnetic induction by means of permanent magnets, a coil and a resonating cantilever or spring. In particular, either the coil or the magnets can be chosen to be mounted on the beam (spring) while the other should remain fixed [11], [35–38]. However, in general, for the tip-mass to affect the beam frequency response, it is more preferable to mount the magnets directly on the beam.

El-hami et al. [35] simulated and fabricated a cantilever-based electromagnetic generator. In his design the cantilever beam is clamped at one end and has a pair of neodymium iron boron (NdFeB) magnets attached to a c-shaped core located at the free end of the beam (Figure 2-3). In this embodiment, the magnetic field will be moving relative to a stationary copper and generate electromagnetic induction.

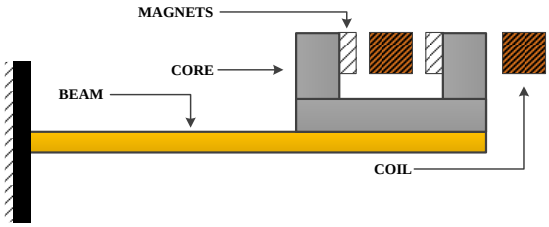

Figure 2- 3. Resonant frequency tuning of an electromagnetic energy harvester using magnets [35]

From the fundamental principles, and from the analysis of generators tested to date [39], it is clear that electromagnetic devices do not favourably scale down in size. One can say that, with the advent of MEMS technology, future applications for micro scale vibration energy harvesters will be met by methods based on piezoelectric and electrostatic extraction mechanisms.

2.1.2. Electrostatic Energy harvesting

An electrostatic (capacitive) harvester acquires power from ambient vibrations by incorporating a variable capacitor within. The pre-charged capacitor plates are relatively moved when subjected to ambient mechanical vibrations. This relative motion works against the electrostatic force which tends to hold the capacitor plates at its most stabilized (minimum separation distance in between plates) position which in fact provides the harvested energy. In other words, The ongoing process induces a variation in the charge stored on the capacitor plates in order to meet the very basic requirement of any capacitor which is: $Q = CV$, where C is the capacitance in farads and V is the voltage generated. As for an electrostatic transducer, the energy conversion could be done by either holding the charge or voltage between the plates constant.

Electrostatic generators can be classified into three main categories [40], [41]: i) in-plane overlap varying, ii) In-plane gap closing, iii) out-of-plane gap closing (Figure 2-4). These three approaches can be easily operated either in charge constrained or voltage constrained cycles, yet it is more desirable to use the voltage constrained approach since the transducer will benefit from harvesting more energy [34].

Electrostatic generators are a highly ranked candidate when one's concern is on MEMS and micro-system applications. This is due to the characteristic behaviour and

concept that energy density of such generators can be easily boosted up by decreasing the capacitor gapping. Nevertheless, these generators may not be regarded as a good candidate for energy harvesting. This is because they require an initial polarizing voltage or charge forcing them to rely on a secondary generator, say, a battery [4]

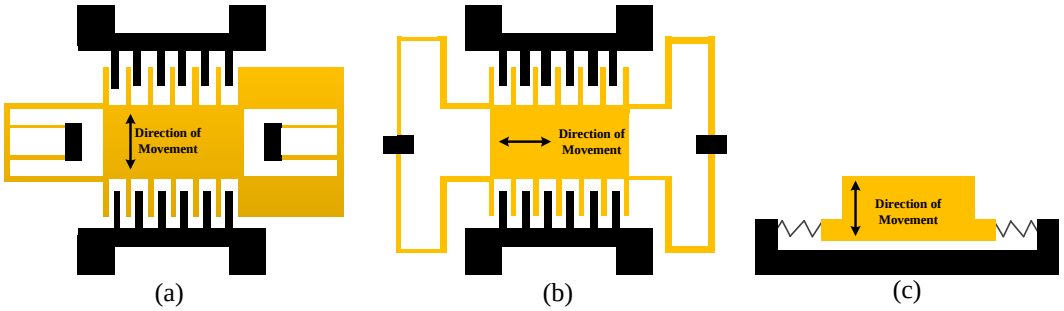

Figure 2- 4. (a) in-plane overlap varying (b) in-plane gap closing (c) out-of-Plane gap closing [40]

2.1.3. Piezoelectric Energy Harvesting

A piezoelectric transducer is a device which transforms one type of energy to another by taking advantage of the piezoelectric properties of certain crystals or other materials. When a piezoelectric material is subjected to stress or force, it generates an electrical potential or voltage proportional to the magnitude of the force. The piezoelectric effect also works in reverse. That is, a voltage applied to a piezoelectric material will cause that material undergo deformation. Typically a piezoelectric energy harvester is a vibration-based energy harvester, which is a cantilever beam (Figure 2-5) with one or two piezoceramic layers (a unimorph or a bimorph) [42]. The harvester beam is located on a vibrating host structure and the dynamic strain induced in the piezoceramic layers generates an alternating voltage output across the electrodes covering the piezoceramic layers.

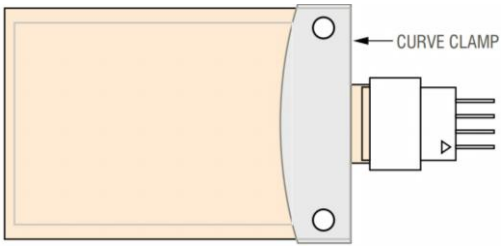

Figure 2- 5. Schematic of a piezoelectric beam

As a comparison, the energy density produced from piezoelectric transducers is about three times higher than electrostatic and electromagnetic transducers [4]. The piezoelectric generators offer the simplest approach of energy harvesting since there is no need for having complex geometries and numerous additional components. This simple mechanism is well capable of producing relatively high output voltages yet low electric currents. It has to be mentioned that the piezoelectric materials are required to be strained directly and therefore their mechanical properties will put limit on their overall performance and lifespan [34]. The work undertaken in this thesis concerns a rotational energy harvesting system with the core of the extraction mechanism relying on the characteristics of a piezoelectric cantilever beam. For this reason, in subsequent chapters, a thorough discussion will be presented on piezoelectric energy harvesters.

2.2. Strategies for Enhancing the Performance of Energy Harvesters

As mentioned in the previous section, three major principles are typically being used as a solution for vibration to electricity conversion. Nevertheless, no matter which principle is being exploited for that purpose, the majority of vibration-based energy harvesting devices designed nowadays are linear resonating structures. Such structures generate a single narrow resonance frequency causing the system to deliver its maximum performance only when the resonating frequency matches the external excitation frequency. Moreover, there would be a sudden and dramatic decrease in the performance of the harvester should there be any slight shift in the external excitation. Due to this limitation, the energy harvester must be designed to resonate at the vibration source's peak acceleration amplitude. Unfortunately, in most cases of practical importance, the vibration is completely random or spans a broad range of frequencies.

And, this poses one of the most important limitations in implementing energy harvesters for real-world applications. That is, each energy harvester must be tailored to a specific application's vibration spectrum. Therefore, addressing the challenging problem of how to extend the bandwidth of these mechanisms becomes a necessity before any practical deployment of such harvester can be made in real applications.

The following presents a review of current techniques in for remedying the shortcoming of linear resonating energy harvesting structures. These methods are namely known as multimodal energy harvesting, frequency up-conversion (or frequency pumping), and other related methods [43].

2.2.1. Resonance Frequency Tuning Technique

As clearly stated in the prior sections, a linear resonating energy harvesting mechanism with its fixed resonance frequency is unable to obtain sufficient amount of power from ambient, so that it may not be suitable for our design purposes. It is one of the main objectives of the present work to come up with a new harvesting mechanism which could incorporate a resonance tuning mechanism in order to boost its functionality. Actually, the idea is not new and as was explained by Roundy and Zhang [44], can be done either 'actively' or 'passively'. A continuous source of power is needed for resonance tuning in an active mode. In the passive mode, however, an intermittent initial power is needed initially for the tuning, but power is needed as the frequency matching is completed.

The resonance tuning methods can be achieved by either mechanical methods or magnetic approaches. In the following sections we shall provide a brief description of these methods.

2.2.2. Mechanical Techniques

From a vibrational point of view, one could say that the resonance frequency of any system could be altered by changing either the total stiffness and/or the mass of the system. (It is more common and practical should we choose to change the stiffness rather than the mass of the system.) The technique was put on test by Leland and

Wright [45] who showed that the resonance frequency of their proposed mechanism is tunable by applying an axial compressive load. This load would in fact alter the stiffness of the harvester. A schematic view of the proposed mechanism is shown in Figure 2-6. Their study revealed that by applying such a load, the resonance frequency of a harvesting mechanism is lowered down by up to 24% from its initial resonating frequency. It has to be mentioned that their design was intended to operate in a passive mode as it could be tuned manually.

Further analytical studies were set place by Hu et al. [46] enabling him to derive a set of governing equations for a cantilever piezoelectric beam undergoing an axial preload. They predicted that such system is capable of adjusting its resonance frequency to either higher or lower values by applying a tensile or compressive load.

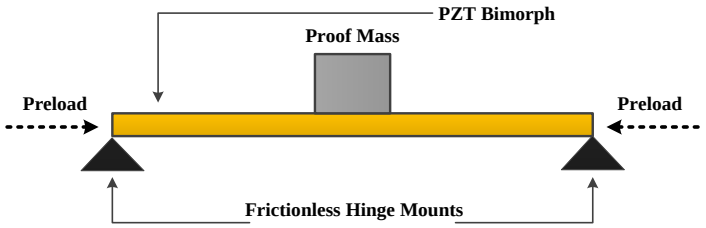

Figure 2- 6. Schematic of a simply supported bimorph energy harvester [46]

Wu et al. [46], proposed another method by adjusting the center-of-gravity of the tip mass in order to tune the resonance of a cantilever beam. This mechanism was designed by realizing a portable tip mass on the beam. The center of gravity of the proof mass could then be easily adjusted and moved to the desired position by driving a movable screw which was attached to the mass.

2.2.3. Magnetic Techniques

Magnetic force is known to be another effective method to alter the stiffness of the harvesting mechanism. A tuneable harvesting mechanism consisting of a cantilever beam and two pair of permanent magnets was proposed by Challa et al. [47]. Two magnets were mounted at the free end of the cantilever beam while the other two were fixed to the top and bottom of the enclosure of the device. A schematic view of this design has been shown in Figure 2-7. The magnetic force was then altered by changing

the distance between the magnets using a simple spring-screw. It was shown that an alteration of the magnetic force would affect the stiffness of the beam, and in turn vary its resonance frequency.

Another similar study was done by Reissman et al. [48] which introduced a novel technique of using variable attractive magnetic force, as indicated in Figure 2-7. This study pointed out the fact that the resonance of the piezoelectric energy harvester could be tuned by adjusting a magnetic slider mechanism.

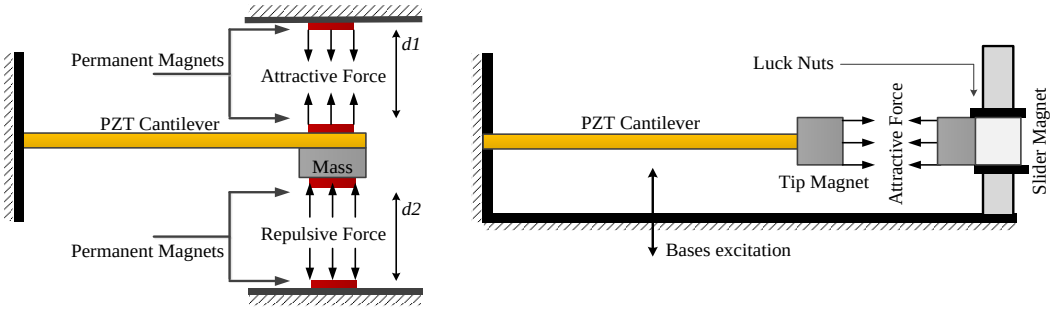

Figure 2- 7. Tuneable harvesters (left) Challa et al. (right) Reissman et al. [48]

2.2.4. Multi-modal Energy Harvesting

The concept of multi-modal energy harvesting has proven to be a prospective method to pursue when energy harvesting in its most effective way is the main concern. Due to the abundance availability of various energy resources in one given scenario, such as solar, wind, and vibrations, this method investigates the feasibility of combining two or more energy harvesting schemes in one system such that one assists and takes advantage of the other [43]. This combination enables obtaining significant output power over a wide range of operating frequencies when compared to the energy harvesting systems utilizing only one energy harvesting method.

2.2.5. Hybrid Energy Harvesting Scheme

An ideal example of a multi-modal energy harvesting device could be met by combining the principles induced inside of an electromagnetic and a piezoelectric energy harvesting mechanism. In such devices alike, the piezoelectric transducer and the electromagnetic field are mutually contributing towards power generation [49]. The

design of such a system consists of a cantilever beam with piezoelectric plates mounted at precise locations (Figure 2-8). Furthermore, a permanent magnet, which oscillates within a stationary coil, is also incorporated at the tip of the cantilever beam serving two different purposes: 1) it acts as a proof mass and induces some stress to the cantilever, and 2) it acts as a core oscillating in between the stationary inductive coils and generates electric current throughout Faraday's law.

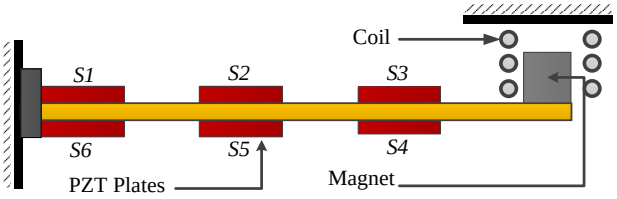

Figure 2- 8. Schematic structure of the multi-modal energy harvester [49]

Utilizing multiple cantilevers or cantilever arrays integrated in one energy harvesting device has shown to be another method to generate continuous wide bandwidth should the geometric parameters of the harvester are delicately selected. As an example of such a method, Yang and Yan [50] suggested the use of coupling bimorph cantilevers having resonance frequencies close to each other. Figure 2-9 shows the schematic of the design. Their studies showed that with a proper design of the load masses and the spring intersecting them, the proposed structure would acquire energy across a wider frequency spectrum than a single cantilever beam harvester.

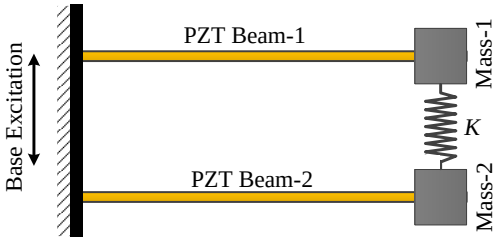

Figure 2- 9. Schematic of two beams with two masses elastically connected [50]

Another method which ensures a wide bandwidth power acquisition is by the incorporation of quasi-uncoupled cantilevers. In this method, each cantilever is regarded as one substructure of the harvesting mechanism and acts and resonates individually. Accordingly, the first mode of each cantilever is one of the vibration modes of the

harvester. Figure 2-10-a, shows such a mechanism. This system comprises multiple piezoelectric cantilevers having different lengths and load masses all of which attached to a common base. It has been shown that, by properly selecting the length and tip mass values of each individual piezoelectric beam one could obtain voltage and power over a wider frequency range (Figure 2-11-b) [19].

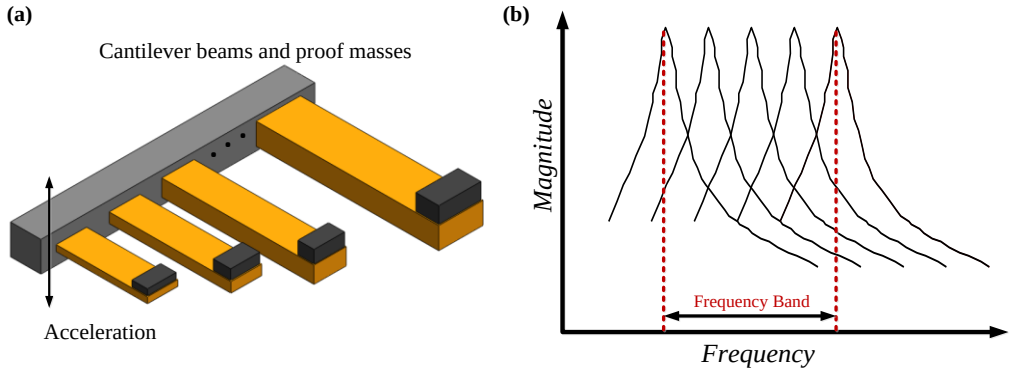

Figure 2- 10. (a) Band-Pass filter, and (b) its transfer function

Another method of using cantilever arrays for broadening the frequency bandwidth was proposed by Xue et al [46]. They showed that by manipulating multiple piezoelectric beams with different thicknesses (Figure 2-11-a), one could achieve different operating frequencies and hence obtain a wider bandwidth (Figure 2-11-b).

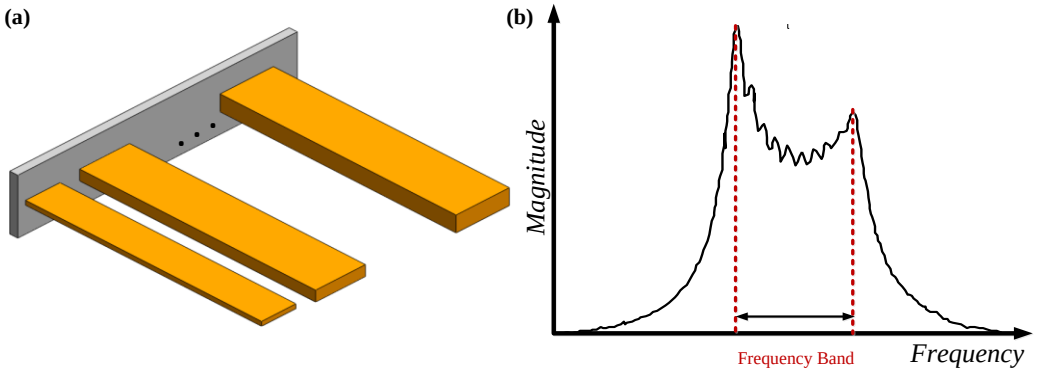

Figure 2- 11. (a) Schematic of the harvester with multiple PZT beams. (b) Power output vs. frequency for two cases: a single PZT beam and 10 PZT beam connected in series with various thickness

Compared to resonance tuning, multimodal energy harvesting technique is much easier to implement. However, they require somewhat sophisticated circuits than the

single conversion mechanisms or single cantilever configurations. To be more specific, in a cantilever array configuration, each cantilever requires an individual rectifier for the sake of avoiding output cancellation due to possible phase difference between the cantilevers [51].

2.2.6. Frequency Up-Conversion (Frequency Pumping)

One method of increasing the power harvested by a typical piezoelectric transducer is to subject the transducer to more deflections in the same time period by any means possible. Typical vibration frequency seen in ambient and in various machines is in the range of 5-100 Hz [43], which is in fact much lower than the operating frequency of the raw micro-generators. The aforementioned method follows the concept of amplifying the source vibration frequency before being applied to the piezoelectric transducer which shall consequently improve the efficiency of the system. A simple way to boost the frequency by such method is by the use of mechanical devices such as gears or springs. The utilization of such gears can be found in the design of a novel windmill (Figure 2-12) designed by Priya [52].

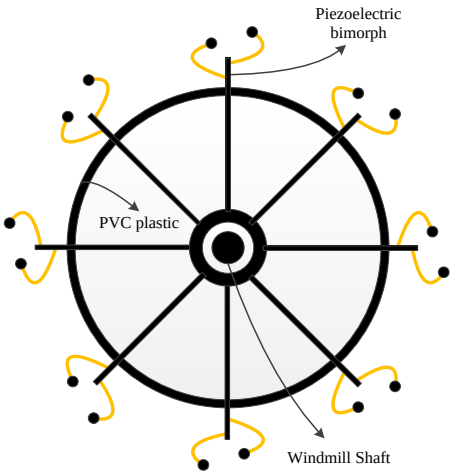

Figure 2- 12. Schematic diagram of the piezoelectric windmill [52]

In the next chapter we will discuss the current methods available for energy harvesting using piezoelectric effect.

3. Piezoelectric Energy Harvesting

In the previous chapter piezoelectricity was mentioned as one liable and feasible technique for energy harvesting from ambient vibrations. This chapter shall provide a brief description of the range of piezoelectric generators described in the literature to date. To that end, piezoelectric generators have been classified by methods of operation and applications. In order to better appreciate different types of generators, the chapter begins with briefly describing the piezoelectric phenomena and the physics behind its operating mechanism at a molecular scale.

3.1. The Piezoelectric Effect

The piezoelectric effect was first discovered by Curie in 1880. They discovered that an electrically polarized domain is induced in certain crystals should they be subjected to a mechanical strain. They also found out that the degree of such polarization is proportional to the magnitude of the applied strain. Interestingly, such crystals would deform if subjected to an electric field. Crystals of such nature are realized to have no center of symmetry. As an explanation to this fact, one should investigate he individual molecules that form the crystal. Each of these molecules has a distinct polarization, meaning one end of it to be more negatively charged and the other end to be positively charged. This sort of charge seen in each molecule is called dipole. This polarization is mainly due to the style of the atoms shaping the molecules. To that end, there exists an imaginary line called the *polar axis* which runs through the center of both charges of the molecule. In a symmetrical crystal, typically known as monocrystal, all the dipoles lie in one direction. These crystals are said to be symmetric because if the crystal is cut at any point, the resultant polar axes of the two pieces would eventually lie in the same direction as the original piece. On the other hand, in a polycrystalline type of material, different regions having different polar axis co-exist within the material. As a result, there exists no point on the material at which the crystal could be cut so that the

two remaining pieces have the same resultant polar axis. Figure 3-1 illustrates this concept [53].

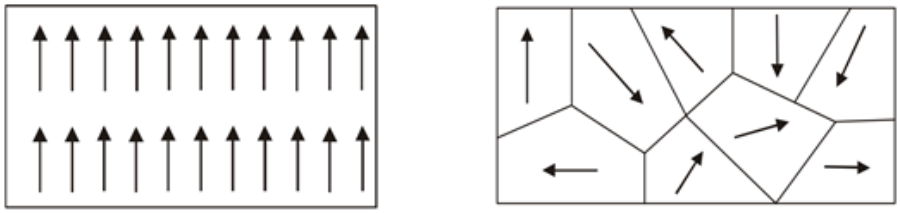

(a) (b)

Figure 3- 1. (a) Monocrystal with single polar axis, (b) Polycrystal with random polar axis [53]

For producing the piezoelectric effect, the polycrystal is heated under the influence of a strong electric field. The heat allows the molecules to move with more ease causing the electric field to orient all dipoles in in *nearly* the same direction. Figure 3-2 shows a schematic view of such process.

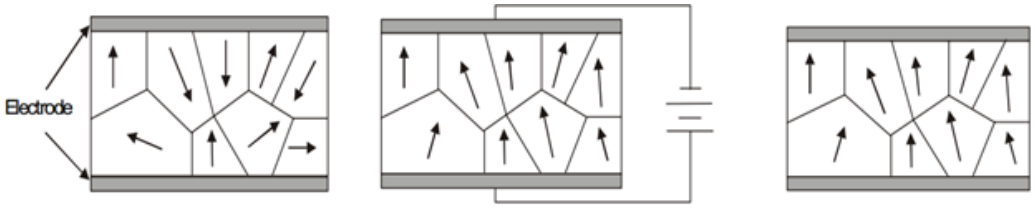

(a) (b) (c)

Figure 3- 2. a) random dipole,b) polarization,c) surviving polarity [53]

The piezoelectric effect can now be observed in the crystal. Figure 3-3 [54] illustrates the piezoelectric effect. This figure shows a cylindrical piezoelectric material initially without a stress or charge (see Fig. 3-3a). A voltage of the same polarity as the poling voltage will appear between the electrodes should the material undergo a compressive load (see Fig. 3-3b). If stretched, a voltage of opposite polarity will appear in the crystal, as shown in Fig. 3-3c. Conversely, if a voltage is applied, the material will undergo a deformation. A voltage with the opposite polarity as the poling voltage will cause the material to expand, as shown in Fig. 3-3d. But, a voltage with the same polarity will cause the material to compress. If an AC signal is applied then the material will vibrate at the same frequency as the driving voltage (Fig. 3-3f).

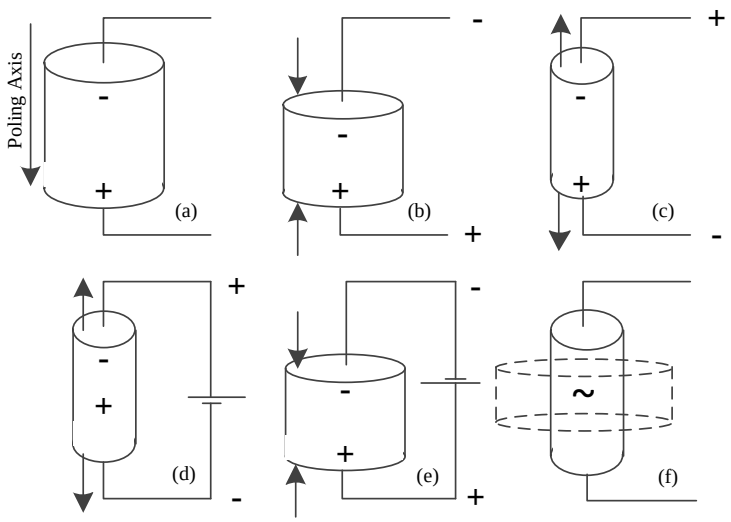

Figure 3- 3. Piezoelectric effect in a body of piezoelectric ceramic: a) no load, b) compressed, c) stretched, d) elongated, e) shrinked, f) periodic.[53]

Piezoelectric materials are available in a variety of forms including single crystal (e.g. quartz), piezoceramic (e.g. Lead Zicronate Titanate or PZT), screen printable thick-films based upon piezoceramic powders, and polymeric materials such as polyvinyllidenefluoride (PVDF) [55–57].

The properties of a piezoelectric material differ depending on the direction of the applied forces and the orientation of the polarized electrodes. To that end, piezoelectric crystals are known to be typical of anisotropic materials. A system of symbols and notations should therefore be used to define their anisotropic properties [58]. This is related to the orientation of the ceramic and the direction of measurements and applied stresses. The direction of positive polarization usually is made to coincide with the Z-axis of a Cartesian co-ordinate system of X, Y and Z axes. Directions X, Y, or Z are represented by the subscript 1, 2, or 3, respectively, and shear about one of these axes is represented by the subscript 4,5, or 6, respectively [58]. The basis for this is shown in Figure 3-4.

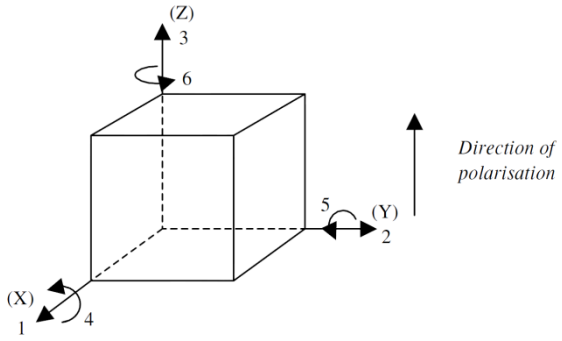

Figure 3- 4. The appropriate coordinate system used to represent a PZT cantilever[58]

Piezoelectric generators that rely on a compressive strain applied perpendicularly to the electrodes exploit the d_{33} coefficient of the material while those that apply a transverse strain parallel to the electrodes utilize the d_{31} coefficient.

It is known that stress, temperature and age could affect the piezoelectric properties. The change in the properties of piezoceramic with time is known as the ageing rate and is dependent on the construction methods and the material type. The changes in the material tend to be logarithmic with time, thus the material properties stabilize with age, and as a matter of fact, manufacturers of such materials usually specify the constants of the device after a specified period of time[34].The aging process is accelerated by the amount of stress applied to the ceramic and this should be considered in cyclically-loaded, energy-harvesting applications. Soft piezoceramic compositions, such as PZT-5H, are more susceptible to stress-induced changes than the harder compositions such as PZT-5A. Temperature is also a limiting factor with piezoceramics due to the Curie point. Above this limit piezoelectric materials will lose their piezoelectric properties by becoming de-polarized [53].

3.2. Vibration-Driven Piezoelectric Energy Harvesting Mechanisms

From the rumble of a passing truck to the gentle hum of the electrical grid, vibrational energy surrounds us in our everyday life. While often considered an annoyance or simply background noise by the general public, design engineers

recognize that this energy is just waiting to be harvested for use in micro power electronics and sensors. In this section, a review of vibration-based energy harvesters will be provided, with a focus on publications which elaborate on the requirements and design of the harvester's power management electronics. This is because the work undertaken in this thesis concerns a rotational energy harvesting system that transfers maximum power from the harvester to an electrical load. A brief mentioning of the latest developments within the energy harvesting community (with regard to the resonant frequency tuning of vibration-driven devices) will also be presented.

3.2.1. Impact-Coupled Devices

Earliest versions of a piezoelectric kinetic energy harvesting system extracted energy from impacts. The feasibility of this approach was first found by dropping a 5.5 g steel ball-bearing from a height of 20 mm onto a piezoelectric transducer to a bronze disk. The study estimated that the optimum efficiency of the impact would be less than 10% with most of the energy being returned to the ball-bearing which bounces off the transducer after the initial impact. Using numerical simulations, it was shown that if the collision were inelastic, the efficiency would boost up to 50% [59]. Recent works done on energy harvesting using impact methods on PZT plates [60] have shown that the electrical energy generated by this method has a linear relationship with the incident energy. Moreover, it has been found that by integrating a silicon-based material onto the PZT plate would result in an improvement in both the magnitude and duration of the electrical output [60].

3.2.2. Human Powered Piezoelectric Generation

Human motion is characterized by large-amplitude movements at low frequencies, and it is therefore difficult to design a miniature resonant generator to work on humans. Methods such as direct straining of piezoelectric elements or impact on such elements have been applied to human applications. Studies have shown that an average walking human of weight 68 kg, produces 67 W of energy at the heel of the shoe [61]. Theoretical studies and calculations indicate that there exists a sufficient amount of power that could be generated form body heat, or blood pressure [61]. Based

on this understanding, it is clear that extracting energy from a walking person presents a potential energy harvesting opportunity.

One of the earliest examples of a shoe-mounted generator incorporated a hydraulic system mounted in the heel and sole of a shoe coupled to cylindrical PZT stacks [62]. The hydraulic system amplifies the force on the piezoelectric stack. A prototype was built and initial calculations showed that a 6.2 W power could be generated while walking. Unfortunately, the prototype was too bulky and could drastically hinder the normal walking of the user.

A similar device consisting of an 8 layer stack of PVDF laminated on either side of a plastic sheet was fabricated and mounted inside a running shoe in the 1990s [63]. It was shown that at a frequency of 0.9 HZ, the fabricated prototype produced an average power of 1.3 mW into a 250 $k\Omega$ load (Figure 3-5).

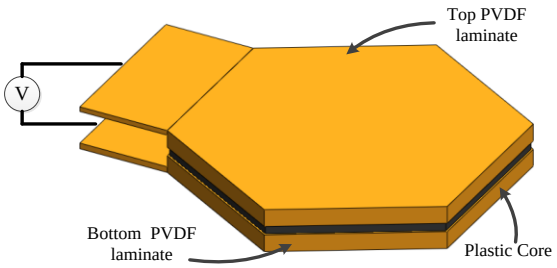

Figure 3- 5. PVDF shoe insole [63]

Later on, another study was conducted for extracting energy from heel strike of a shoe. The study consisted of a compressible dimorph, located in the heel of the shoe (Figure 3-6). As the heel of the shoe hits the ground, the transducers are forced to deform and, as the heel is lifted the transducers spring back in their original shape. Each event generated a voltage and a power up to 8.4 mW could be fed into a 500 $k\Omega$ load [64].

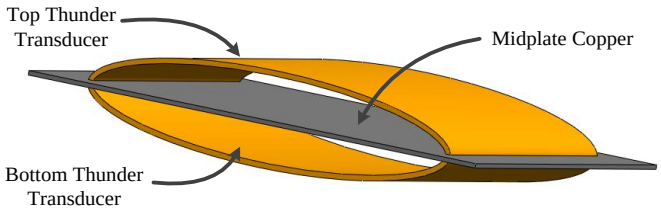

Figure 3- 6. Schematic of the piezoelectric dimorph [65]

Energy harvesting has also been considered in orthopaedic implants. A piezoelectric energy harvester was inserted into the implants with the intention of providing power for the existing sensors in the implant [65]. More importantly, Ramsay and Clark studied the feasibility of using piezoelectric material as a power supply for MEMS application. A square PZT-5A thin plate was driven by a fluctuating pressure source designed to simulate blood pressure. They concluded that there exists an effective surface area in which a piezoelectric generator would be able to power up a device which works in the order of μW [66].

3.2.3. Cantilever-Based Piezoelectric Generators

A cantilever structure with piezoelectric material attached to the top and bottom surfaces is an attractive geometry for harvesting energy from vibrations. The structure is designed to operate in a bending mode thereby straining the piezoelectric films and generating voltage from this act. A cantilever provides low resonant frequencies compared to impact models which (depending on the specific needs and the vibrational conditions) could be further reduced by adding up tip mass on the free end of the beam. A tapered cantilever beam was developed by Jones et al, (Figure 3-7) [67]. The structure was excited at its fundamental bending mode at a frequency of 80.1 Hz and produced 3 μW of power into an optimum resistance of 250 $k\Omega$.

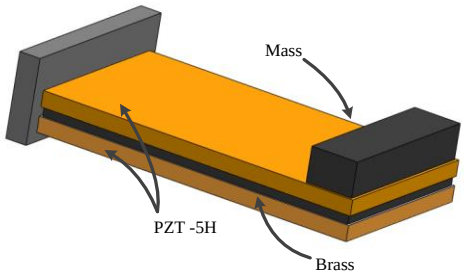

Figure 3- 7. Schematic of a PZT cantilever generator [67]

Khameneifar and Arzanpour [9],[20] looked at the feasibility of utilizing a cantilever piezoelectric beam to extract power from pneumatic tires. They showed that a 8.4 mW electrical power can be generated this way from the prototype [39].

4. Electromechanical Modeling of a PZT Cantilever Beam

In this chapter we shall present a coupled distributed parameter modeling of unimorph and bimorph cantilevers for piezoelectric energy harvesting systems. Closed form solutions are obtained by considering all vibration modes. Steady state electrical and mechanical response expressions are then derived for arbitrary frequency excitations. These multi-modal solutions are then reduced to single-mode solutions for excitations around the modal frequencies.

4.1. Basic Configurations of Piezoelectric Generators

Depending on the application, different types of piezoelectric generators (PEG) can be used for energy harvesting, i.e. stack, bimorph, membrane or spiral rotational springs. Each of these configurations has specific advantages and design limitations and drawbacks. The most widely used PEGs are bimorph cantilever structures which typically consist of two or more piezoelectric layers mounted on a passive metallic or ceramic layer [68]. In order to achieve high-output impedance, the piezoelectric layers are usually connected in series, whereas a parallel connection is used between the piezoelectric layers when a low-output impedance is the target. Figure 4-1, shows a generator based on a cantilever element.

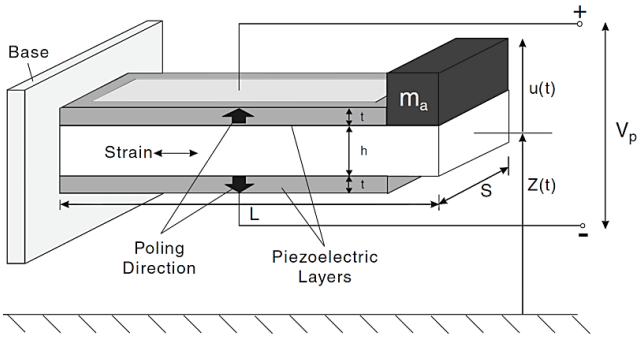

Figure 4- 1. A common piezoelectric-based power generator: a cantilever triple-layer bender operated in the (3-1) mode. [68]

4.1.1. Linear Constitutive Equation for Piezoelectric Material

The linear constitutive equation for piezoelectric materials are given by [69],

$$\begin{pmatrix} S \\ D \end{pmatrix} = \begin{pmatrix} S^E & d \\ d_t & \varepsilon^T \end{pmatrix} \begin{pmatrix} T \\ E \end{pmatrix} \tag{4-1}$$

where *S* is the mechanical strain, *T* is the mechanical stress, *D* is the dielectric charge displacement, and *E* is the electrical field strength. These quantities are tensors of order 2 and 1 respectively. In Eq. (4-1), S^E represents the compliance tensor under the condition of a constant electric field defined as strain generated per unit stress. The tensor d contains the piezoelectric charge constants, which in fact provides us with the relationship between electric charge and mechanical stress. The above constitutive equation can be used for both the direct and the inverse piezoelectric effects. In this equation, ε^T gives the absolute permittivity [49] defined as dielectric displacement per unit electric field for constant stress. Equation 4-1, can be transformed into a form in which the mechanical strain and the dielectric charge displacement are the independent variables.

$$\begin{pmatrix} T \\ E \end{pmatrix} = \begin{pmatrix} C^D & h \\ h_t & \beta^S \end{pmatrix} \begin{pmatrix} S \\ D \end{pmatrix} \tag{4-2}$$

4.1.2. Coupled Distributed Parameter Models and Closed-Form Solutions

The three basic cantilevered piezoelectric configurations are shown in Figure 4-2. The first cantilever shown in Figure 4-2-a is a unimorph configuration with a single peizoceramic layer, whereas the other two cantilevers are bimorph configurations with two piezoceramic layers [70].

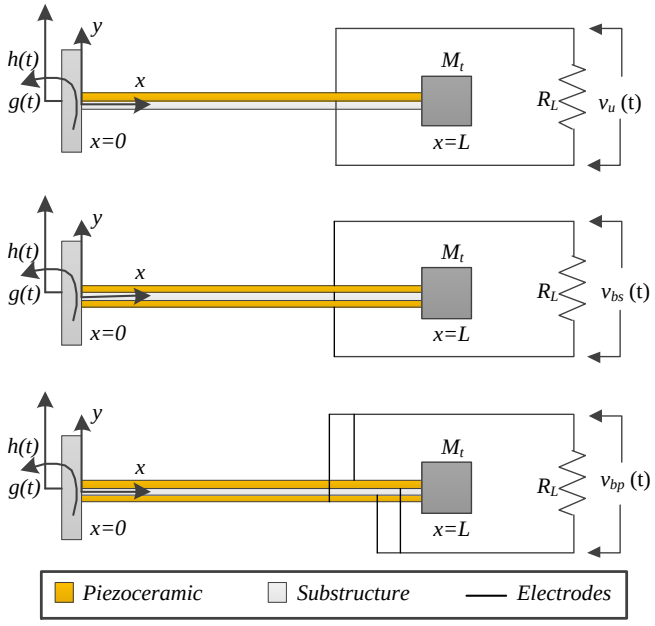

Figure 4- 2. PZT cantilever energy harvester configurations under base excitation: a) unimorph configuration, b) bimorph configuration (series connection), and, c) bimorph configuration (parallel connection) [70]

These configurations are modeled here as uniform composite beams for linearly elastic deformations and geometrically small oscillations based on the Euler-Bernoulli beam assumptions. Therefore, the effects of shear deformation and rotary inertia are neglected, and this is a reasonable assumption since typical piezoceramic benders are designed and manufactured as thin beams. The electrodes covering the opposite faces of the piezoceramic layers are assumed to be very thin so that their contribution to the thickness dimension is negligible. The piezoceramic layers are poled in the thickness direction as depicted in Figure 4-2. Since the bimporph configurations have two piezoceramic layers, one can connect the electrical outputs of the piezoceramic layers either in series (see Figure 4-2-b) or in parallel (see Figure 4-2-c). The continuous

electrode pairs covering the top and the bottom faces of the piezoceramic layers are assumed to be perfectly conductive so that a single electric potential difference can be defined between them. Therefore, the instantaneous electric fields induced in the piezoceramic layers are assumed to be uniform throughout the length of the beam. A resistive electrical load (R_l) is incorporated in the circuit along with the internal capacitances of the piezoceramic layers.

4.2. Mathematical Background

Consider the uniform cantilevered beam shown in (Figure 4-2-a). the beam is under transverse vibration along the y direction, indicated by $w_b(x,t)$. The beam is of rectangular cross section $A(x)$ with widthh_y, thickness h_z, and length l. Also, the flexural bending of the beam is assigned to be $EI(x)$, E is the Young's elastic modulus of the beam and I is the cross sectional area moment of inertia about the z-axis. The beam sustains a bending moment $M(x,t)$, which is related to the beam deflection $w(x,t)$,

$$M(x,t) = EI(x).\left(\frac{\partial^2(x,t)}{\partial x^2}\right) \tag{4-3}$$

Figure, 4-3 illustrates such beam; a model of bending vibration can be derived by examining the forces invoked within an infinitesimal element of the beam. The main assumption in this procedure is that the deformation is small enough such that the shear deformation is much smaller than $w(x,t)$, a summation of forces in the *y* direction yields

$$\left(V(x,t) + \frac{\partial V(x,t)}{\partial x}dx\right) - V(x,t) + f(x,t)dx = \rho A(x)dx\ \frac{\partial^2 x(x,t)}{\partial t^2} \tag{4-4}$$

Where $V(x,t)$ related to the shear force and $f(x,t)dx$ is the total external force applied to the element per unit length. The moments induced on the element dx about z axis through point *Q* could also be found as,

$$\left[\frac{\partial M(x,t)}{\partial x} + V(x,t)\right]dx + \left[\frac{\partial V(x,t)}{\partial x} + \frac{f(x,t)}{2}\right]dx^2 = 0 \xrightarrow{yields} \frac{\partial M(x,t)}{\partial x} = -V(x,t) \tag{4-5}$$

Substituting this expression into equation 4-4 yields

$$\rho A(x)\left(\frac{\partial^2(x,t)}{\partial t^2}\right) + \frac{\partial^2}{\partial x^2}.\left[EI(x)\left(\frac{\partial^2(x,t)}{\partial x^2}\right)\right] = f(x,t) \tag{4-6}$$

If no external force is involved, and Based on the Euler-Bernoulli assumptions (i.e., shear deformations and rotary inertias are negligible), free vibrations of the beam are governed by the following partial differential equation [49].

$$\frac{\partial^2 M(x,t)}{\partial x^2} + m\frac{\partial^2 w(x,t)}{\partial t^2} = 0 \tag{4-7}$$

where m is the mass per unit length, $w(x,t)$ is the absolute transverse displacement of the beam at point x and time t. Figure 4-3 shows the schematic of such a beam. The internal bending moment term $M(x,t)$, which is the first moment of the axial stress integrated over the beam cross section, corresponds to the piezoelectrically-induced voltage.

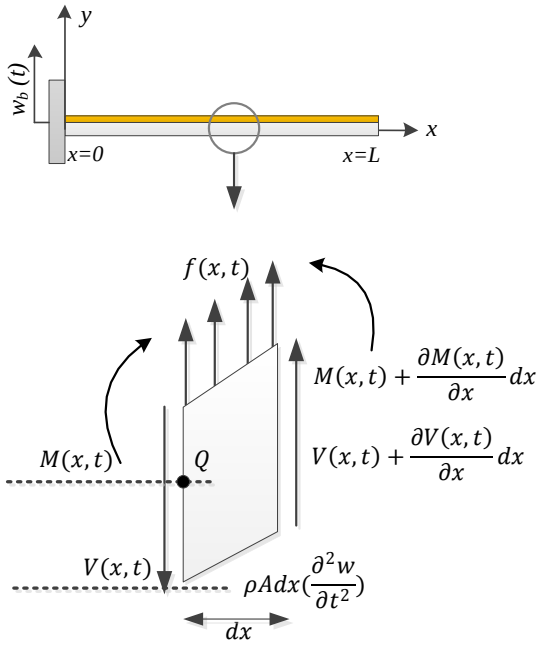

Figure 4- 3. Cantilevered beam excited in transverse direction

In order to introduce piezoelectric coupling to the beam equation, the following axial stress expression [42] must be used in expressing $M(x,t)$ over the thickness of the beam occupied by the piezoceramic layers,

$$T_1 = c_{11}^E S_1 - e_{31} D_3. \tag{4-8}$$

where T_1 is the axial stress component, S_1 is the axial strain component, C_{11}^E is the elastic stiffness of the piezoceramic layer at constant electric field, e_{31} is the piezoelectric constant, D_3 is the electric field component, and 1 and 3 directions coincide with the longitudinal and thickness directions. The axial strain component at a certain level (y) from the neutral axis of the composite beam is proportional to the curvature of the beam at that position (x); that is,

$$S_1(x, y, t) = -y \frac{\partial^2 w_{rel}(x, t)}{\partial x^2}. \tag{4-9}$$

As proposed by Timoshenko et al. in 1974 [71] the absolute displacement response $w(x, t)$ can be given in terms of the base excitation $w_b(x, t)$ and the transverse displacement response $w_{rel}(x, t)$ relative to the base as,

$$w(x, t) = w_b(x, t) + w_{rel}(x, t), \tag{4-10}$$

where the base displacement is equal to,

$$w_b(x, t) = g(t) + xh(t). \tag{4-11}$$

The base excitation consists of translation in transverse direction (denoted by $g(t)$) and superimposed small rotation (denoted by $h(t)$). Equation 4-11 can then be substituted into Equation 4-5 to obtain a forced vibration equation for the transverse displacement response of the beam relative to its base,

$$\begin{aligned} YI.\frac{\partial^4 w_{rel}(x, t)}{\partial x^4} + m\frac{\partial^2 w_{rel}(x, t)}{\partial t^2} + \vartheta v(t)\left[\frac{d\delta(x)}{dx} - \frac{d\delta(x - L)}{dx}\right] \\ = -[m + M_t\delta(x - L)].\frac{\partial^2 w_b(x, t)}{\partial t^2} \end{aligned} \tag{4-12}$$

The above equation is the expanded form of the coupled mechanical equation of motion in the physical coordinates in which the bending moment term has been expanded to give a term related to bending stiffness and an electrical term due to piezoelectric coupling. In this equation, M_t, is the tip mass attached to the free end of the beam, $\delta(x)$ is the Dirac delta function, ϑ is the piezoelectric coupling term (to be discussed shortly), and $v(t)$ is the voltage across the resistive load for the given cantilever configuration. One should be aware that the electrical and mechanical terms, as well as the piezoelectric coupling term ϑ, differ for the three configurations shown in Figure 4-2. It is important to note that the right-hand side forcing function has two components. One component is due to the distributed inertia of the beam, whereas the other component is due to external viscous damping. If the surrounding fluid is air, then the excitation term due to air damping is typically negligible when compared with the inertial excitation term [42]. $w_{rel}(x,t)$ can be represented by an absolutely and uniformly convergent series of the eigenfunctions as,

$$w_{rel}(x,t) = \sum_{r=1}^{\infty} \phi_r(x)\eta_r(t). \tag{4-13}$$

where $\phi_r(x)$ and $\eta_r(t)$ are the mass normalized eigenfucntion (mode shapes) and modal response of the clamped-free beam for the *r*th vibration mode, respectively. rearranging equation 4-13 into equation 4-7 , would yield to,

$$C^2\left(\frac{X''''(x)}{X(x)}\right) = -\frac{\ddot{T}(t)}{T(t)} = \omega^2 \tag{4-14}$$

In which the temporal part, has a solution in the form of

$$T(t) = A\,sin\omega t + B\,cos\omega t \tag{4-15}$$

And the spatial term has a solution on the form of

$$X(x) = a_1 sin\beta x + a_2 cos\beta x + a_3 sinh\beta x + cosh\beta x \tag{4-16}$$

For the modal expansion, the eigenfunctions can be found by applying the boundary conditions of a cantilevered beam which is free at one end fixed at the other. This would yield to,

$$\phi_r(x) = C_r\left[\cos\frac{\lambda_r}{L}\,x - \cosh\frac{\lambda_r}{L}\,x + \zeta_r\left(\sin\frac{\lambda_r}{L}\,x - \sinh\frac{\lambda_r}{L}\,x\right)\right]. \tag{4-17}$$

where λ_r is the dimensionless frequency numbers (eigenvalues) obtained from solving the following characteristic equation [49],

$$\begin{aligned}1 + \cos\lambda\cosh\lambda + \lambda\frac{M_t}{mL}(\cos\lambda\sinh\lambda - \sin\lambda\cosh\lambda) - \frac{\lambda^3 I_t}{mL^3}(\cosh\lambda\sin\lambda + \sinh\lambda\cos\lambda)\\ + \frac{\lambda^4 M_t I_t}{m^2 L^4}(1 - \cos\lambda\cosh\lambda) = 0\end{aligned} \tag{4-18}$$

The ζ_r in Equation 4-2 is obtained from [49],

$$\zeta_r = \frac{\sin\lambda_r - \sinh\lambda_r + \lambda_r(M_t/mL)(\cos\lambda_r - \cosh\lambda_r)}{\cos\lambda_r + \cosh\lambda_r - \lambda_r(M_t/mL)(\sin\lambda_r - \sinh\lambda_r)}. \tag{4-19}$$

The C_r in Equation 4-2 is a modal constant which should be evaluated by normalizing the eigenfunctions according to the following orthogonality conditions

$$\int_0^L \phi_s(x) m \phi_r(x) dx + \phi_s(L) M_t \phi_r(L) + \left[\frac{d\phi_s(x)}{dx} I_t \frac{d\phi_r(x)}{dx}\right]_{x=L} = \delta_{rs}\,, \tag{4-20}$$

$$\int_0^L \phi_s(x) YI \frac{d^4\phi_r(x)}{dx^4} dx - \left[\phi_s(x) YI. \frac{d^3\phi_r(x)}{dx^3}\right]_{x=L} + \left[\frac{d\phi_s(x)}{dx} YI \frac{d^2\phi_r(x)}{dx^2}\right]_{x=L} = \omega_r^2 \delta_{rs}, \tag{4-21}$$

Here, I_t is the rotary inertia of the tip mass, M_t and δ_{rs} is the Kronecker delta (defined to be equal to unity for $s = r$ and equal to zero for $s \neq r$). It has to be mentioned that the undamped natural frequencies are obtained from [42],

$$\omega_r = \lambda_r^2 \sqrt{\frac{YI}{mL^4}}. \tag{4-22}$$

For a single piezoceramic layer operating in a circuit of admittance $1/R_l$ the coupled electrical circuit equation is obtained from the following relation [42].

$$\frac{d}{dt}\int D.ndA = \frac{v(t)}{R_l}, \tag{4-23}$$

where $v(t)$ is the voltage across the electrodes of the piezoceramic, D is the vector of electric displacement components, n is the unit outward normal. Also, the integration is performed over the electrode area A. The relevant component of the electric displacement to be used in the inner product of the integrand is,

$$D_3 = e_{31}S_1 + \varepsilon_{33}^S E_3 \,, \tag{4-24}$$

where D_3 is the electric displacement component and ε_{33}^S is the permittivity component at constant strain [42]. Note that the axial strain component S_1 introduces the beam deflection $w_{rel}(x,t)$ to the circuit equation through Equation 4-7, so that Equation 4-24 yields a coupled electrical circuit equation. The coupled distributed parameter equations for the cantilevered piezoelectric energy harvester configurations shown in Figure 4-2 and their closed-form solutions are derived in the following sections.

4.2.1. Bimorph Configurations

Depending on the poling directions of the piezoceramic layers and the connection of the electrode leads, the electrical outputs of the piezoceramic layers can be combined in series or in parallel for bimorph cantilevers[42]. Although the bimorph configurations shown in Figure 4-4 have the same geometric and material properties, yet different combinations of the piezoceramic layers in the electrical circuit (in series or in parallel) changes not only the voltage response across the resistive load, but also the coupled vibration response. The coupled models of these two bimorph configurations are derived in the following sub-sections.

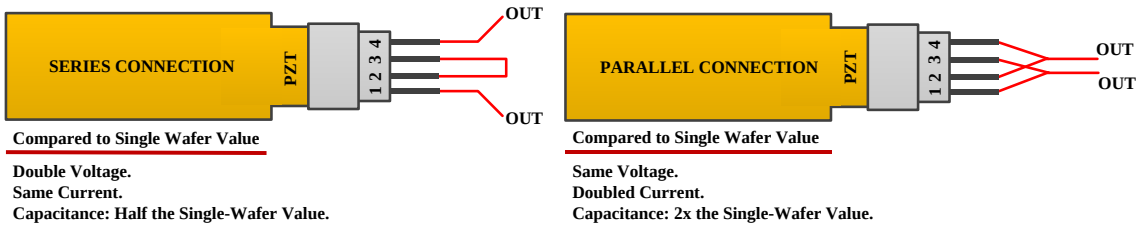

Figure 4- 4. Comparison between a bimorph and unimorph connection [42]

4.2.1.1. Bimorph Cantilevers in Series Connection

After expressing the coupled beam equation in the physical coordinates, the modal expansion and the orthogonality conditions of the vibration modes can be used to obtain,

$$\ddot{\eta}_r^{bs}(t) + 2\zeta_r\omega_r\dot{\eta}_r^{bs} + \omega_r^2\eta_r^{bs}(t) + \chi_r^{bs}v_{bs}(t) = f_r(t)\,, \tag{4-25}$$

where $\eta_r^{bs}(t)$ is the modal mechanical response of the bimorph cantilever. It has to be mentioned that subscript bs stands for a bimporph PZT beam in connected in series connection. $v_{bs}(t)$ is the voltage across the resistive load. $f_r(t)$ is the modal mechanical forcing function due to base excitation and χ_r^{bs} is the backward modal coupling term given by,

$$\chi_r^u = \vartheta_{bs}\left(\frac{d\phi_r(x)}{dx}\right)_L\,, \tag{4-26}$$

And,

$$\vartheta_{bs} = \frac{e_{31}b}{2h_p}\left[\frac{h_{pb}^2}{4} - \left(h_{pb} + \frac{h_{sb}}{2}\right)^2\right], \tag{4-27}$$

is the coupling term in the physical equation. Here *b* is the width of the beam, h_{pb} and h_{sb} is the thickness of the piezoceramic and the substructure layers. The electrical circuit equation for the series connection case is,

$$\frac{C_{pb}}{2}\dot{v}_{bs}(t) + \frac{v_{bs}(t)}{R_l} = i_p^{bs}(t), \tag{4-28}$$

where the internal capacitance and the current source terms are,

$$C_{pb} = \frac{\varepsilon_{33}^S bL}{h_{pb}}\, i_p^{bs}(t) = \sum_{r=1}^{\infty}\varphi_r^b\dot{\eta}_r^{bs}(t)\,, \tag{4-29}$$

Respectively, the forward modal coupling term for the bimorph configuration is,

$$\varphi_r^b = -\frac{e_{31}b\left(h_{pb}+h_{sb}\right)}{2}\int_0^L \frac{d^2\phi_r(x)}{dx^2}dx = = -\frac{e_{31}b\left(h_{pb}+h_{sb}\right)}{2}\left(\frac{d\phi_r(x)}{dx}\right)_L. \quad (4\text{-}30)$$

Equations 4-18 and 4-21, are the coupled equations for the modal mechanical response $\eta_r^{bs}(t)$ of the bimorph and the voltage response $v_{bs}(t)$ across the resistive load. If the translational and rotational components of the base displacement are harmonic in the forms of $g(t) = Y_0 e^{j\omega t}$ and $h(t) = \theta_0 e^{j\omega t}$, then the modal mechanical forcing function becomes $f_r(t) = F_r e^{j\omega t}$, where F_r is given by,

$$F_r = \omega^2\left[m\left(Y_0\int_0^L \phi_r(x)dx + \theta_0\int_0^L x\phi_r(x)dx\right) + M_t\phi_r(L)(Y_0 + L\theta_0)\right]. \quad (4\text{-}31)$$

The steady state voltage response across the resistive load can then be obtained as

$$v_{bs}(t) = \frac{\sum_{r=1}^{\infty}\frac{j\omega\phi_r^b F_r}{\omega_r^2 - \omega^2 + j2\zeta_r\omega_r\omega}}{\frac{1}{R_l} + j\omega\frac{C_{pb}}{2} + \sum_{r=1}^{\infty}\frac{j\omega\varphi_r^b\chi_r^{bs}}{\omega_r^2 - \omega^2 + j2\zeta_r\omega_r\omega}}e^{j\omega t}. \quad (4\text{-}32)$$

4.2.1.2. Bimorph Cantilevers in Parallel Connection

The coupled equation of motion for the modal mechanical response can be obtained as

$$\ddot{\eta}_r^{bp}(t) + 2\zeta_r\omega_r\dot{\eta}_r^{bp} + \omega_r^2\eta_r^{bp}(t) + \chi_r^{bp}v_{bp}(t) = f_r(t), \quad (4\text{-}33)$$

where $\eta_r^{bp}(t)$ is the modal mechanical response of the bimorph cantilever for parallel connection of the piezoceramic layers and $v_{bp}(t)$ is the voltage across the resistive load. It has to be mentioned that the subscript bp, stands for a bimorph PZT beam connected in parallel conection.The modal mechanical forcing function $f_r(t)$ is same as in the series configuration and the backward modal coupling term is given by

$$\chi_r^{bp} = \vartheta_{bp}\left(\frac{d\phi_r(x)}{dx}\right)_L, \tag{4-34}$$

where the coupling term in the physical domain can be given by

$$\vartheta_{bp} = \frac{e_{31}b}{h_{pb}}\left[\frac{h_{sb}^2}{4} - \left(h_{pb} + \frac{h_{sb}}{2}\right)^2\right]. \tag{4-35}$$

Here, b is the width of the beam, h_{pb} and h_{sb} are the thickness of the piezoceramic and the substructure layers of the bimorph configuration displayed in Figure 4-2-c, respectively. The electrical circuit equation for the parallel connection case is

$$C_{pb}\dot{v}_{bp}(t) + \frac{v_{bp}(t)}{2R_l} = i_p^{bp}(t), \tag{4-36}$$

where the initial capacitance and the current source terms are

$$C_{pb} = \frac{\varepsilon_{33}^S bL}{h_{pb}} \quad i_p^{bp}(t) = \sum_{r=1}^{\infty} \phi_r^b \dot{\eta}_r^{bp}(t)\,. \tag{4-37}$$

Equations 4-30 and 4-28 constitute the coupled equations for the modal mechanical response $\eta_r^{bp}(t)$ of the bimorph and the voltage response $v_{bp}(t)$ across the resistive load. For harmonic base motions, one can obtain the steady state voltage response across the resistive load as

$$v_{bp}(t) = \frac{\sum_{r=1}^{\infty} \frac{j\omega\phi_r^b F_r}{\omega_r^2 - \omega^2 + j2\zeta_r\omega_r\omega}}{\frac{1}{2R_l} + j\omega C_{pb} + \sum_{r=1}^{\infty} \frac{j\omega\varphi_r^b \chi_r^{bp}}{\omega_r^2 - \omega^2 + j2\zeta_r\omega_r\omega}} e^{j\omega t}, \tag{4-38}$$

The output power of the piezoelectric beam when connected to a resistive load, R_L, is given by

$$P = \frac{v_{bp}^2}{R_L}. \tag{4-39}$$

The energy harvesting application which is presented in this thesis is based on the tip mass gravitational force fluctuations in a rotational motion. Chapter 5 describes the mathematical framework for modeling our proposed energy harvester.

5. Electromechanical Modeling of a Tangentially-Rotating Cantilever Beam

The device proposed in this study works on the simple principle that the dynamic motion of a spring/mass system, when transferred to a PZT beam, can generate the required voltage in order to self-power wireless sensors typical of smart tire applications. In what follows, we first present the mathematical framework and the equations governing the performance of three different energy-harvesting systems. The numerical method of solution will then be described in some details. I will then proceed with describing the experimental setup and the fabrication of a prototype of our novel energy-harvesting system. The experimental setup will be used to evaluate the performance of this prototype and the validity of the numerical results.

We start with the dynamic modelling of a Cantilever type piezoelectric beam mounted on the inner side of a wheel/hub. The dynamic behaviour of such a system will be investigated and its drawbacks will be highlighted. We will then go one step forward and introduce a system of linear spring/mass and employ a feasibility analysis on whether the spring/mass system can broaden the frequency bandwidth by simulating the system under a base excitation. Three possible scenarios of manipulating the spring/mass system on the harvesting mechanism would be analysed and compared. The relevance of the analytical study will be checked by an experimental study conducted on an energy harvesting prototype using a spinning wheel test setup, specifically designed and manufactured for our studies. Mathematical Modeling of a Rotating Piezoelectric Cantilever Beam

In this part, a mathematical model of a tangent PZT cantilever beam mounted on the inner part of a rotating hub will be presented. This model will provide us with a relationship between the mechanical stress, the deflection invoked within the PZT beam, and the rotary speed of the reference hub. It also relates them to the induced voltage and power from the piezoelectric beam. With this in mind, a coupled dynamical model is

developed for a rotating cantilever beam. The model is then integrated with valid electrical circuit equations. Altogether, they are expected to model the piezoelectricity behaviour of the cantilever beam. The equations so-obtained will be solved to derive a closed form solution for the vibration response of such systems. The objective is to investigate the effect of tip mass on the performance of the harvesting mechanism. A shear and stress analysis will be carried out to verify the safety of the device under normal operating conditions.

As mentioned before, the energy harvester developed in this thesis work is typically a cantilever beam which is carrying a tip mass payload as shown in Figure 5-1. The cantilever beam contains equally-distributed layers of piezoelectric materials mounted on both sides of the beam covering its entire length. Our numerical studies are obtained under the assumption that the hub rotates at a constant angular velocity. Thereby, as the hub rotates, gravity will be the only effective force affecting the harvesting mechanism. As shown in Figure 5-1, the hub is rotating about the 'Z' axis, and gravity is acting along the negative 'Y' axis.

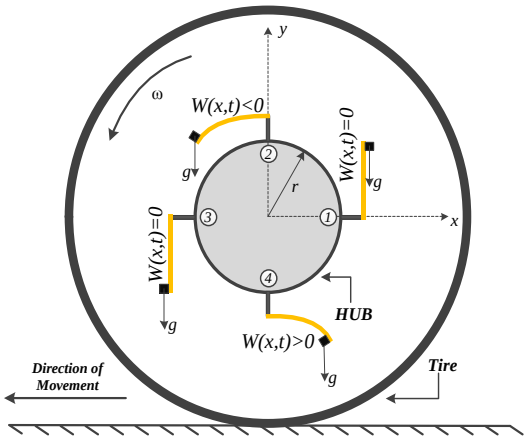

Figure 5- 1. Schematic view of the energy harvester for rotary motion applications

The concept is clearly shown in Figure 5-1 for one cycle of rotation of the cantilever beam. When the beam is in position (1), the bending moment induced by the existing gravitational force is zero. As the beam reaches position (2), the gravitational force caused by the tip mass applies a bending moment on the cantilever beam in '+Z' direction which in fact induces stress and deformation on the beam. As the beam passes this point and reaches position (3) the effect of gravitational force would be identical to

(1). Correspondingly, at position (4), the gravitational force caused by the tip mass would again induce a bending moment yet this time in '–Z' direction. As a result, a full turn of the hub applies an alternating force on the energy harvesting mechanism. It has to be mentioned that the frequency of the force alternation clearly matches the hub rotation frequency. In practice, the induced voltage generated by the vibrations (resulted from the rotary movement of the hub) would create a harmonic signal which is a function of the strain sustained by the piezoelectric beam, as well.

The following analytical modal analysis is given for the linear transverse vibrations of an undamped Euler–Bernoulli beam with clamped–free boundary conditions and a tip mass rigidly attached at the free end. The expressions for the undamped natural frequencies and mode shapes are obtained and the normalization conditions of the eigenfunctions are given. The procedure for reducing the partial differential equations of motion to an infinite set of ordinary differential equations is summarized and it will be applicable to proportionally-damped systems, as well.

5.1.1. Dynamic Modeling of the Rotating Beam

The mathematical modeling of the proposed mechanism is simplified if it can be assumed that the Euler-Bernoulli beam equations are valid for the PZT ceramic beam. A Lagrangian approach can then be used to develop the governing equation(s). Modeling is carried out for the case in which the tire's hub is rotating at constant angular velocity. For small deformations, the undamped partial differential equation describing the deflection of the PZT beam is given by [49]

$$EI\frac{\partial^2 w(x,t)}{\partial t^2}+\rho A\frac{\partial^4 w(x,t)}{\partial x^4}=0, \tag{5-1}$$

where $w(x,t)$ is the beam's deflection, E is the Young's modulus, I is the area moment of inertia, ρ is the mass density, and A is the cross-sectional area of the beam. As stated before, the piezoelectric layers cover the whole length of the beam resulting in constant values of EI and ρA. In order to numerically solve the above equation, we have decided to rely on the Rayleigh-Ritz method to approximate the fundamental natural

frequency of the piezoelectric beam [13]. Based on this method, the displacement of the beam is written as a summation of *N* mode shapes [11], [12]; that is,

$$w(x,t) = \sum_{i=1}^{N} \phi_i(x) q_i(t) \tag{5-2}$$

where $\phi_i(x)$ is the assumed mode shape (which is set such that it satisfies any combination of boundary conditions), $q_i(t)$is the temporal coordinate of the displacement (which has a solution of the form $q_i(t) = e^{j\omega t}$) and N is the number of modes. By substituting Equation 5-2 into Equation 5-1 , the equation of motion can be re-written as,

$$c^2.\left(\frac{\phi''''(x)}{\phi(x)}\right) = -\left(\frac{\ddot{q}(t)}{q(t)}\right) = \omega_n^2, \tag{5-3}$$

where $c^2 = \sqrt{EI/\rho A}$, and ω_n is the natural frequency of the beam. Equation 5-3, has a solution of the form,

$$\phi(x) = a_1 \sin(\beta x) + a_2 \cos(\beta x) + a_3 \sinh(\beta x) + a_4 \cosh(\beta x) \tag{5-4}$$

This equation describes the mode shape of the PZT beam. As to the boundary conditions for Equation 5-4, we specify an infinite set of values for β and each β determines a specific eignefrequency ω of the beam through the following equation,

$$\omega^2 = \frac{\beta^4 EI}{\rho A}, \tag{5-5}$$

The unknown constants in Equation 5-4 can be calculated by invoking the boundary conditions. For the current model, the boundary conditions are listed in Table 5-1, where m is the load mass.

Table 5- 1. Boundary Conditions involved within the PZT beam

$\boldsymbol{Position}$	$\boldsymbol{Boundary\ Condition\ \#1}$	$\boldsymbol{Boundary\ Condition\ \#2}$
$x = 0$	$Deflection: \phi(x) = 0$	$Slope: d\phi/dx = 0$
$x = L$	$Bending: d^2\phi/dx^2 = 0$	$Shear: d^3\phi(x)/dx^3 = -(m\beta^4)/\rho A\phi(x)$

The four boundary conditions in Table 5-1 yield four equations for the four unknown coefficients. This coefficient matrix has to be singular in order to obtain non-

trivial values. Setting the determinant of the coefficient matrix equal to zero, gives the *characteristic equation* of the differential eigenvalue problem and one could solve for positive values of β.

Figure 5-2 symbolizes the flexible cantilever beam energy harvesting system under rotational motion. In this schematic, R corresponds to the position of an infinitesimal segment on the beam in the rotating coordinate system, and r is the radius of the rotating hub. Therefore, we have,

$$R = \big(r + w(x,t)\big)i' + vj' \tag{5-6}$$

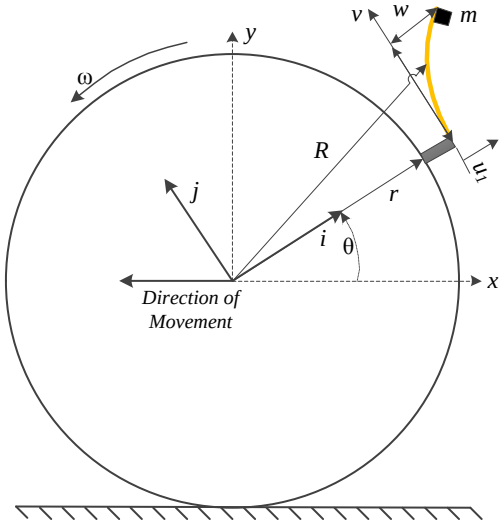

Figure 5- 2. Rotating Flexible beam mass system

To numerically solve the governing equation, i.e., Equation 5-1, we have decided to rely on the "method of assumed modes" in a Lagrangian framework [72], [73]. This method allows for the equations of motion of even complicated systems to be derived without using free-body force and moment diagrams. The Lagrange formulation follows from variational principles and states that the mathematical model describing the dynamics of the beam structure can be written as,

$$\frac{d}{dt}\left(\frac{\partial T}{\partial \dot{q}_i}\right) - \frac{\partial T}{\partial q_i} + \frac{\partial U}{\partial q_i} = Q_i + F_i, \tag{5-7}$$

where $\partial/(\partial\dot{q}_i)$ is the derivative with respect to the generalized velocity, T is the total kinetic energy, U is the potential energy, Q_i represents all non-conservative forces corresponding to q_i, and F_i indicates the moments induced by the piezoelectric beam respectively. To implement the Lagrangian formulation, however, one needs the kinetic and potential energy terms of the substructure first. What follows next is the procedures taken into account for finding these parameters for each of the three conceptual designs.

For the velocity of an infinitesimal segment on the PZT beam having a position R in a rotating coordinate system, we can write,

$$\vec{\dot{R}} = \frac{\overrightarrow{dR}}{dt} + \dot{\theta}k' \times \vec{R} \rightarrow = \left(\frac{\partial r}{\partial t} + \frac{\partial w}{\partial t}\right) i' + \left(\frac{\partial v}{\partial t}\right) j' + \dot{\theta}k' \times (vj'), \tag{5-8}$$

This in fact, results to the following equation,

$$\vec{\dot{R}} = \left(\dot{w} - v\dot{\theta}\right) i' + (r + w)\dot{\theta}\, j'. \tag{5-9}$$

Knowing the velocity of each infinitesimal segment on the beam from the above equation, one can proceed with its integration along the beam and obtain the kinetic energy of the beam as,

$$T_{beam} = \frac{1}{2}\rho A \int_0^l \left|\vec{\dot{R}}\right|^2 dx = \frac{1}{2}\rho A \int_0^l \left(\left(\dot{w} - v\dot{\theta}\right)^2 + \left((r + w)\dot{\theta}\right)^2\right) dx. \tag{5-10}$$

As to the load mass, it has a translational kinetic energy which is equal to,

$$T_{mass} = \frac{1}{2} m \left[\left(\phi_L \dot{q} - L\dot{\theta}\right)^2 + \left((r + \phi_L q)\dot{\theta}\right)^2\right], \tag{5-11}$$

where ϕ_L, represents the mode shape of the beam at coordinate $x = L$. The potential energy of the beam structure can be expressed as

$$U_{beam} = g\rho A \int_0^l (rsin\theta + vcos\theta + wsin\theta) dx + \frac{1}{2} EI \int_0^l \left(\frac{\partial^2 w}{\partial x^2}\right)^2 dx, \tag{5-12}$$

The potential energy related to the tip mass is defined by

$$U_{mass} = mg(rsin\theta + lcos\theta + \phi_l qsin\theta), \tag{5-13}$$

The generalized applied forces involved in the model, which is typically the moment induced by the piezoceramic beam, can be described as [15],

$$F_i = k_{pzt} v(t) \begin{bmatrix} \phi_1'(0) - \phi_1'(l) \\ \vdots \\ \phi_i'(0) - \phi_i'(l) \end{bmatrix}, \tag{5-14}$$

According to Equation 5-14, it should be noted that the torque generated is clearly a function of the voltage $v(t)$ generated inside the PZT beam. Also, the term k_{pzt} in Equation 5-14, which is known as the backward coupling term, is given by [15],

$$k_{pzt} = \frac{h_1 t_z (t_z + 2h_1) E_z}{h_1^3 + \left((t_z^3 + 3h_1 t_z^2 + 3h_1^2 t_z) E_z\right)/E} w_1 h_1^2 \frac{d_{31}}{t_z}, \tag{5-15}$$

where d_{31} is the charge constant, E and E_z are the modulus of elasticity of the beam and PZT, respectively. In this equation, $h_1$is the half-thickness of the beam, w_1 is the width of the beam, and t_z is the thickness of the piezoelectric layer. Knowing the geometric parameters of our PZT beam, Equation 5-15 becomes

$$k_{pzt} = \frac{E_z d_{31} b_1 t}{14}. \tag{5-16}$$

Applying the Lagrangian formulation for all generalized coordinates would leads us to define the dynamic simulation of the model. This can be expressed as,

$$C_1 \ddot{q} + C_2 q + C_3 = F(t), \tag{5-17}$$

where $C_1, C_2$and C_3 are given by Table 5-2.

Table 5- 2. Coefficients of the matrix describing the dynamics of the system

Coeffcient	***Value***	***Defenition***

$\boldsymbol{C_1}$	$m\phi_l^2 + \rho AM$	$Eeffective\ Mass$
$\boldsymbol{C_2}$	$EIK_{eq} - \rho AM\dot{\theta}^2 - m\phi_l^2\dot{\theta}^2$	$Coriolis\ Force$
$\boldsymbol{C_3}$	$gsin\theta(\rho A\varphi + m\phi_l) - \dot{\theta}^2(mr\phi_l + \rho Ar\varphi)$	$Gravitational\ and\ Centrifugal\ Force$

where M and φ are obtained from,

$$M = \int_0^l \phi^2(x)dx\ , \qquad \varphi = \int_0^l \phi(x)dx. \tag{5-18}$$

In Table 5-2, K_{eq} represents an effective stiffness for the PZT beam, which is determined as,

$$K_{eq} = \int_0^l \left(\phi''(x)\right)^2 dx, \tag{5-19}$$

In the next section, we shall represent the electrical model of the energy havrvesting device and introduce the coupling term which provides us with a series of coupled electromechanical formulations necessary for our numerical studies**.**

5.1.1.1. Coupled Electrical Model of the PZT Energy Harvester

The next step is to obtain the electro-mechanical equations of the piezoelectric transducer. The piezoelectric layers of a symmetric PZT beam can be connected in series or in parallel depending on the application [15]. Figure 5-3 shows the parallel configuration in which each piezoceramic layer can be represented by a current source in parallel with its internal capacitance [20].

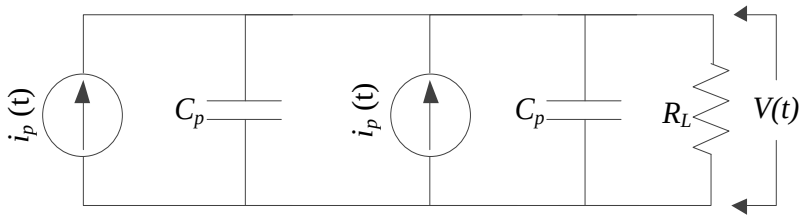

Figure 5- 3. Electrical circuit symbolizing the parallel connection of PZT layers

In a practical situation, the output voltage is rectified and conditioned by the converter circuit for storing the harvested power in a storage media such as a large capacitor. The purely resistive electrical load provides a practical way for calculating the power generated form the harvester. These equations now represent the electro-mechanical system and can be used to determine the motion of the beam.

The electrical circuit equation of the system (considering only the first mode of vibration) can be obtained by using the Kirchhoff's law as [74].

$$C_p\dot{v}(t) + \frac{v(t)}{2R_L} = i_p(t), \tag{5-20}$$

The output current of the PZT beam, which is a function of its strain, can be given by [28],

$$i_p(t) = -\frac{1}{2}d_{31}E_z b_1 t_h \int_0^l \frac{\partial^3 w(x,t)}{\partial x^2 \partial t}dx = -\frac{1}{2}d_{31}E_z b_1 t_h \sum_{i=1}^{n} \phi_i'(l)\dot{q}_i(t) = \gamma\dot{q}_i(t) \tag{5-20}$$

where R_L is the load resistance,$C_p = (\varepsilon_{33}^S bL)/h_p$ is the internal capacitance of piezoelectric layer, $\gamma = -d_{31}E_z b_1 t_h \phi'(l)/2$ is the forward coupling term, ε_{33}^S is the permittivity constant, b, L and h_p are the width, length, and thickness of the piezo-ceramic layer, respectively, d_{31} is the piezoelectric constant, and S_{11}^E is the elastic compliance at a constant electric field.

5.1.1.2. Undamped Coupled Electromechanical Model

By combining the electrical model with the equations governing the dynamics of the system, the final undamped coupled electromechanical model can be derived for the

energy harvesting mechanism. The single mode electromechanical model of the aforementioned system could be given by

$$\begin{cases} (m\phi_l^2 + \rho AM)\ddot{q}(t) + \left(EIK_{eq} - \rho AM\dot{\theta}^2 - m\phi_l^2\dot{\theta}^2\right)q(t) + k_{pzt}\varphi_l' v(t) \\ \qquad = -gsin\theta(\rho A\varphi + m\phi_l) \\ C_p\dot{v}(t) + \dfrac{v(t)}{2R_L} = \dfrac{d_{31}E_z w t_h}{2}\varphi_l'\dot{q}(t) \end{cases} \tag{5-21}$$

In the next section, we present the numerical results obtained having solved Equation 5-21. We have applied the fourth-order Runge-Kutta method in the SIMULINK/MATLAB code to solve this system of equations. Our main objective is to investigate the feasibility of the proposed energy harvesting mechanism in rotary motion applications. The frequency response of the mechanism will be sought for using a frequency sweeping process. The data presented in Table 5-3 have been used in our simulations. It has to be mentioned that the data used here where extracted from a real piezoelectric beam which has been briefly introduced in section (6.4).

Table 5- 3. Values used for the numerical study

$\boldsymbol{Symbol}$	$\boldsymbol{Description}$	$\boldsymbol{Value}$	$\boldsymbol{Unit}$
t	$Thickness$	0.762	mm
b	$Width$	33.2	mm
l	$Length$	460	mm
E	$PZT\ Young's\ modulus$	28.4	N/m^2
ρ	$Density$	7800	kg/m^2
d_{31}	$Coupling\ coefficient$	-190	$\rho m/V$
ε_{33}	$Electrical\ Permittivity$	1500	F/m
R_L	$Load\ Resistance$	40	$k\Omega$
r	$Radious\ of\ HUB$	350	mm

5.2. Tip mass Effect on Harvesting Mechanism

Figure 5-4 shows the effect of tip mass on the natural frequency of the energy harvester and the amplitude of the output voltage. Different values of tip mass, in the range of $40\ gr$ to $60\ gr$ have been selected for this study. This range of tip mass was deemed appropriate for acquiring resonance frequencies from the energy harvester

substructure in a typical vehicle. In practice, this range of tip mass values brought some drawbacks which will be briefly discussed in the following sections. As it can be seen in Figure 5-4, by an increase in the tip mass, the resonance frequency of the substructure is decreased; that is, the substructure will resonate at lower rotational velocities of the vehicle.

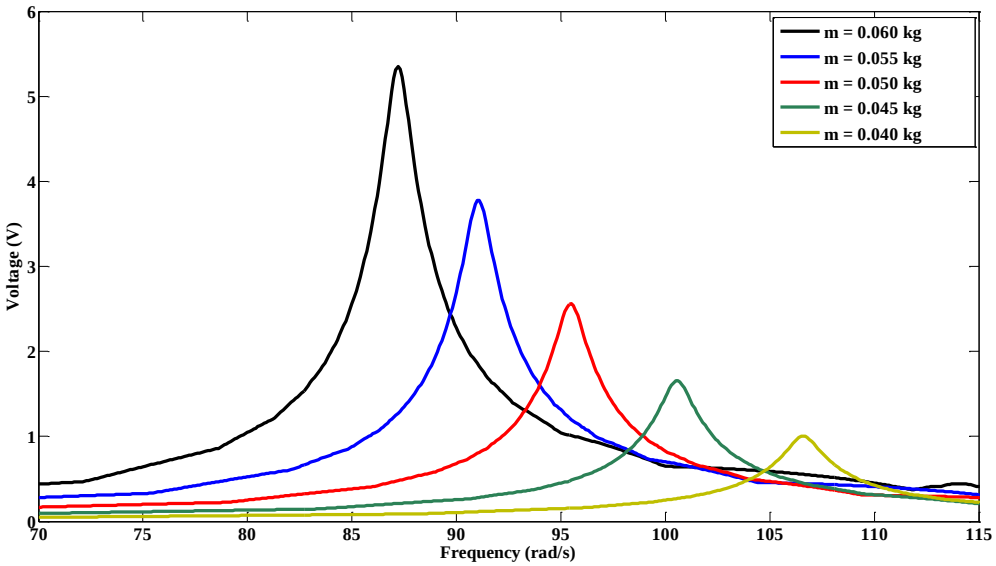

Figure 5- 4. Effect of tip mass on the acquired voltage and resonance frequency

5.3. Effect of Load Mass on the Generated Voltage

Figure 5-5 shows the effect of the tip mass on the voltage output of the energy-harvesting mechanism. As it can be seen in this figure, by increasing the tip mass, the voltage output of the device is increased, somewhat exponentially. This figure confirms the notion that one could boost up the voltage output from roughly $1v$ to roughly $6v$ by simply adding a $20gr$ tip mass.

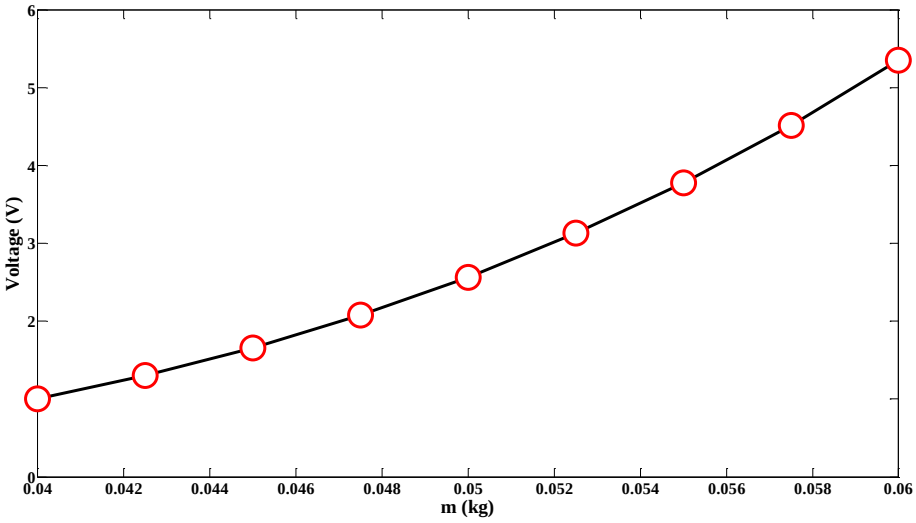

Figure 5- 5. Effect of tip mass on the acquired voltage

5.4. Effect of Load Mass on the Frequency Response

Figure 5-6 states the fact that by increasing tip mass values from $40gr$ to values up to $60gr$ would result in a very slight decrease in the resonanting frequency of the energy harvesting substructure and yielding the resonating frequency drop from values around $108\,rad/s$ to values around$88\,rad/s$.

This very slight change in the resonance frequency could be stated to role as a defecting character for this proposed design since one should add up high orders of tip mass values in order to obtain and see a major deviation in the resonating frequency of the system substructure. In other words, one could envisage the fact that this system is hardly tunable and hard to design to meet the objectives. Moreover, according from our observations from Figure 5-5 and 5-6, one could see that it is possible to obtain high orders of voltages by simply adding up tip mass values on to the structure. On the other hand figure 5-5 states the fact that for having high orders of voltage, large amount of load masses ($100\ gr$), should be used. This may not be a problem when considering the problem in an analytical point of view, but there could be limitations due to safety factors and maximum shear stress the PZT beam could handle. This fact yields us to say that we may not be able to add load mass as much as we wish.

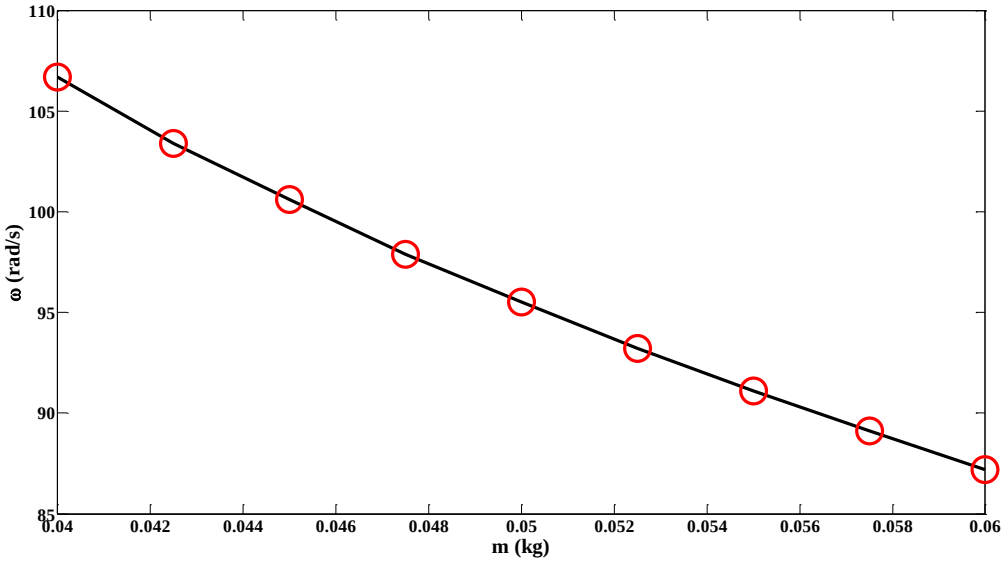

Figure 5- 6. Effect of tip mass on the resonance frequency

As it can be inferred from equation 5-21, there exists a direct relationship between the tip mass and the centrifugal force acting on the edge of the beam. The centrifugal force caused by the tip mass is equal to $F_{cent} = mr\omega^2$. In this equation r is the radius of the hub, and ω is the rotational velocity the tip mass is undergoing. The contour of the centrifugal force resulted by such tip mass is shown in Figure 5-7; (The color bar indicates the magnitude of the force). As it can be seen in this Figure 5-7, tip mass values larger than $30\ gr$ could exert large forces on the beam substructure when subjected to high rotational speeds. In fact, for a design working with a tip mass value equal to $40gr$ (which would amount to a resonance frequency of $100\ rad/s$) the centrifugal force will be in the order of $100N$. Such a large force can be fatal to the substructure and cause the beam to break at high rotational speeds.

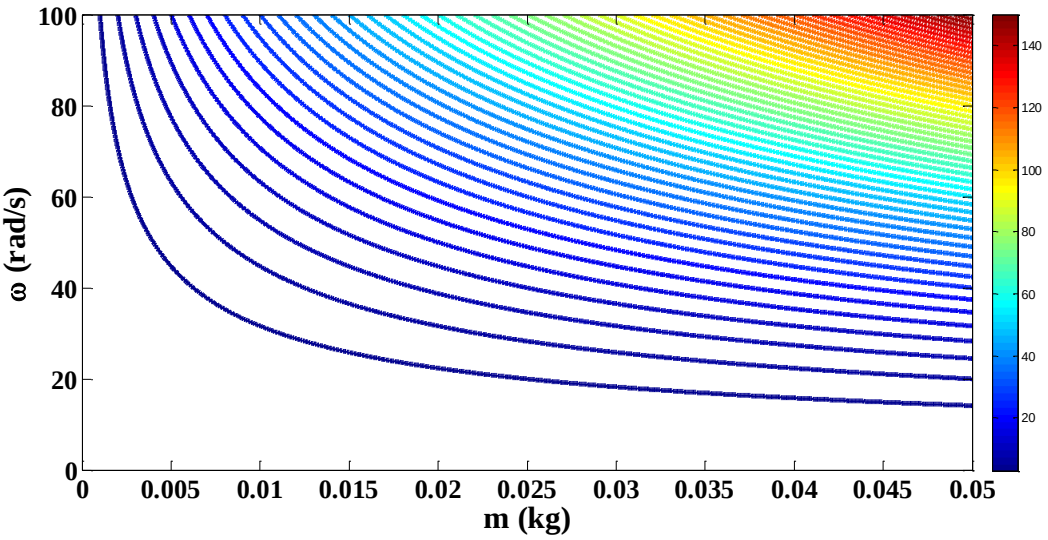

Figure 5- 7. Effect of tip mass on the centrifugal force acting on the beam

5.5. Safety Factor Analysis on the PZT Beam

As mentioned before, the purpose of this study was to introduce a trust-worthy energy-harvesting mechanism in the tire/hub of a vehicle. Having said this, one should note that a vehicle's safety and its passengers are more important than the energy-harvesting device and its purpose. Without a doubt, any sort of failure or breakage of energy-harvester is absolutely intolerable as it may result in a catastrophic accident injuring the passengers of that vehicle. To see if the design would meet safety concerns, the von-misses shear and stress analysis was done on the PZT cantilever beam. Safety factor (SF), is a term which indicates the structural integrity of a system beyond the expected loads or actual loads. In particular, safety factor describes to what extent a design is far from critical situations.

To calculate the safety factor, we have relied on an FEM commercial software known as SimulationExpress. The results of this software are based on linear static analysis and the material is assumed to be isotropic. Linear static analysis assumes that: (1) the material behavior is linear complying with the hooke's law, (2) induced displacements are adequately small to ignore changes in stiffness due to loading, and (3) loads are applied slowly in order to ignore dynamic effects. The results of such study are done for the case of a piezoelectric cantilever beam having a tip mass value equal to

$40gr$ undergoing a rotational velocity of 100 rad/s. This would expose the cantilever beam to a vertical force of roughly$100\,N$. Figure 5-8a indicates that the system would unfortunately have safety factors lower than 1 in most parts. It has to be mentioned that, in this figure, areas having safety factors less than 1 have been identified by the red color. From Figure 5-8a one can conclude that this system would definitely be prone to failure under such combination of rotational velocities and tip mass values. Figure 5-8b, also shows a von-misses shear and stress analysis on the same study which clearly indicates that the system would be prone to break near the edges of the holes.

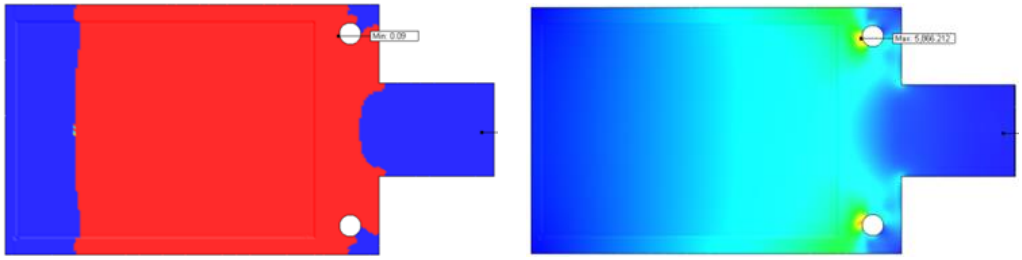

(a) (b)

Figure 5- 8. (a) safety factor of the beam (b) von-misses shear contour

5.6. Concluding Remarks

An investigation of the simple energy harvesting system introduced in this chapter revealed the fact that although the device is quite simple to fabricate, yet it suffers from certain drawbacks. The main drawback of the device is due to the single linear resonating character it offers. This forces the system to acquire tangible amount of power in one, and only one, frequency. Thus, the system would be inefficient when subjected to other frequencies. Another drawback of this mechanism was that it was not easily tuneable. Last, but not least, this system needs large load mass in order to generate adequate voltage in the required frequency spectrum. This makes the device quite prone to mechanical damage and breakage. In the following chapter, a new concept is introduced for an energy harvesting mechanism which can eliminate most of those drawbacks.

6. Feasibility Analysis of a Coupled Linear Resonating Energy Harvester for Broadening the Frequency Bandwidth

The previous design discussed in chapter 5, showed to be inefficient in terms of frequency tuning. It was also shown for the structure to produce high orders of voltage, utilization of high orders of tip mass values was necessitated. This fact made the structure to become prone to breakage. In the following chapter utilization of linear resonating structures has been investigated in order to see whether these structures could reduce the amount of load mass which are in need to be added for the structure to produce high orders of voltage in low frequencies. In order to investigate this fact, a feasibility analysis was first set by studying the structure under a base excitation motion. The reason of studying the system in a base excited study was due to the simplicity it had when deriving the governing equations the structure was undergoing. It has to be mentioned that the problem was investigated both experimentally and numerically.

Analytical modeling is an indispensable tool in the design and optimization of power harvesting devices. Figure 6-1 shows the three design concepts proposed in this work for harvesting the vibrational energy. The device is seen to be basically comprised of a spring/mass system in which the spring is attached to the base with a freely-ended flexible PZT ceramic beam attached to the mass itself. The spring/mass system undergoes an oscillatory motion as soon as the base undergoes harmonic excitation. The oscillatory motion of the base makes the flexible PZT ceramic film to vibrate thereby producing the required voltage. As mentioned above, a spring/mass system (see Figure 6-1-a) behaves like a linear resonator providing a narrow bandwidth in the frequency spectrum. Therefore, the voltage generated by the most basic system, as shown in Fig. 1a, cannot provide the required voltage over a broad range of frequencies. This shortcoming can be resolved by introducing an extra tip mass to the other end of the PZT beam (see Figure 6-1-b). The combined effect of the two masses provides an extra resonating frequency. In practice, it enables us to broaden the frequency bandwidth by

tuning the mechanical properties of the coupled spring/mass system. However, as it is discussed in Chapter 5, the extra tip mass can impose significant strain and stress to the substrate (particularly at high rotational velocities) causing catastrophic failure and breakage of the PZT beam. To avoid this, a third conceptual design was introduced by adding another spring to the system in addition to the previous resonator system (see Figure 6-1-c). This modification would result in the substructure to become more symmetric and rigid when subjected to rotational speed. The proposed mechanism is shown to be easily tunable to any required frequency spectrum and is expected to harvest power in a broad and satisfactory bandwidth.

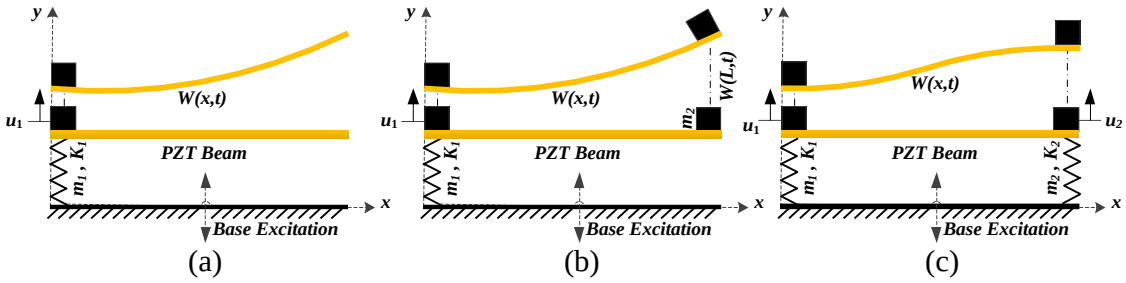

Figure 6- 1. Schematic showing the novel mass/spring mechanism proposed in this work, a) the basic system, b) the two-mass system, c) the two mass, two spring system

Table 6-1 shows a summary of the boundary conditions involved for each of the three design concepts depicted in Figure 6-1.

Table 6- 1. A summary of the boundary conditions involved for the three designs

Boundary Condition	$(B.C)_1: \left.\frac{d^2\phi(x)}{dx^2}\right\|_{x=l}$	$(B.C)_2: \left.\frac{d^2\phi(x)}{dx^2}\right\|_{x=0}$	$(B.C)_3: \left.\frac{d^3\phi(x)}{dx^3}\right\|_{x=l}$	$(B.C)_4: \left.\frac{d^3\phi(x)}{dx^3}\right\|_{x=0}$
Design #1	0	0	0	$\left(\frac{K_{s_1}}{EI}-\frac{m_1\beta^4}{\rho A}\right)\phi(x)$
Design #2	0	0	$-(\frac{m_2\beta^4}{\rho A})\phi(x)$	$\left(\frac{K_{s_1}}{EI}-\frac{m_1\beta^4}{\rho A}\right)\phi(x)$
Design #3	0	0	$\left(\frac{K_{s_2}}{EI}-\frac{m_2\beta^4}{\rho A}\right)\phi(x)$	$\left(\frac{K_{s_1}}{EI}-\frac{m_1\beta^4}{\rho A}\right)\phi(x)$

In this table, $K_{s_i}(i=1,2)$ corresponds to the spring stiffness involved in the system, and $m_i(i=1,2)$ are the tip masses present in the proposed system. By

imposing these four boundary conditions, four equations are obtained for the four unknown coefficients. For Design #3, to have a nonzero solution, the determinant of the coefficient matrix is set equal to zero.

$$\begin{bmatrix} 0 & -\beta^2 & 0 & \beta^2 \\ \beta^3 & H_1 & -\beta^3 & H_1 \\ \beta^2 sin\beta l & -\beta^2 cos\beta l & \beta^2 sinh\beta l & \beta^2 coshbl \\ H_2 sin\beta l + \beta^3 cos\beta l & H_2 cos\beta l - \beta^3 cosh\beta l & H_2 sinh\beta l - \beta^3 cosh\beta l & H_2 cosh\beta l - \beta^3 sinh\beta ll \end{bmatrix} \quad (6\text{-}1)$$

where H_1 and H_2 are equal to $\left(K_{s_1}/EI - (m_1\beta^4)/\rho A\right)$ and $\left(K_{s_2}/EI - (m_2\beta^4)/\rho A\right)$ correspondingly. Having solved this equation for β, the first root of β can then be found. One might envisage that for having the maximum voltage output, the resonance frequency of the beam should be tuned to the frequency of the spring/mass system. This tuning can be achieved by varying the values of the mass load and/or the spring stiffness. However, our results indicate that the natural frequency of the PZT beam automatically adjusts itself to the natural frequency of the spring-mass structure. As a matter of fact, the resonance frequency of the beam is found to be virtually the same as the resonance frequency of the spring/mass system. This can be attributed to the fact that the mass load, attached to the PZT beam, is much more dominant in dictating the dynamics of the whole system as compared to the PZT beam itself.

6.1. Governing Equations for Design #3

Since Design #2 and #3 are special cases of Design #3 (Figure 6-2), therefore it suffices to start with deriving the governing equations for this particular case. To that end, we start with finding the total kinetic and potential energies involved in the mechanism. An important assumption to be made here is that the direction of movement of each individual spring-mass structures are limited to only be moving in the vertical direction with respect to the excited base.

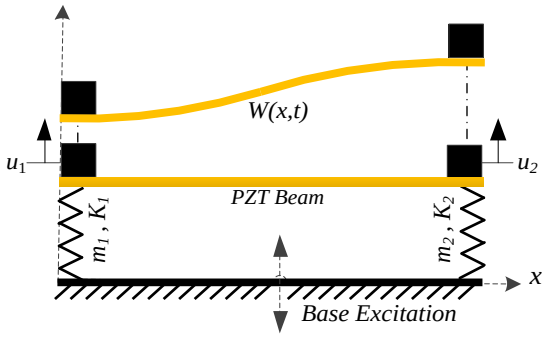

Figure 6- 2. The coordinate system used for design concept #3

The load masses have a translational kinetic energy equal to,

$$T_{m1} = \frac{1}{2} m_1 (\dot{u_1} - \phi_0 \dot{q})^2 \tag{6-2}$$

$$T_{m2} = \frac{1}{2} m_2 (\dot{u_2} - \phi_L \dot{q})^2 \tag{6-3}$$

where $w(x,t) = \phi(x)q(t)$ represents the coordinate system for the PZT beam, andu_1 and u_2 represent the coordinate system for the spring-mass structure. In this equation, ϕ_0 and ϕ_L represent the mode shape of the beam at $x = 0$ and $x = L$, respectively. Knowing the velocity of each infinitesimal segment on the beam and integrating along the beam, the kinetic energy of the beam can be obtained as,

$$T_{beam} = \frac{1}{2} \rho A \int_0^L \phi^2(x)\, \dot{q}^2 = \frac{1}{2} \rho A M \dot{q}^2 \tag{6-4}$$

where M is obtained from Equation 5-18. The potential energy of the springs can be found from,

$$U_{K1} = \frac{1}{2} . K_1 (u_1 - \phi_0 q - Y) \tag{6-5}$$

$$U_{K2} = \frac{1}{2} . K_2 (u_1 - \phi_L q - Y) \tag{6-6}$$

where $Y = Asin(\omega t)$ is the motion related to the base excitation, The total potential energy of the beam can be expressed as,

$$U_{beam} = \frac{1}{2}.EIK_{eq}q^2 \tag{6-7}$$

where K_{eq} represents an effective stiffness for the PZT beam, which is determined by Equation 5-19. The generalized applied forces involved in the model, which is typically the moment induced by the piezoceramic beam, can be described as [74]. Applying the Lagrangian formulation for all generalized coordinates would result in $i + 1$ equations for a complete dynamical simulation of the model. In matrix form, it can be expressed as,

$$C_1\begin{bmatrix}\ddot{u_1}\\ \ddot{u_2}\\ \ddot{q}\end{bmatrix} + C_2\begin{bmatrix}u_1\\ u_2\\ q\end{bmatrix} + C_3 = \begin{bmatrix}0\\ 0\\ F(t)\end{bmatrix}, \tag{6-8}$$

where C_1 is given by

$$C_1 = \begin{bmatrix} m_1 & 0 & -m_1\phi_0 \\ 0 & m_2 & -m_2\phi_L \\ -m_1\phi_0 & -m_2\phi_L & m_1\phi_0^2 + m_2\phi_L^2 + \rho AM \end{bmatrix} \tag{6-9}$$

In Equation 6-8, C_2 corresponds to the Coriolis and centrifugal terms, with C_3 indicating the gravitational force vector; they are given by,

$$C_2 = \begin{bmatrix} K_1 & 0 & -K_1\phi_0 \\ 0 & K_2 & -K_2\phi_L \\ -K_1\phi_0 & -K_2\phi_L & EIK + K_1\phi_0^2 + K_2\phi_L^2 \end{bmatrix} \tag{6-10}$$

$$C_3 = \begin{bmatrix} K_1 \\ K_2 \\ -K_1\phi_0 - K_2\phi_L \end{bmatrix} Y \tag{6-11}$$

6.2. Governing Equations for Design #2

Following the same procedure as shown above for the design concept #3, one could easily end up with the equations of motion for the design concept #2 and

investigate the dynamical behaviour of the system. In matrix form the formulation can be shown to be the form of,

$$C_1\begin{bmatrix}\ddot{u}_1\\ \ddot{q}\end{bmatrix}+C_2\begin{bmatrix}u_1\\ q\end{bmatrix}+C_3=\begin{bmatrix}0\\ F(t)\end{bmatrix}, \tag{6-12}$$

where C_1 is given by,

$$C_1=\begin{bmatrix}m_1 & -m_1\phi_0\\ -m_1\phi_0 & m_1\phi_0^2+m_2\phi_L^2+\rho AM\end{bmatrix}, \tag{6-13}$$

where ϕ_L corresponds to the assumed mode-shape at position $x=l$ of the PZT beam. In Equation 6-12, C_2 corresponds to the Coriolis and centrifugal terms, with C_3 indicating the gravitational force vector; which are given by,

$$C_2=\begin{bmatrix}K_1 & -K_1\phi_0\\ -K_1\phi_0 & EIK+K_1\phi_0^2\end{bmatrix} \tag{6-14}$$

$$C_3=\begin{bmatrix}K_1\\ -K_1\phi_0\end{bmatrix}Y \tag{6-15}$$

6.3. Governing Equations for Design #1

According to Figure 6-1, the only element which makes difference between concept design #1 and #2, is and extra tip mass involved in the system. As to this case solving the governing equations for the first concept, in a matrix format shall be the same as concept design#2, yet the coefficient $c_1$shall vary as follows,

$$C_1=\begin{bmatrix}m_1 & -m_1\phi_0\\ -m_1\phi_0 & m_1\phi_0^2+\rho AM'\end{bmatrix} \tag{6-16}$$

6.4. Experimental Setup

To investigate the validity of theoretical models developed in the previous section a prototype for each of the cases has been fabricated and tested on an electromagnetic shaker.

a PZT cantilever beam known as Volture PZT cantilevers is employed for as the energy harvester. Midé Technology Corporation produces the Volture line of piezoelectric vibration energy harvesters. The Volture cantilever piezoelectric films range in size from the V25W-ND (Figure 6-3) at 1.5 in. wide and 2.0 in. long down to the V22B-ND, which is only 0.24 in. wide and 1.4 in. long. Each Volture cantilever contains two piezoelectric wafers with individual output pins. These are most commonly connected in parallel to double the output current, but a series connection can be used to double the voltage and reduce the capacitance at the output.

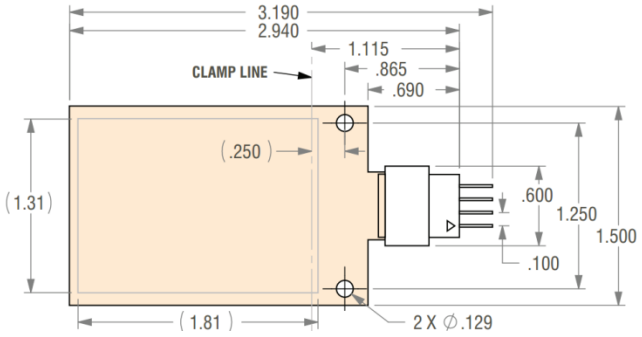

Figure 6- 3. Dimensions of the PZT cantilever beam used in the study (in inches)

A major feature of the Volture cantilevers is the robust packaging for the piezoelectric wafers (Figure 6-4). The protective skin offers a hermetically sealed unit for operation in harsh environments. However, care should still be taken to provide a smooth mounting surface free of burrs.

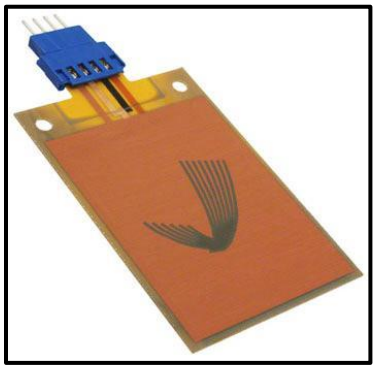

Figure 6- 4. Bimorph cantilever piezoelectric energy harvester

Figure 6-5 shows the final design to be mounted on shaker. To boost up the PZT beam's mechanical strength, we have decided to mount it on four parallel springs at each corner (see Figure 6-5-b). The stiffness coefficients of the springs used in this study were measured to be about 4250 N/m. It has to be mentioned that thin plastic type paper sheets were introduced in between the intersection of the PZT beam and the aluminum plates. Extra protective measures has been implemented to reduce (or eliminate) the risk of any sort of cut on the PZT beam (as might be caused by the edges of the aluminum plates).

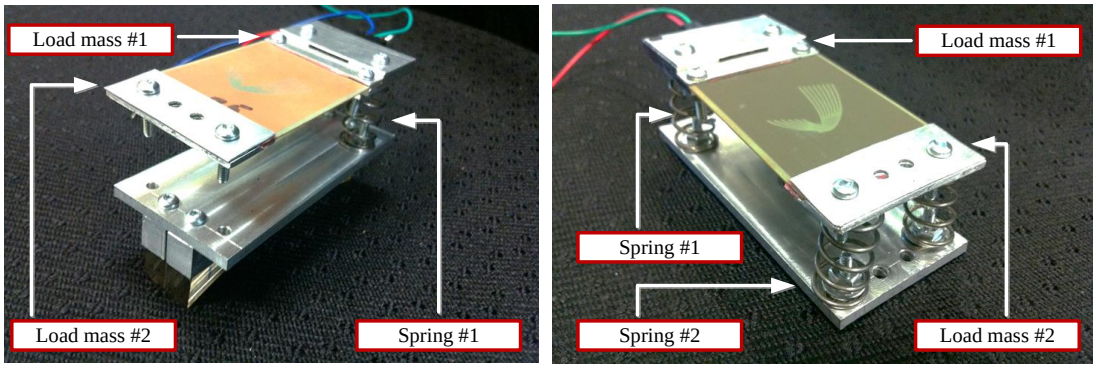

(a) (b)

Figure 6- 5. (a) Fabricated prototype of concept design #2 and (b) a fabricated prototype of Concept Design #3

The performance of the complete prototype energy-harvesting system, as shown in Figure 6-5, has been tested on a shaker. In order to study the frequency response of the system, the shaker is operated at a constant displacement. Figure 6-6 shows the LDS V455 permanent magnet shaker which was used in this study. The prototype of the

energy harvester device, which is mounted on the top of the shaker, can also be seen in this figure. The performances of the three proposed energy-harvesting models have been investigated using the experimental setup shown in Figure 6-6.

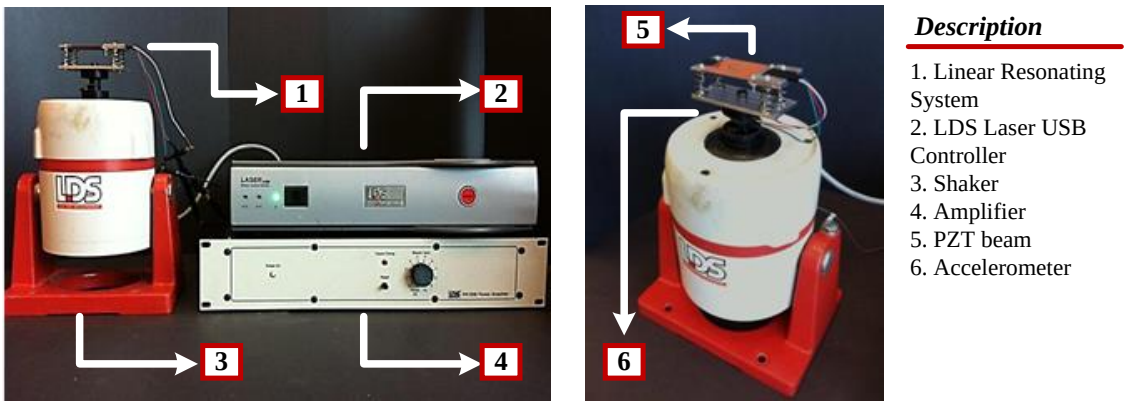

Figure 6- 6. The experimental setup used for the base excitation study

The setup shown in Figure 6-6 has been used to not only predict the amount of power produced by the PZT harvester (when subjected to transverse vibration), but also to identify the resonance frequencies of the substructure (i.e., where the amplitude of the voltage and power generated by the device are highest).

6.5. Results and Discussions (Proof of Concept)

In this section, we will present our numerical and experimental results obtained for the proposed energy harvesting designs depicted in Figure 6-1 and shall prove that our conceptual designs works as desired. We will start with presenting the experimental results and will show that our numerical simulations are readily capable of predicting the response of such system. It has to be mentioned that we have only focused on the analysis of two conceptual designs, since the prototype built for this project was incapable of predicting the study of systems consisting of only one tip mass.

Figure 6-7 shows the frequency response of the second configuration where a spring is coupled with two masses. This figure clearly shows the effect of the load mass on the frequency response of the system. As it can be seen in this figure, by increasing the load mass, the two narrow resonating frequencies get closer to each other resulting

in a wide bandwidth of sufficient voltage generation. Moreover, increasing the load mass values would also shift the resonating frequencies to lower values. Another interesting fact which can be observed from this experimental study was the increase in voltage generated as the two resonating frequencies merge and get close to each other. Overall, one can conclude that the system proposed would be working at its most efficient condition if the resonating frequencies are set in such a way that they are close to each other.

The experimental procedure has even enabled us to take the damping terms into account. To that end, we attached small load masses of equal value (having a mass of $m = 0.0165\ kg$) and kept the tip-mass and spring stiffness values constant in each case. In order to investigate the influence of the base excitation amplitude on the induced voltage in the PZT beam, the amplitude was varied from 0.1 to 0.25 mm for each case. As it can be seen by Figure 6-7, an increase in the amplitude of the excitation would result in the generation of higher voltage from the prototype.

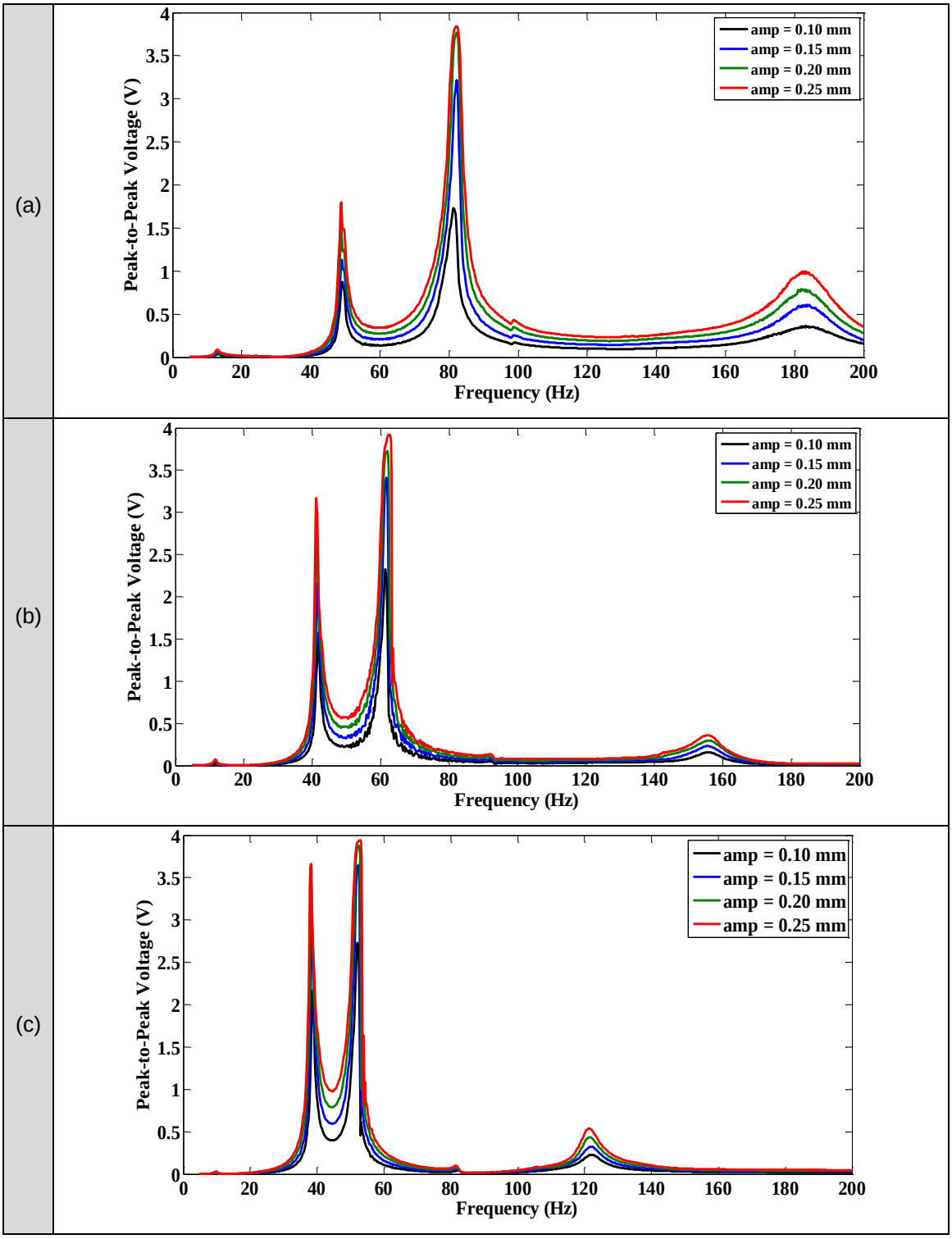

Figure 6- 7. Effect of load mass on frequency response of the design concept #2: (a) $m_l = m$, (b) $m_l = 2m$, (c) $m_l = 3m$.

Obviously, the third configuration (as depicted schematically in Figure 6-1-c) has superior performance over the design which was only comprised of an individual load mass in terms of frequency bandwidth. Also, the fact that the bandwidth of this design is readily tunable (say, by changing the mass or the spring stiffness) makes it more appealing as compared to the other two designs. As previously mentioned, one of the main objectives of the present work was to come up with an efficient energy harvesting system with a wide bandwidth for acquiring more power from the ambient vibration. The third design concept meets this objective the best.

The load mass and also the spring stiffness are both expected to play a key role in maximizing the voltage output. In practice, however, changing the load mass appears to be much easier than changing the spring stiffness. For this reason, we have decided to fix the spring stiffness and investigate the effect of the load mass only. Figures 6-8 show the measured frequency response for the more sophisticated conceptual design, in which multiple linear resonating forces are introduced to the PZT beam. We can clearly see that this system has produced three resonating frequencies. However, due to the presence of damping, the peaks are not very sharp. It is seen that the two linear resonators respond independently and, when they undergo resonance, the other resonator acts like a rigid wall causing the whole substructure behave as a cantilever beam attached to a spring-mass system at its end. This figure clearly shows that this configuration gives us more options to tune the system performance such that it can closely match our specific needs for voltage generation by choosing a good combination of load masses m_1 and m_2.

An interesting fact seen from this study was the effect of the load mass values on the frequency response of the third peak. According to Figures 6-8, increasing the load mass has quite an intensive effect on the frequency response of the substructure and would shift the first, second, and third peak to resonate in much lower frequencies.

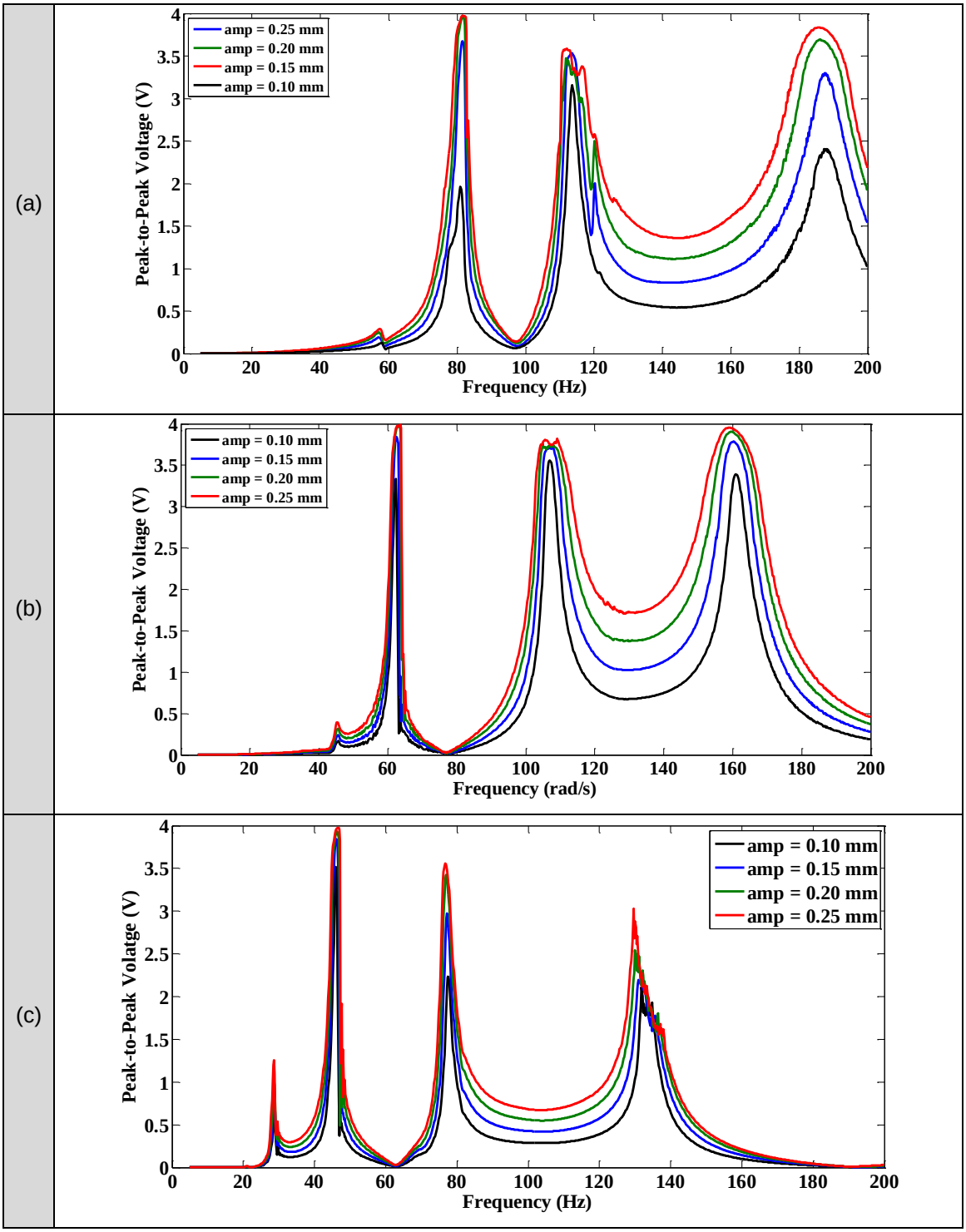

Figure 6- 8. Effect of load mass on frequency response of the design concept #3: (a) $m_l = m$, (b) $m_l = 2m$, (c)$m_l = 3m$.

It needs to be mentioned that for deriving the natural frequencies for each system, an eigenvalue study had to be made. The implementation of this eigenvalue study enables us to see if a correct frequency response has indeed been obtained from our simulations or not. This study also reveals a very interesting but predictable fact; that is: neither the natural frequency of the first nor the natural frequencies of the other two energy harvesting designs are equal to the natural frequencies of the linear resonating structures induced in the system. This is irrespective of the fact that, the Design #3 is predicted not to react in exactly the same fashion as the other two configurations. The study for the eigenvalue problem in finding the natural frequencies of the third configuration showed that the natural frequencies induced in the system exactly match the natural frequency of any of the single degree-of-freedom linear resonating structures involved within it. A plausible explanation for such an odd prediction can be attributed to the fact that the third design is equivalent to a system comprising two completely independent cantilever beams each having a spring-mass structure at one end, thereby giving rise to two very distinct natural frequencies (Figure 6-9). This appears to be the main cause for the third configuration design to be so easily tunable.

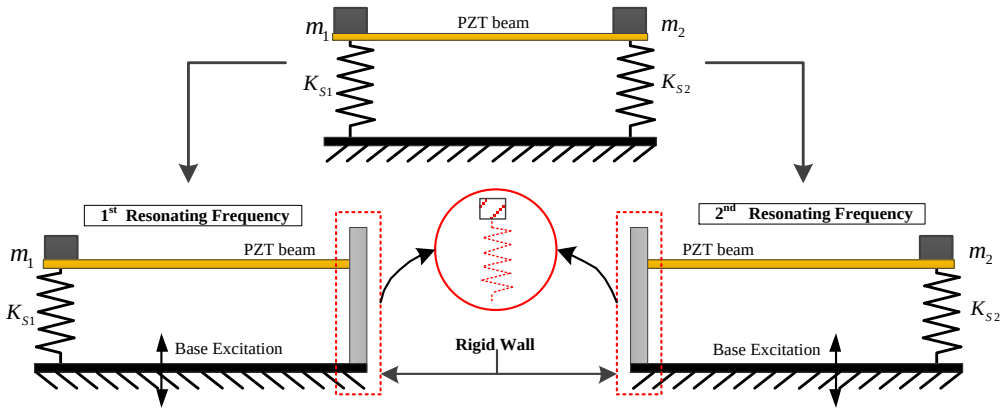

Figure 6- 9. Equivalency of the third design to two independent and separate cantilever beams

It needs to be mentioned that to avoid the difficulties introduced by damping terms, our numerical studies were carried out by assuming that no damping is involved in the system. As will be shown in the experimental section, our numerical results precisely predict the resonance frequency meaning that damping does not crucially affect the resonance frequency. Obviously, one can argue that the magnitude of the

generated voltage may not be the same if the damping terms are included in the analysis. The damping terms may also affect the frequency response of the system by broadening its bandwidth and also by lowering the magnitude of the narrow peaks observed in linear resonators. Ironically, this would result to an even more efficient energy harvesting mechanism.

Figure 6-10 clearly shows that results obtained from the prototype energy harvesting mechanism are in excellent correlation with the simulation results. That means that our analytical models are adequate to describe the dynamical behavior of the proposed energy harvesting device, at least as far as the resonance frequency is concerned. The difference between the two sets of results can again be attributed to the damping terms dropped from our theoretical analysis.

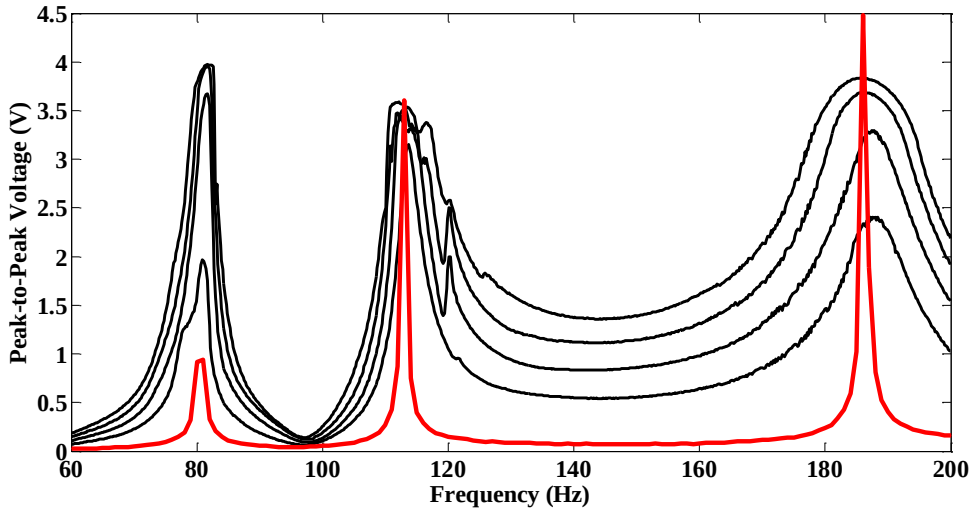

Figure 6- 10. Comparison between the numerical results (in red) and experimental results (in black) for the frequency response of the proposed energy harvester

Figure 6-11, shows the power output from the harvesting mechanism as a function of the load resistance. By assuming that the power generated is equal to v^2/R_L , the optimum load resistance was found to be 40 $k\Omega$. This would result in generating a power approximately up to 0.4 mW.

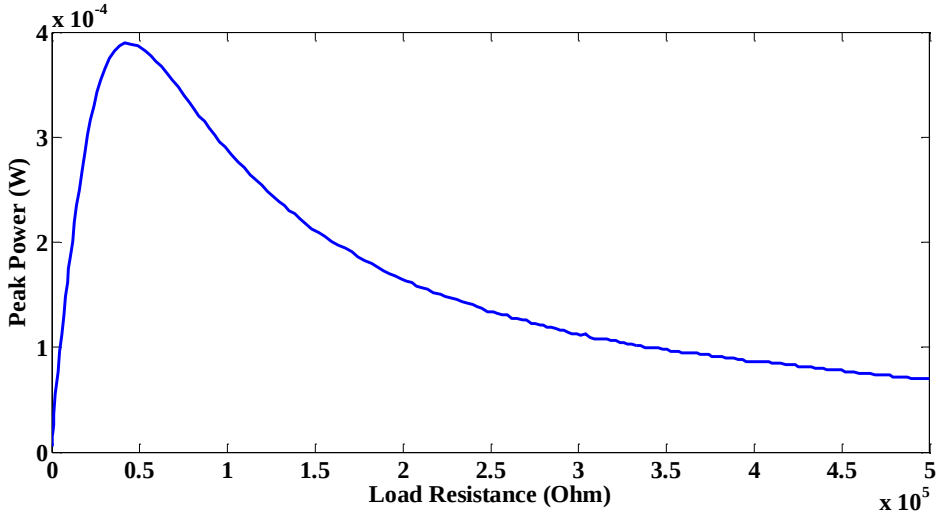

Figure 6- 11. Maximum output with respect to the load resistance

6.6. Conclusion

This chapter, presented the design, construction and test of a broad band energy harvester to capture energy from a rotary system. A combination of linear resonators was employed on a piezoelectric beam to increase the operational frequency range of vibration-based power generators. Theoretical analysis and experimental investigations was performed on a piezoelectric beam mounted on a system of linear resonating mechanisms. Different methods of mounting linear resonators to the piezoelectric beam have been studied. Using the results obtained from the simulations, it was shown that the natural frequency of a system comprising of a beam, spring and mass can easily be tuned by adjusting the load mass and/or the mechanical characteristics of the spring-mass system. In addition, it was shown that by introducing a coupled spring-mass to the PZT beam undergoing rotary motion, three different resonance frequencies can be produced. By a careful selection of the load mass, one could pre-tune the harvester in order to generate power over a broad range of frequencies. Therefore, our conceptual design is well suited to meet our purposes. In the following chapter we shall show that the conceptual design proposed would also work in rotary motion applications such as wheel hub assemblies.

7. Implementation of a Wide Band Coupled Linear Resonating Energy Harvesting System in a Smart Tire Application

As discussed in the previous chapters, the resonance frequency of traditional single spring-mass vibration-based energy harvesters is very narrow so that their efficiency is dramatically dropped when the ambient frequency is different from their natural frequency. In Chapter 6, three new piezoelectric-based energy harvesting mechanism was proposed as a remedy to the shortcoming of such harvester. Through experimental and numerical analysis, it was shown that our proposed design can truly meet this purpose.

In this chapter the energy harvesting mechanisms introduced in Chapter 6 will be tried in rotary motion applications. It will be shown that the conceptual designs exhibit the same trend in the frequency response as seen in base excitation problems. A step-by-step procedure was adopted in order to broaden the bandwidth of such energy harvesters by introducing a coupled spring-mass system attached to a PZT beam undergoing rotary motion. It is shown that the new strategies can indeed give rise to a wide-band frequency response making it possible to fine-tune their dynamical response in rotary motion applications. It is also shown that the numerical results are in good agreement with the experimental data as far as the frequency response is concerned.

In what follows, we first present the mathematical framework and the equations governing the performance of three different energy-harvesting systems. The numerical method of solution will then be described in some details. We will then proceed with describing the experimental setup and the fabrication of a prototype of our novel energy-harvesting system. The experimental setup will be used to evaluate the performance of this prototype and the validity of the numerical results. The work is concluded by highlighting its important findings.

7.1. Theoretical Formulations

Figure 7-1 shows the three design concepts proposed in this work for harvesting the vibrational energy. The device is seen to be basically comprised of a spring/mass system in which the spring is attached to the tire hub with a freely-ended flexible PZT ceramic beam attached to the mass itself. The spring/mass system undergoes an oscillatory motion as soon as the hub starts rotating. The oscillatory motion so generated makes the flexible PZT ceramic film to vibrate thereby producing the required voltage. As mentioned above, a spring/mass system (see Figure7-1-a) behaves like a linear resonator providing a narrow bandwidth in the frequency spectrum. Therefore, the voltage generated by the most basic system, as shown in Figure7-1-a, cannot provide the required voltage over a broad range of frequency domain. This shortcoming can be solved should we introduce an extra tip mass to the other end of the PZT beam (see Figure7-1-b). The combined effect of the two masses provides an extra resonating frequency, and so can widen the bandwidth by deliberately tuning the mechanical properties of the coupled spring/mass system. However, the extra tip mass can impose significant strain and stress to the substrate, particularly at high rotational velocities, causing damage to the PZT beam. To avoid this, a third conceptual design was introduced by adding another spring to the system in addition to the previous resonator system (see Figure7-1-c). This notion would result in the substructure to become more symmetric and rigid when undergoing high rotational velocities and accelerations. The proposed mechanism is shown to be easily tunable to any required frequency spectrum and is expected to harvest power in a broad and satisfactory bandwidth.

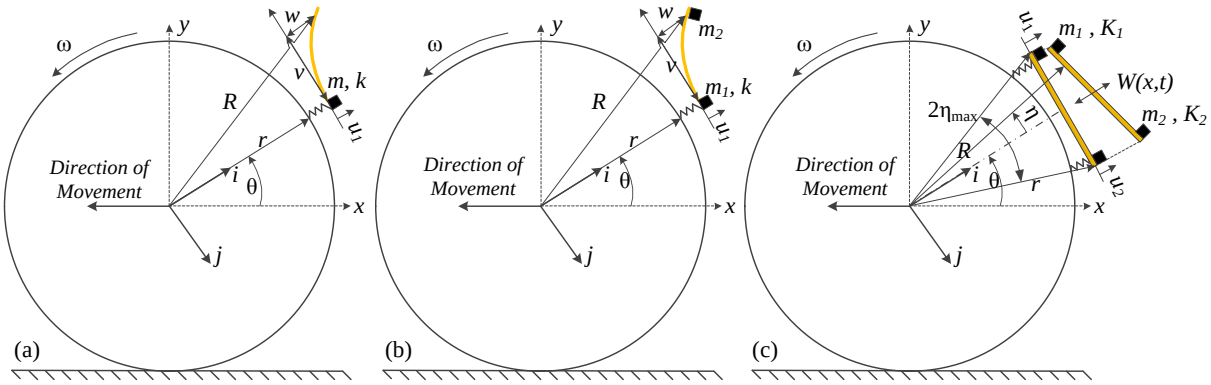

Figure 7- 1. Schematic of the novel mass/spring mechanism proposed or harvesting energy in smart tire applications: (a) the basic system, (b) the two-mass system, (c) the two-mass, two-spring system

7.1.1. Governing Equations

The mathematical modeling of the proposed mechanisms is obtained exactly as discussed in Chapter 4. Euler-Bernoulli beam equations are assumed to be valid for the PZT ceramic beam. A Lagrangian approach can then be used to develop the governing equation(s). Modeling is carried out for the case in which the tire's hub is rotating at constant angular velocity. As discussed before, for small deformations, the undamped partial differential equation describing the deflection of the PZT beam is given by,

$$EI\frac{\partial^2 w(x,t)}{\partial t^2}+\rho A\frac{\partial^4 w(x,t)}{\partial x^4}=0 \qquad (7\text{-}1)$$

where $w(x,t)$ is the beam's deflection, EI is the flexural stiffness in which E corresponds to the Young's modulus, I is the cross-sectional area moment of inertia, ρ is the mass density, and A is the cross-sectional area of the beam. As discussed briefly in the previous chapters, in order to numerically solve the above equation (subject to appropriate boundary conditions), the Rayleigh-Ritz method is employed to obtain approximate values for the fundamental natural frequency of the piezoelectric beam. Based on this method, the displacement of the beam can be approximated for N number of mode shapes. It has to be reemphasized that we have focused only on the first mode shape in our studies.

One might envisage that for having the maximum voltage output, the resonance frequency of the beam should be tuned to the frequency of the spring/mass system. This tuning can be achieved by varying the values of the mass load and/or the spring stiffness. However, our results indicate that the natural frequency of the PZT beam automatically adjusts itself to the natural frequency of the spring-mass structure. This can be attributed to the fact that the mass load, attached to the PZT beam, is much more dominant in dictating the dynamics of the whole system as compared to the PZT beam itself.

7.1.1.1. Governing Equations for Design #1

Figure 7-2 shows the geometry and parameters involved within the concept. As it can be seen in this figure, a single linear spring/mass system is attached to the inner side of a rotary hub and the PZT beam is attached to the mass.

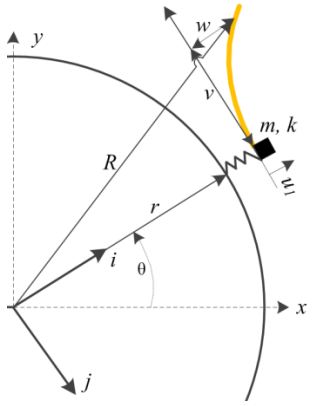

Figure 7- 2. The coordinate system used for the design concept #1

The boundary conditions pertinent to the system geometry are summarized in Table 7-1.

Table 7- 1. Boundary conditions involved in concept design #1

$\boldsymbol{Boundary\ Condition}$	$(\boldsymbol{B.C})_1: \left.\frac{d^2\phi(x)}{dx^2}\right\|_{x=l}$	$(\boldsymbol{B.C})_2: \left.\frac{d^2\phi(x)}{dx^2}\right\|_{x=0}$	$(\boldsymbol{B.C})_3: \left.\frac{d^3\phi(x)}{dx^3}\right\|_{x=l}$	$(\boldsymbol{B.C})_4: \left.\frac{d^3\phi(x)}{dx^3}\right\|_{x=0}$
$\boldsymbol{Design\ \#1}$	0	0	0	$\left(\frac{K_{s_1}}{EI} - \frac{m_1\beta^4}{\rho A}\right)\phi(x)$

Assuming u to be corresponding to the displacement of the spring/mass and $w(x,t)$ to be representing the displacement of the PZT beam, The position of any point on the PZT beam in this rotating coordinate system can be expressed as,

$$\vec{R} = (r + u + w)i' + vj' \tag{7-2}$$

Based on Figure 7-2, for the velocity of an infinitesimal segment on the PZT beam having a position R in a rotating coordinate system, we can write,

$$\dot{\vec{R}} = \left(\frac{\partial u}{\partial t} + \frac{\partial r}{\partial t} + \frac{\partial w}{\partial t}\right) i' + \dot{\theta}k' \times \left((u + r + w)i' + vj'\right) \tag{7-3}$$

which can be written as

$$\dot{\vec{R}} = \left(\dot{u} + \dot{w} - v\dot{\theta}\right)i' + (r + u + w)\dot{\theta}j' \tag{7-4}$$

where $w(x,t) = \phi(x)q(t)$ represents the coordinate system for the PZT beam, and u represents the coordinate system for the spring-mass structure. Knowing the velocity of each infinitesimal segment on the beam from the above equation and integrating along the beam, the kinetic energy of the beam can be obtained as,

$$\begin{aligned} T_{beam} = \frac{1}{2}\rho A \int_0^l \left|\dot{\vec{R}}\right|^2 dx = \frac{1}{2}\rho A(\dot{u}^2 l + \dot{q}^2 M + \frac{l^3}{3}\dot{\theta}^2 - l^2\dot{u}\dot{\theta} - l^2\dot{q}\dot{\theta}\varphi + 2\dot{u}\dot{q} \\ + (r^2 l + q^2 M + u^2 l + 2rul + 2rq\varphi + 2uq\varphi)\dot{\theta}^2) \end{aligned} \tag{7-5}$$

where M and φ are obtained from Equation 5-18. The load mass has a translational kinetic energy equal to,

$$T_{mass} = \frac{1}{2}m_1\dot{R}_{x=0}^2 = \frac{1}{2}m_1\left(\left(\dot{u} + \dot{w}(0,t)\right)^2 + \dot{\theta}^2(r + u + w(0,t))^2\right). \tag{7-6}$$

Therefore, the total potential energy U can be expressed as,

$$U = \frac{1}{2}EI\int_0^l \left(\frac{\partial^2 w}{\partial x^2}\right)^2 dx + g\rho A\left(\frac{l^2}{2}cos\theta + l(r+u+w)sin\theta\right) + \frac{1}{2}K_{s_1}u^2 + m_1 g(r+u)sin\theta \quad (7\text{-}7)$$

The generalized applied forces involved in the model, which is typically the moment induced by the piezoceramic beam was discussed in the prior sections and can be described as Equation 5-14. Applying the Lagrangian formulation for all generalized coordinates would result in $i+1$ equations for a complete dynamical simulation of the model. In matrix form, it can be expressed as,

$$C_1\begin{bmatrix}\ddot{u}\\ \ddot{q}\end{bmatrix} + C_2\begin{bmatrix}u\\ q\end{bmatrix} + C_3 = \begin{bmatrix}0\\ F(t)\end{bmatrix} \quad (7\text{-}8)$$

where C_1 is given by

$$C_1 = \begin{bmatrix}\rho Al + m_1 & \rho A\varphi + m_1\varphi_0^* \\ \rho A\varphi + m_1\varphi_0^* & \rho AM + m_1\varphi_0^*\end{bmatrix} \quad (7\text{-}9)$$

where φ_0^* corresponds to the assumed mode-shape at position $x = 0$ of the PZT beam. In Equation 7-8, C_2 corresponds to the Coriolis and centrifugal terms, with C_3 indicating the gravitational force vector; they are given as,

$$C_2 = \begin{bmatrix}K_{s_1} - \dot{\theta}^2(\rho Al + m_1) & -\dot{\theta}^2(\rho A\varphi + m_1\varphi_0^*) \\ -\dot{\theta}^2(\rho A\varphi + m_1\varphi_0^*) & EIK - \dot{\theta}^2\left(\rho AM + m_1{\phi_0^*}^2\right)\end{bmatrix} \quad (7\text{-}10)$$

$$C_3 = \begin{bmatrix}(m_1 + \rho Al)gsin\theta - m_1 r\dot{\theta}^2 \\ \rho A\varphi gsin\theta - m_1 r\dot{\theta}^2\end{bmatrix}. \quad (7\text{-}11)$$

7.1.1.2. Governing Equations for Design #2

Figure 7-3 shows the geometry and parameters involved within the concept #2. As can be seen in this figure, like the previous case, there exists a single linear spring/mass system which is attached to the inner side of a rotary hub and a PZT beam which is attached to the mass. However, another extra load mass attached on the edge of the beam has been introduced to the system substructure.

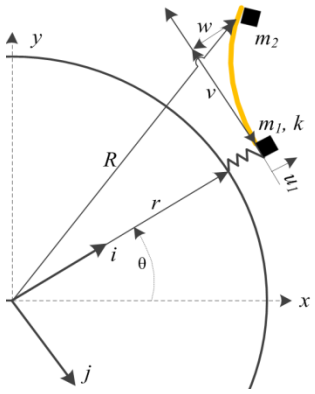

Figure 7- 3. The coordinate system used for the design concept #2

The boundary conditions involved in this case are summarized in Table 7-2.

Table 7- 2. Boundary conditions involved in concept design #2

Boundary Condition	$(\boldsymbol{B.C})_1: \left.\frac{d^2\phi(x)}{dx^2}\right\|_{x=l}$	$(\boldsymbol{B.C})_2: \left.\frac{d^2\phi(x)}{dx^2}\right\|_{x=0}$	$(\boldsymbol{B.C})_3: \left.\frac{d^3\phi(x)}{dx^3}\right\|_{x=l}$	$(\boldsymbol{B.C})_4: \left.\frac{d^3\phi(x)}{dx^3}\right\|_{x=0}$
Design #2	0	0	$-(\frac{m_2\beta^4}{\rho A})\phi(x)$	$\left(\frac{K_{s_1}}{EI}-\frac{m_1\beta^4}{\rho A}\right)\phi(x)$

Following the same procedure as shown above for the design concept #1, one could easily end up with the equations of motion for the design concept #2 and investigate the dynamical behaviour of the system. In matrix form the formulation can be shown to be the form of,

$$C_1\begin{bmatrix}\ddot{u}\\ \ddot{q}\end{bmatrix}+C_2\begin{bmatrix}u\\ q\end{bmatrix}+C_3=\begin{bmatrix}0\\ F(t)\end{bmatrix}, \tag{7-12}$$

where C_1 is given by,

$$C_1=\begin{bmatrix}\rho Al+m_1+m_2 & \rho A\varphi+m_1\varphi_0^*+m_2\varphi_l^*\\ \rho A\varphi+m_1\varphi_0^*+m_2\varphi_l^* & \rho AM+m_1\varphi_0^*+m_2\varphi_l^*\end{bmatrix}, \tag{7-13}$$

where φ_l^* corresponds to the assumed mode-shape at position $x=l$ of the PZT beam. In Equation 7-11, C_2 corresponds to the Coriolis and centrifugal terms, with C_3 indicating the gravitational force vector; they are given by,

$$C_2 = \begin{bmatrix} K_{s_1} - \dot{\theta}^2(\rho A l + m_1 + m_2) & -\dot{\theta}^2(\rho A\varphi + m_1\varphi_0^* + m_2\phi_l^*) \\ -\dot{\theta}^2(\rho A\varphi + m_1\varphi_0^* + m_2\phi_l^*) & EIK - \dot{\theta}^2\left(\rho AM + m_1\phi_0^{*2} + m_2\phi_l^{*2}\right) \end{bmatrix}, \tag{7-14}$$

$$C_3 = \begin{bmatrix} (m_1 + m_2 + \rho A l)gsin\theta - (m_1 + m_2)r\dot{\theta}^2 \\ (\rho A\varphi + m_2\phi_l^*)gsin\theta - (m_1 + m_2)r\dot{\theta}^2 \end{bmatrix}. \tag{7-15}$$

7.1.1.3. Governing Equations for Design #3

Figure 7-4 illustrates the geometry and parameters involved within the third design concept. As it can be seen in this figure, unlike the previous concepts, there exists a pair of coupled linear spring/mass systems which are attached to the inner side of a rotary hub and the PZT beam is also attached to the spring/mass system form both ends, making the system completely symmetric. Due to the complex geometry of the design concept #3, obtaining its kinetic and potential energy terms is much more complicated as compared to the other two design concepts. To that end, we have decided to rely on a new rotating co-ordinate system, as shown in Fig. 7-4.

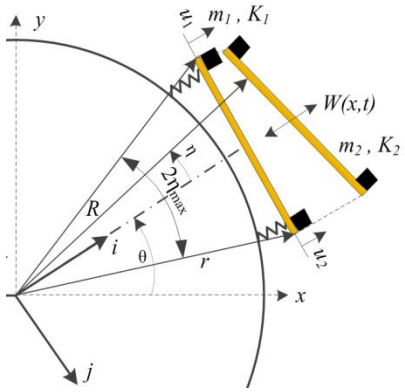

Figure 7- 4. The coordinate system used for the design concept #3

The boundary conditions involved in this design are much more sophisticated compaered to the prior concepts. Table 7-3 is a summary of the boundary conditions for this case.

Table 7- 3. Boundary conditions involved in design concept #3

Boundary Condition	$(\boldsymbol{B.C})_1: \left.\frac{d^2\phi(x)}{dx^2}\right\|_{x=l}$	$(\boldsymbol{B.C})_2: \left.\frac{d^2\phi(x)}{dx^2}\right\|_{x=0}$	$(\boldsymbol{B.C})_3: \left.\frac{d^3\phi(x)}{dx^3}\right\|_{x=l}$	$(\boldsymbol{B.C})_4: \left.\frac{d^3\phi(x)}{dx^3}\right\|_{x=0}$
Design #3	0	0	$\left(\frac{K_{s_2}}{EI} - \frac{m_2\beta^4}{\rho A}\right)\phi(x)$	$\left(\frac{K_{s_1}}{EI} - \frac{m_1\beta^4}{\rho A}\right)\phi(x)$

In the active rotating coordinate system shown in Figure 7-4 ,u_1, u_2 correspond to the displacement of the spring-mass structure, and w represents the displacement of the PZT beam. A new angular parameter η has been introduced in this coordinate system to facilitate the relations governed on the energy harvesting system. Assuming η to have a small value and $tan(\eta) \cong \eta$, the position of an infinitesimal segment on the PZT beam in this rotating coordinate system can be expressed as,

$$\vec{R} = \left[(r + u_1) + \frac{1}{2}(u_2 - u_1)\left(\frac{\eta}{\eta_{max}} + 1\right) + w(x,t)\right] i' + \left[\frac{L}{2}\left(\frac{\eta}{\eta_{max}}\right)\right] j' \tag{7-16}$$

which results to the following equations for the load masses:

$$\vec{R}_{m1} = \left(\dot{u}_1 + \dot{w}(0,t) + \frac{l}{2}\dot{\theta}\right) i' + \dot{\theta} k' \times \big(r + u_1 + w(0,t)\big) j' \tag{7-17}$$

$$\vec{R}_{m2} = \left(\dot{u}_2 + \dot{w}(l,t) - \frac{l}{2}\dot{\theta}\right) i' + \dot{\theta} k' \times \big(r + u_2 + w(l,t)\big) j'. \tag{7-18}$$

Due to the geometry of the system and knowing the radius of the hub ($r = 0.3\ m$) and length of the beam ($l = 0.046\ m$), η_{max} should then be set equal to a 0.0767 radian. Having obtained the velocity of each infinitesimal segment on the beam from the above equation, the kinetic and potential energy terms of the beam can be obtained by integrating along the beam as,

$$T_{beam} = \frac{1}{2}\rho A \int_0^l \left|\dot{\vec{R}}\right|^2 dx = \frac{1}{2} r \int_{-\eta_{max}}^{\eta_{max}} \rho A \dot{R}^2 d\eta \tag{7-19}$$

The overall potential energy of the beam can then be found by solving the equation,

$$U_{beam} = \frac{1}{2} EI \int_{-\eta_{max}}^{\eta_{max}} \big(\phi'' q(t)\big)^2 r d\eta + g\rho A r \int_{-\eta_{max}}^{\eta_{max}} h d\eta\,, \tag{7-20}$$

where h (i.e., the height of each infinitesimal segment on the beam) can be obtained as,

$$h = \left[(r + u_1) + \frac{1}{2}(u_2 - u_1)\left(\frac{\eta}{\eta_{max}} + 1\right) + w(x,t)\right] sin\theta - \left[\frac{L}{2}\left(\frac{\eta}{\eta_{max}}\right)\right] cos\theta \qquad (7\text{-}21)$$

Having applied the Lagrangian formulation for all generalized coordinates would result in the dynamic modeling of the substructure. In matrix form the equation of motion can be shown to be the form of,

$$C_1 \begin{bmatrix} \ddot{u_1} \\ \ddot{u_2} \\ \ddot{q} \end{bmatrix} + C_2 \begin{bmatrix} u_1 \\ u_2 \\ q \end{bmatrix} + C_3 = \begin{bmatrix} 0 \\ 0 \\ F(t) \end{bmatrix}, \qquad (7\text{-}22)$$

where $C_1$is given by,

$$C_1 = \begin{bmatrix} m_1 + \frac{2}{3}\rho Ar\,\eta_{max} & \frac{1}{3}\rho Ar\,\eta_{max} & m_1\phi_0^* + \rho Ar\varphi\,\eta_{max} \\ \frac{1}{3}\rho Ar\,\eta_{max} & m_2 + \frac{2}{3}\rho Ar\,\eta_{max} & m_2\phi_l^* + \rho Ar\varphi\,\eta_{max} \\ m_1\phi_0^* + \rho Ar\varphi\,\eta_{max} & m_2\phi_l^* + \rho Ar\varphi\,\eta_{max} & m_1\phi_0^* + m_2\phi_l^* + 2M\rho Ar\,\eta_{max} \end{bmatrix} \qquad (7\text{-}23)$$

As mentioned before, C_2 corresponds to the Coriolis and centrifugal terms, with C_3 indicating the gravitational force vector; they are given by,

$$C_2 = \begin{bmatrix} c_{11} & c_{12} & c_{13} \\ c_{21} & c_{22} & c_{23} \\ c_{31} & c_{32} & c_{33} \end{bmatrix}, \qquad (7\text{-}24)$$

where $C_{11}, \dots, C_{33}$ are set as follows

Coe.	***Equation***	***No.***
$\boldsymbol{c_{11}}$	$K_{s_1} - (2/3\rho A\, r\, \eta_{max} + m_1)\dot{\theta}^2$	(7-24-1)
$\boldsymbol{c_{12}}$	$-1/3\rho Ar\eta_{max}\dot{\theta}^2$	(7-24-2)
$\boldsymbol{c_{13}}$	$-(\rho Ar\varphi\eta_{max} + m_1\phi_0^*)\dot{\theta}^2$	(7-24-3)
$\boldsymbol{c_{21}}$	$-1/3\rho Ar\eta_{max}\dot{\theta}^2$	(7-24-4)
$\boldsymbol{c_{22}}$	$K_{s_2} - (2/3\rho A\, r\, \eta_{max} + m_2)\dot{\theta}^2$	(7-24-5)
$\boldsymbol{c_{23}}$	$-(\rho Ar\varphi\eta_{max} + m_2\phi_l^*)\dot{\theta}^2$	(7-24-6)
$\boldsymbol{c_{31}}$	$-(\rho Ar\varphi\eta_{max} + m_1\phi_0^*)\dot{\theta}^2$	(7-24-7)
$\boldsymbol{c_{32}}$	$-(\rho Ar\varphi\eta_{max} + m_2\phi_l^*)\dot{\theta}^2$	(7-24-8)
$\boldsymbol{c_{33}}$	$EIKr - (2MAr\varphi\eta_{max} + m_1\phi_l^{*2} + m_2\phi_0^{*2})\dot{\theta}^2$	(7-24-9)

And for C_3, following matrix is set,

$$C_3 = \begin{bmatrix} (m_1 + \rho Ar\eta_{max})gsin\theta - (m_1 r + \rho Ar^2\eta_{max})\dot{\theta}^2 \\ (m_2 + \rho Ar\eta_{max})gsin\theta - (m_2 r + \rho Ar^2\eta_{max})\dot{\theta}^2 \\ 2\rho Ar\varphi\left(gsin\theta - r\dot{\theta}^2\right) - (m_1 + m_2)r\dot{\theta}^2 \end{bmatrix} \quad (7\text{-}25)$$

The electrical model of the energy harvesting device and the coupling terms which provide us with a series of coupled electromechanical formulations was introduced in Chapter 4. We shall again use those models in order to be able to numerically predict the acquired power and voltage from the aforementioned concepts under constant rotary motion**.**

7.2. Experimental Setup

To investigate the validity of the theoretical method developed in the previous section a prototype based on our Design #3 has been fabricated.

The PZT cantilever beam is capable of acquiring voltage from any small ambient vibration or noise present. As a matter of fact one has to exercise extreme care should he/she wish to conduct experimental studies on the PZT beam and/or in the fabrication of the test bed of such experiments. These precautions become harder to meet when spinning wheel test beds are to be fabricated and designed. Any sort of eccentricity seen in the test bed result wobbling motions on the wheel hub (in both vertical and horizontal directions), causing unaccounted vibration sources for the PZT beam.

Before fabricating a delicate test bed, 3D models were created for each part of the test bed assembly and 2D maps were subsequently imported for fabrication in order to achieve high orders of tolerance and precision. The software used for this matter was Solidworks which is a 3D program used for designing mechanical parts. Figure 7-5 shows the rendered version of our spinning wheel test bed specifically designed for this project.

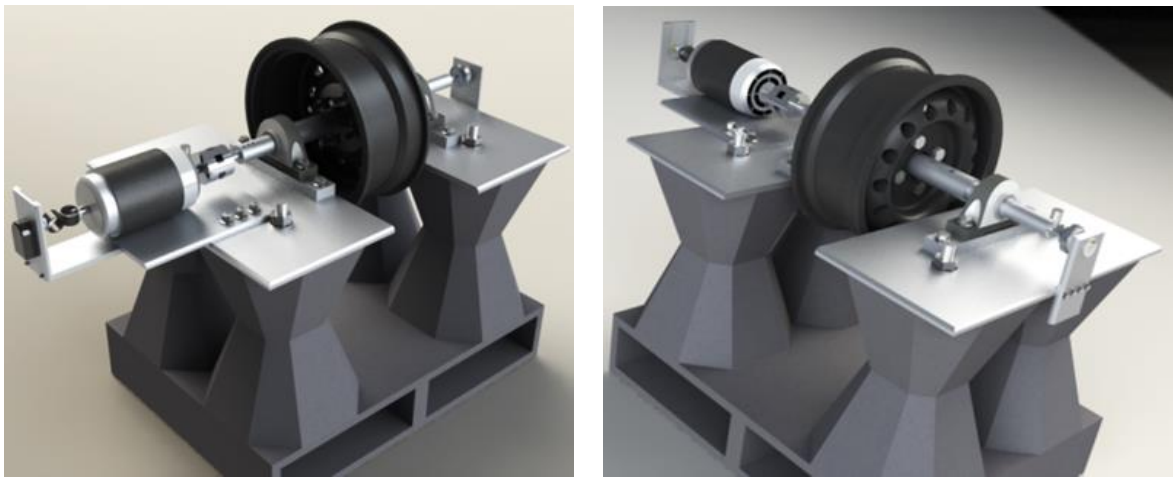

Figure 7- 5. The CAD model of the spinning wheel experimental setup designed

Figure 7-6 shows a CAD sketch view of the final design to be mounted on the inner part of the tire hub. As mentioned before, the PZT beam which was used in practice was a *V25W Volture* piezoelectric film manufactured by *MIDE Inc.* To boost its mechanical strength, we have decided to mount it on four parallel springs at each corner (see Figure 7-6). For our numerical investigation, the stiffness coefficients of the springs used in this study were set to be 45 N/m.

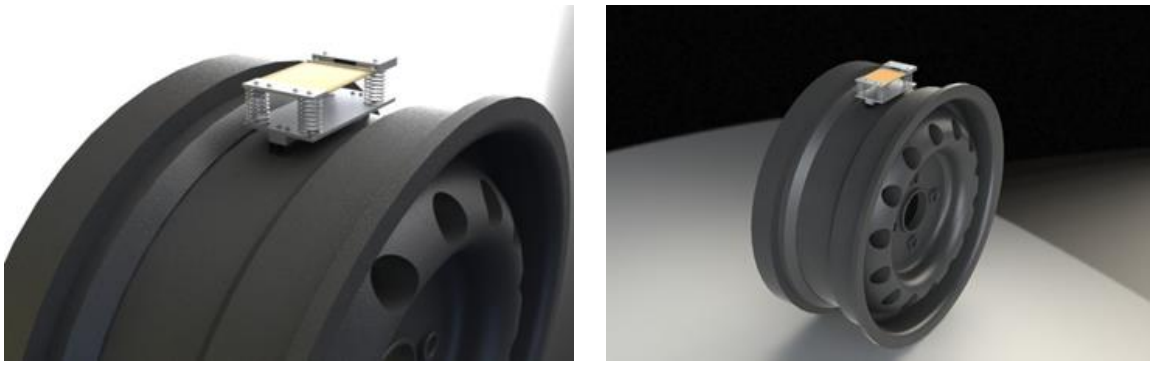

Figure 7- 6. The CAD model of the proposed energy harvesting mechanism mounted inside the wheel's hub

The performance of the prototype energy-harvesting system, as shown in Fig. 7-7, will be tested on a spinning wheel experimental setup specifically designed and fabricated for this application. It is worth mentioning that the test-bed was assembled all from scratch and all the parts incorporated within the test bed were individually

fabricated in the most delicate way by the author itself. In fact, fabricating a rotary Test-bed was one of the concerns of this project. As shown in Figure 7-7, the hub in which the PZT energy harvester is mounted, is coupled to a DC motor. For better alignment between the motor's shaft and the wheel's shaft, specific flexible spider shaft couplings have been introduced to the system. In order to precisely measure the rotary position, the DC motor has been coupled with an Encoder using ultra-flex double looped coupler. Numerical differentiation from the output data of the encoder is also used to obtain the angular velocity (in rad/s). The rotary nature of our experimental setup forced us to use a rotary coupling mechanism known as slip-ring (made by *Michigan Scientific Corp.,* S-series, End of shaft slip-ring). This device readily transfers electric current from the rotating wheel assembly to a stationary unit, enabling data to be easily acquired from the rotary device. For the purpose of a precise data acquisition, the electric output voltage from the energy harvester is connected to a *NI USB-6229 DAQ* module, optimized for superior accuracy at fast sampling rates. It has to be mentioned that the whole setup has been mounted on a rigid and bulky concrete block in order to damp out any sort of unwanted vibration and noise present in the ambient.

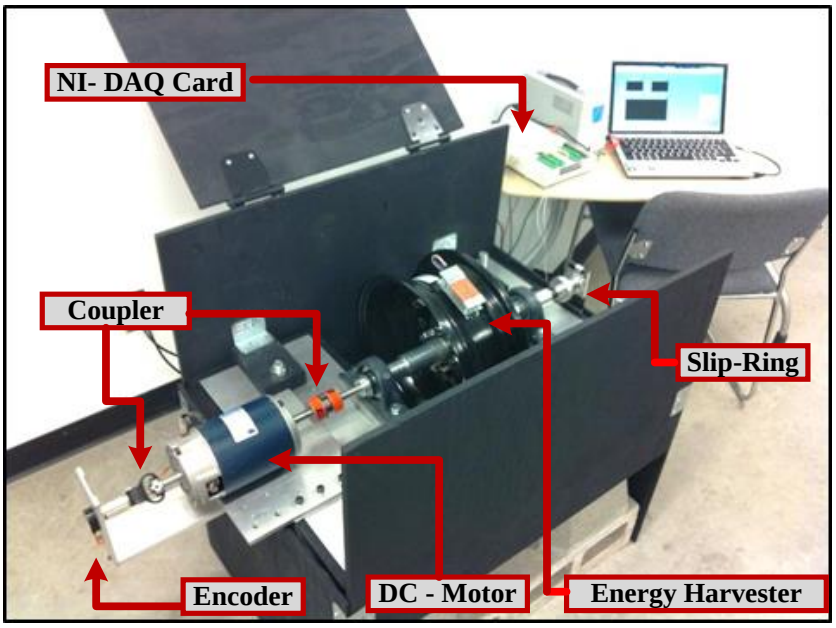

Figure 7- 7. The spinning wheel experimental setup used in this study

The setup is used to not only predict the accurate amount of the power produced by the PZT generator, but also to identify the resonance frequencies of the substructure

where the amplitude of the voltage and power generated by the device are highest. The experimental setup shown in Fig. 7-7 is easily capable of reaching angular velocities of the order of 120 rad/s.For an ordinary vehicle having wheel radii of 40 cm, this would amount to a linear velocity close to 173 km/h. In practice, the experimental data were gathered by sweeping the angular velocity of the wheel from 10 to 120 rad/s. An open circuit voltage was then monitored. Further studies were conducted by introducing a series of resistive loads in order to adjust it to an optimum value for the purpose of maximum power generation. The software interface which was used for acquiring data out of the NI DAQ card was LABVIEW which is a user-friendly, visual programming language. Figure 7-8 shows the block diagram developed and manipulated for acquiring the output voltage from the PZT beam as well as the data collected from the encoder for measuring the true rotational velocity of the tire.

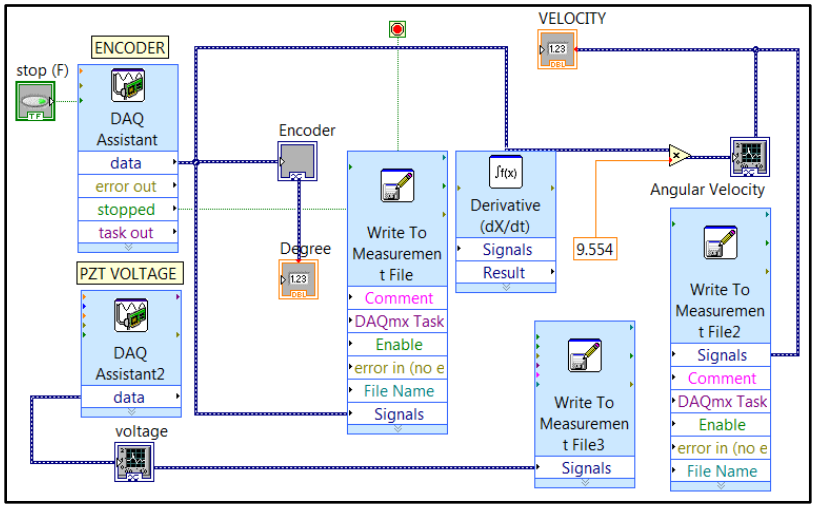

Figure 7- 8. LABVIEW block diagram used for data acquisition

7.3. Numerical Results and Discussions

In this section, we will present a comparison between our numerical and experimental results obtained for the proposed energy harvesting design as depicted in Figure 7-4. We start with presenting the numerical results first. As it is well-established in the literature [2], in order to maximize the voltage output of piezoelectric beams, the structure should be excited at its first natural frequency. The load mass and also the

spring stiffness are both expected to play a key role in maximizing the voltage output. In practice, however, changing the load mass appears to be much easier than changing the spring stiffness. For this reason, we have decided to fix the spring stiffness and investigate the effect of the load mass only. Figure 7-15 shows the effect of the load mass on the peak-to-peak voltage output of the device based on Design #1. As it can be seen in this figure, by increasing the mass, the frequency shifts to lower values.

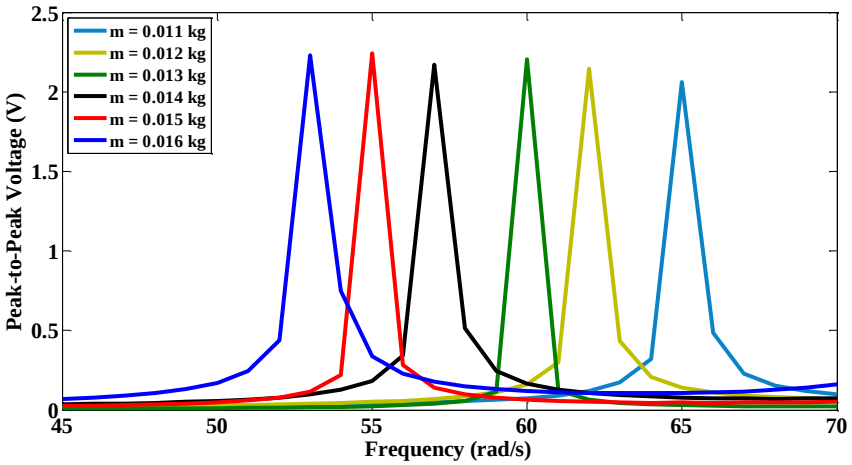

Figure 7- 9. Effect of the load mass of the peak-to-peak voltage

7.3.1. Effect of Load mass on the Generated Voltage

Figure 7-16 shows the effect of the load mass on the single spring/mass energy harvesting system. This figure clearly indicates that variation of the load mass has no significant effect on the magnitude of the acquired voltage from the proposed energy harvesting mechanism. This behaviour could be attributed to the presence of the spring mass in the energy harvesting system. Any change in the load mass would affect the dynamics of the spring rather than the PZT beam itself. As such, the PZT beam would undergo roughly the same strain resulting in virtually the same voltage generation.

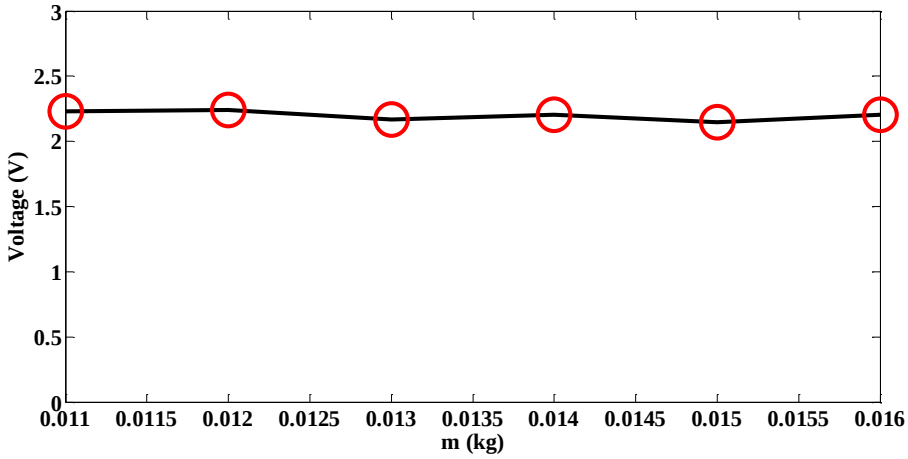

Figure 7- 10. Effect of the load mass on the magnitude of acquired voltage

7.3.2. Effect of Load Mass on the Frequency Response

Figure 7-17 shows the effect of tip mass on the resonance frequency. This figure shows that by increasing the tip mass from $11gr$ to values up to $16gr$, the resonance frequency of the energy harvesting substructure drops from roughly $65\,rad/s$ to values around $52\,rad/s$.

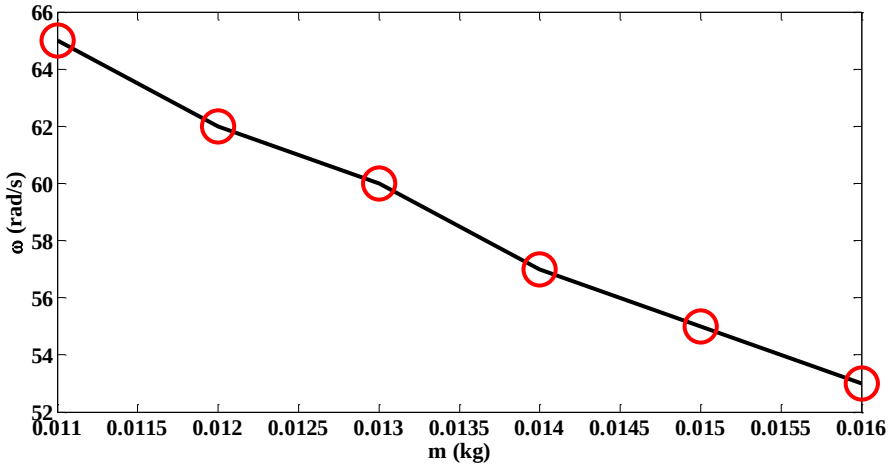

Figure 7- 11. Effect of load mass on the resonance frequency

A comparison between the proposed energy harvesting system with the very first design (i.e., the one which consists of a tangent cantilever beam fixed to the rotary hub), reveales the fact that utilizing a linear resonating structure within the harvesting system

could be beneficial as to the fact that it causes the harvesting mechanism to become more tunable than the cantilever beam as the frequency deviates more easily when the load mass values vary. Figure 7-18, clearly shows the frequency response of two individual mechanisms under the same load mass condition. According to this figure, introducing a linear resonator to the system not only shifts the deviation in changing the frequency response of the harvesting mechanism but also, for the case which both mechanisms have a same load mass value, the harvesting mechanism with a resonating structure, creates resonating frequencies much lower than. In general , one could state that incorporating a linear resonator in the system enhances the performance by ; firstly, increasing the level of deviation in frequency tuning resulting to a more tunable system, and secondly, decreasing the magnitude and order of resonance frequencies induced in the harvesting mechanism.

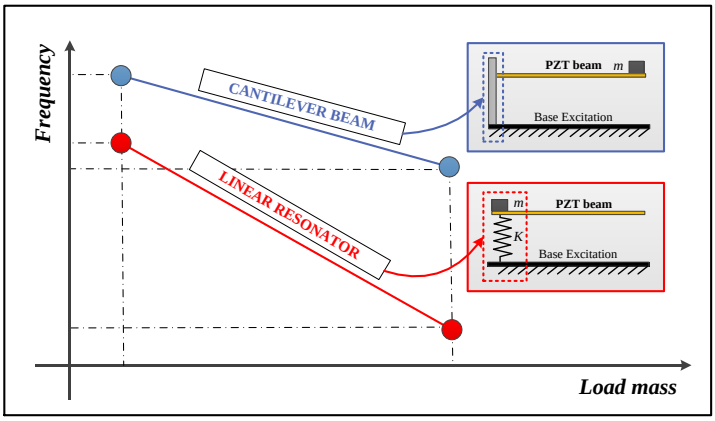

Figure 7- 12. Comparison of harvesting mechanism with and without a linear resonating structure.

7.3.3. Comparison between Proposed Concepts as a Matter of Frequency Response

Figure 7-18 shows a comparison between the frequency responses of the three design concepts depicted schematically in Figure 7-1. As it can be seen in this figure, the first design configuration results in just one very narrow resonating frequency (see Figure 7-19-a). On the other hand, the second configuration gives rise to two resonance frequencies (see Figure 7-19-b) resulting in a broader bandwidth. the third design concept also renders two resonance frequencies covering a broad bandwidth for voltage

generation. Obviously, the third configuration (as depicted schematically in Figure 7-19-c) is advantageous to the other two designs in terms of frequency tuning. As previously mentioned, one of the main objectives of the present work was to come up with an efficient energy harvesting system having a broad bandwidth for acquiring power from the ambient vibration and also a mechanism which would be easy tuning. The third design concept easily meets our purpose. It needs to be mentioned that for obtaining the natural frequencies for each system, an eigenvalue study had to be made. The implementation of this eigenvalue study enabled us to see if a correct frequency response has indeed been obtained from our simulations or not.

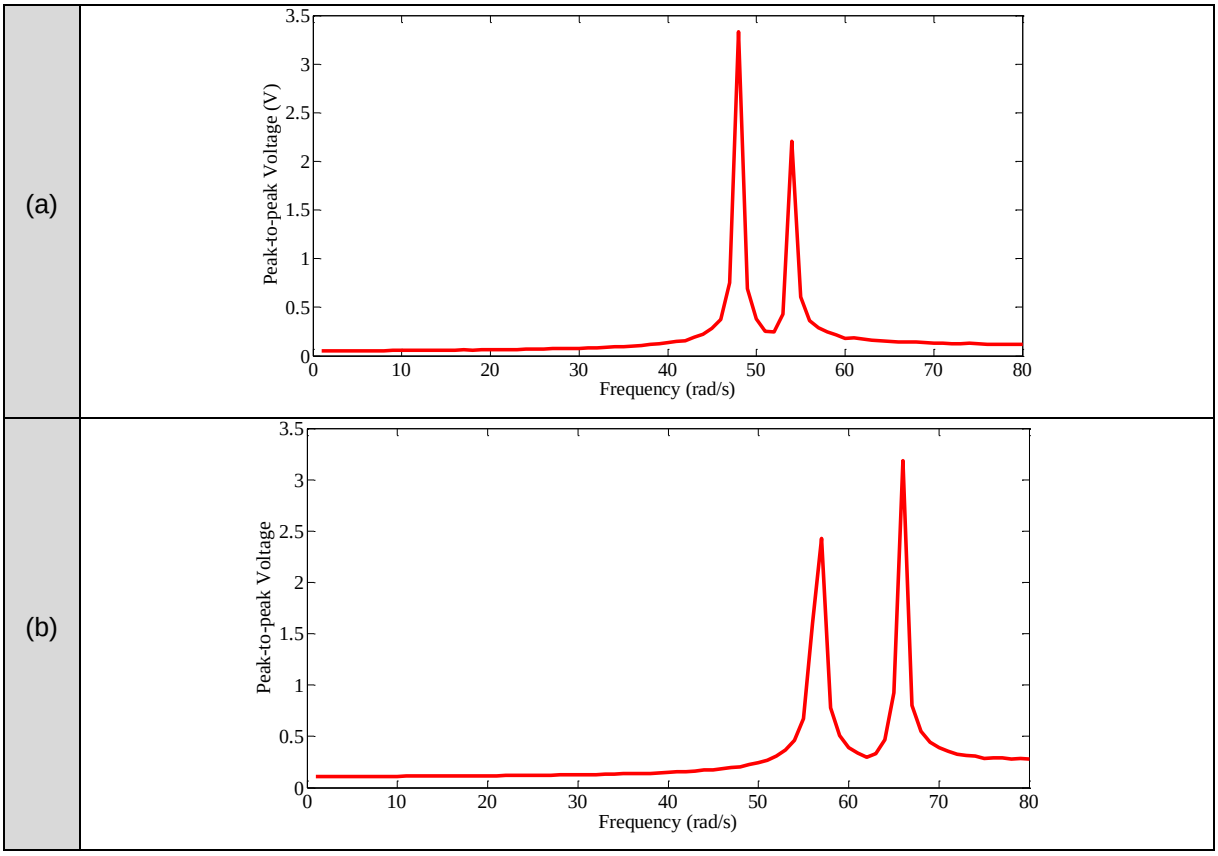

Figure 7- 19. Frequency response of the conceptual designs showing the effect of using coupled linear resonators: (a) design concept #2, and (b) design concept #3

Figure 7-20, shows how the load masses m_1 and m_2, and the spring stiffness K_1 and K_2 affect the frequency response of the more complicated design #3 system. This figure clearly shows that this configuration gives us more flexibility to tune the system performance such that it can closely match our specific needs for voltage generation by choosing a good combination of load masses m_1 and m_2.

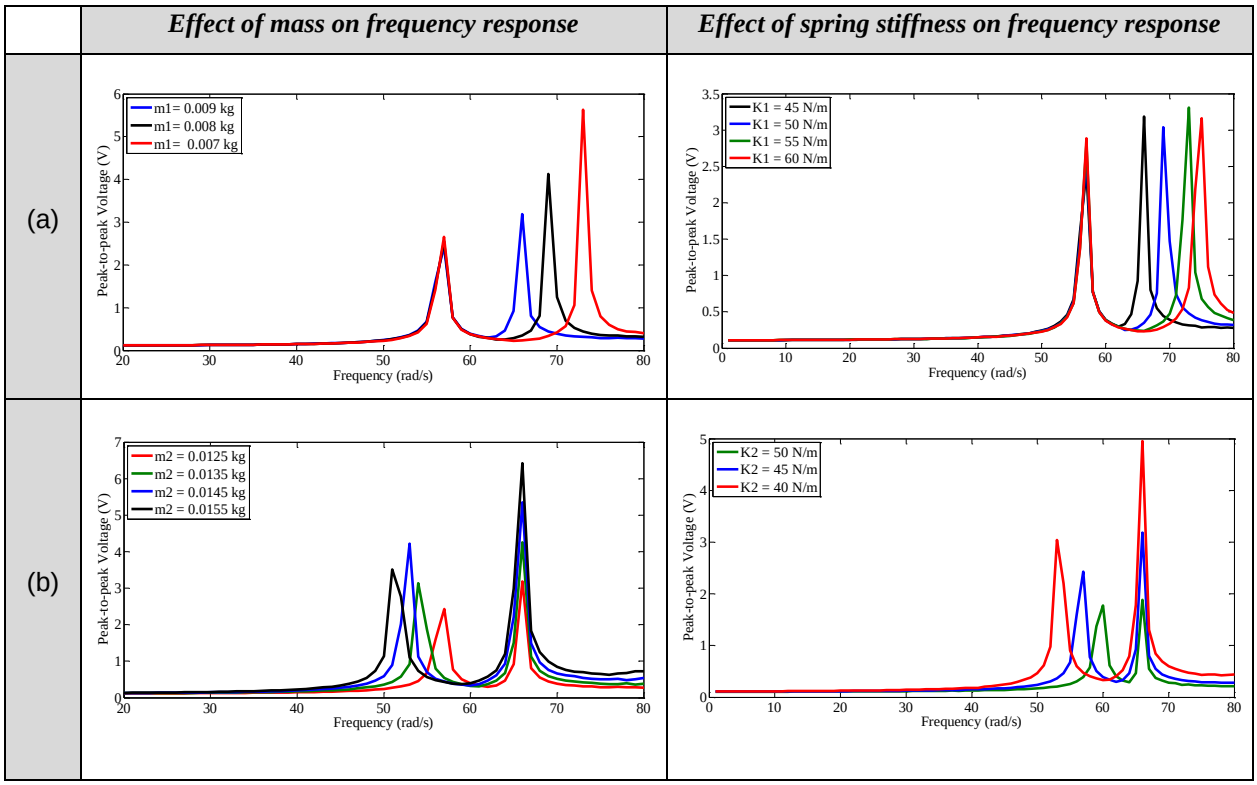

Figure 7-20. Effect of load mass m_1 and m_2 on frequency response of concept #3

It is worth mentioning that to avoid the difficulties caused by the damping terms, our numerical studies were carried out by assuming that no damping is involved in the system. As will be shown in the experimental section, our numerical results precisely predict the resonance frequency meaning that damping does not crucially affect the resonance frequency. Obviously, one can argue that the magnitude of the generated voltage may not be the same if the damping terms are included in the analysis. The damping terms may also affect the frequency response of the system by broadening its bandwidth and also by lowering the magnitude of the narrow peaks observed in linear resonators.

According to Figure 7-20 one can conclude that by incorporating an appropriate and delicately tuned coupled spring mass system, in this case ($m_1 = 0.01, m_2 = 0.0125\ kg,$ and $K_{spring} = 45\ N/m$), a broad bandwidth of voltage could be generated from the rotational motion of the wheel which fortunately covers the moderate range of the driving speed of commercial vehicles. According to Figure 14, the system is capable of harvesting energy in between the frequencies of 55 to 65 rad/s, which accordingly means this system efficiently harvests power when a vehicle having a wheel radii of $0.4\ m$ is driving with a pace of 70 to 80 $km/h.$ Conclusion and Recommendations

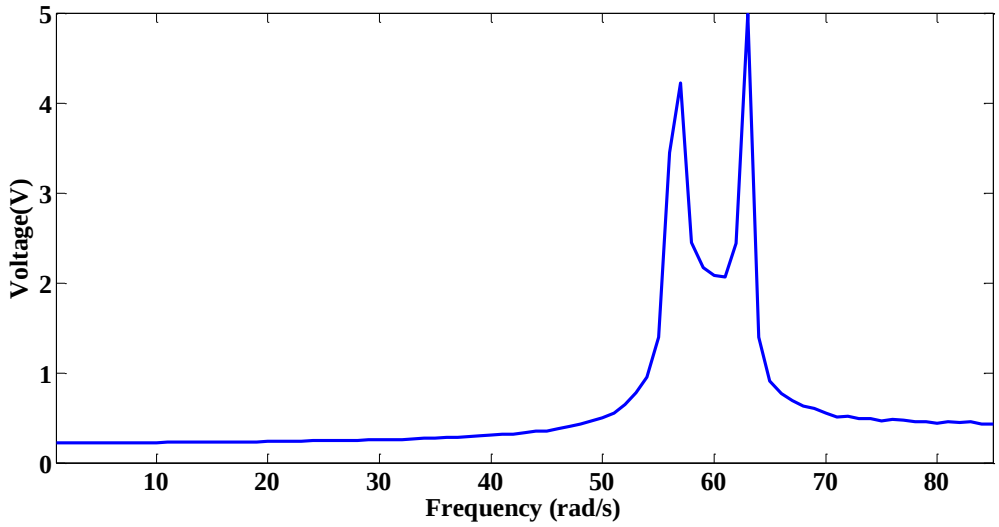

Figure 7- 13. Wide bandwidth voltage generation within the average range of vehicles driving speed

7.4. Experimental Results

The experimental procedure was done by fastening the prototype with four identical springs having a stiffness value of 45 N/m . The decision of utilizing such soft springs was based upon the factor of tuning the prototype to reach to its resonance in much lower angular velocities, close to the driving speeds of typical commercial vehicles [29]. Due to structural characteristics, the prototype was initially equipped by tip mass values of 0.018 and 0.008 kg, at each end. For the purpose of investigating the effect of tip mass values on the resonance behavior of the system, two extra small identical tip masses having a value of 0.00225 kg were added to the system later on.

Figure 7-21 clearly shows the effect of load mass value on the frequency response for conceptual design #3 when a linear resonating force is introduced to the PZT beam. This process was done by attaching small load masses of equal value having a weight of $m = 0.00225\ kg$ and keeping the tip-mass and spring stiffness value constant in each case. As predicted from our theoretical section, the third design is capable of producing three resonating frequencies; nevertheless, we have only relied on the first two resonating frequencies since the third resonance occurs at high frequencies (say close to 105rad/s), which is in fact way much higher than the average driving speed of any commercial vehicle. This leads us to say that the third frequency does not fit within our desired working frequency range. Moreover, because now damping terms are involved, the peaks are not very sharp. Based on these results it can be concluded that by increasing the load mass value the two narrow resonating frequencies get closer to each other resulting in a wider bandwidth with a more sufficient voltage generation. Based on our observations, the two linear resonators responded independently and when they undergo resonance, the other resonator acts like a rigid wall causing the whole substructure behave as a cantilever beam attached to a spring-mass system at its end.

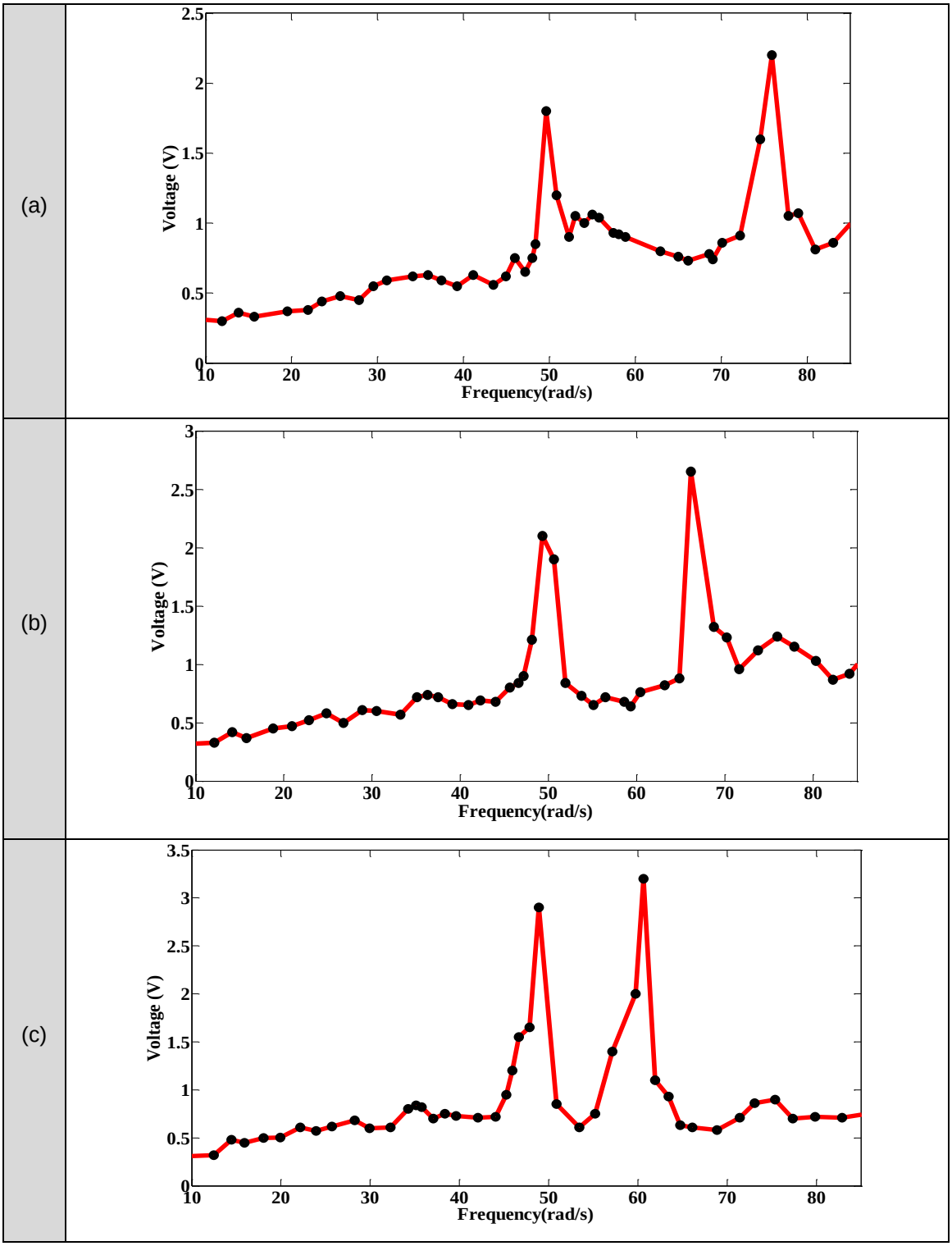

Figure 7- 14. Effect of the load mass on the frequency response for design concept #3 (experimental data): (a) $m_l = 0$, (b) $m_l = m, (c)$ $m_l = 2m$

Figure 7-22 clearly shows that results obtained from our prototype energy harvesting mechanism are in excellent correlation with the simulation results. That means that our analytical model is capable to describe the dynamical behavior of the proposed energy harvesting device, at least as far as the resonance frequency is concerned. The difference between the two sets of results can again be attributed to the damping terms dropped from our theoretical analysis.

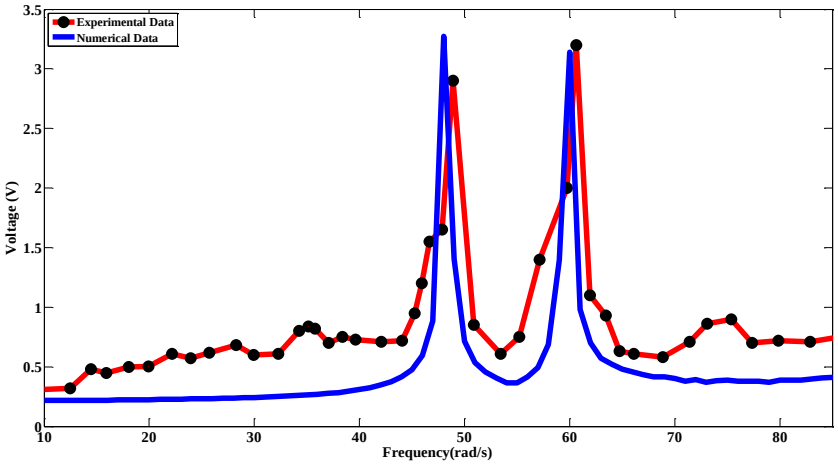

Figure 7- 15. Comparison between the numerical results (in red) and experimental results (in blue) for the frequency response of the energy harvester

8. Conclusion and Recommendations

This thesis demonstrated that it is possible to broaden the working range of mass/spring energy harvester for rotary motion applications. The piezoelectric energy harvester designed and fabricated in this work was mainly comprised of a piezoelectric beam being employed by a combination of linear resonators (spring/mass structures), on the beam. The objective was to increase the operational frequency range of vibration-based power generators. The proposed energy harvester was then mounted on a rotary hub undergoing a constant rotational motion inducing an active harmonic force on the harvesting substructure. This harmonic force (which is driven by the gravitational force acting on the load mass) was the main cause of producing vibration and thereby generating voltage within the PZT beam. We started with deriving a robust mathematical (electromechanical) model for the harvester which had to be solved numerically in order to predict the magnitude of power generated and acquired form the energy harvester substructure. In the analytical, we relied on ~~n~~ the Euler-Bernoulli and assumed mode theorem in order to obtain a distributed model for the PZT beam. The coupled partial differential equations so-obtained were solved using the method of separation of variables. Assumed mode shapes of the PZT beam were estimated by invoking valid and active boundary conditions for the beam and a Lagrangian approach was then used for deriving the governing equations of motion. By introducing nonlinear correction factors to the governing equations, the modified model was used to investigate possible nonlinear behaviour of the system. Also, by introducing the coupling terms of the piezoelectric transducer, the equations of motion were used to estimate the acquired voltage. Subsequently, based on Kirchhoff law, an electrical circuit equation consisting of a resistive load was derived which was then used for predicting the generated power; it also enabled finding the optimal resistance value for maximum power acquisition.

Theoretical analysis and experimental investigations were both performed on a piezoelectric beam mounted on a system of linear resonating mechanisms. Experimental

studies were performed on a unique spinning wheel/hub test-bed, specifically designed and fabricated for this project. Three different methods of mounting linear resonators to the piezoelectric beam have been studied. Using the results obtained from the simulations, *it was shown that the natural frequency of a system comprising beam spring and mass can easily be tuned by changing the load mass and/or the mechanical characteristics of the spring-mass system*. In addition, it was shown that by introducing a coupled spring-mass to the PZT beam going through rotary motion, three different resonance frequencies can be produced. By a careful selection of the load mass, one could pre-tune the harvester such that it can generate power over a broad range of frequencies.

Based on the results obtained in this work, one can conclude that the proposed energy- harvesting design can effectively be used to power up wireless sensors used in rotary motion applications such as those used in smart tires.

8.1. Recommendations for Future Research

Based upon the comprehensive numerical and experimental analysis executed on the proposed energy harvesting mechanism comprised of linear resonating structures, the following recommendations could be advocated for possible future studies:

- The energy harvested by the mechanism described in this work may not be adequate for many applications. Should we consider storing energy coming out from the harvester over a period of a long time, one could simply utilize such harvesters over wider applications. Therefore, efficient storage of the acquired power can be an important research topic in the ensuing works.
- Although we have shown that manipulating and introducing linear resonating structures would increase the bandwidth of power acquisition, yet, the final proposed conceptual design investigated in this study is in fact quite a bulky prototype and as a safety and liability point of view, may not be qualified to be mounted in real cars. As a matter of fact, further studies should be done in order to scale down the size of the proposed prototype to much smaller dimensions

without decreasing its effectiveness. It is anticipated that MEMS technology may play a crucial role in designing the next generation of our energy harvester.

- Increasing the damping of the system would have a definite positive effect on extending the bandwidth of power acquisition with the price being that it causes a slight drop in the magnitude of power generated. An optimization method need be developed to find the best damping for the harvesting system.

References

[1] K. Mnif, “A smart tire pressure monitoring system,” in *A smart tire pressure monitoring system*, 2001, vol. 0, pp. 40–46.

[2] T. Yamagiwa, “Development of a tire pressure monitoring system for motorcycles ,” *JSAE Review*, vol. 24, no. 4, pp. 495–496, Oct. 2003.

[3] C. B. Williams and R. B. Yates, “Analysis Of A Micro-electric Generator For Microsystems,” in *International Solid-State Sensors and Actuators Conference - TRANSDUCERS ’95*, 1995, vol. 1, pp. 369–372.

[4] S. Roundy, P. K. Wright, and J. Rabaey, “Analysis Of A Micro-electric Generator For Microsystems,” *Computer Communications*, vol. 26, no. 11, pp. 1131–1144, Jul. 2003.

[5] S. Priya, “Advances in energy harvesting using low profile piezoelectric transducers” *Journal of Electroceramics*, vol. 19, no. 1, pp. 167–184, Mar. 2007.

[6] A. Chandrakasan, R. Amirtharajah, J. Goodman, and W. Rabiner, “Trends in low power digital signal processing,” in *ISCAS ’98. Proceedings of the 1998 IEEE International Symposium on Circuits and Systems (Cat. No.98CH36187)*, vol. 4, pp. 604–607.

[7] S. Meninger, J. O. Mur-Miranda, R. Amirtharajah, A. Chandrakasan, and J. H. Lang, “Vibration-to-electric energy conversion,” *IEEE Transactions on Very Large Scale Integration (VLSI) Systems*, vol. 9, no. 1, pp. 64–76, Feb. 2001.

[8] W. R. Davis and N. Zhang, “A Design Environment for High-Throughput Low-Power Dedicated Signal Processing Systems ,” vol. 37, no. 3, pp. 420–431, 2002.

[9] F. Khameneifar and S. Arzanpour, “Energy Harvesting From Pneumatic Tires Using Piezoelectric Transducers,” in *Smart Materials, Adaptive Structures and Intelligent Systems, Volume 1*, 2008, vol. 2008, no. 43314, pp. 331–337.

[10] P. D. Mitcheson, E. M. Yeatman, G. K. Rao, A. S. Holmes, and T. C. Green, “Human and Machine Motion for Wireless Electronic Devices,” vol. 96, no. 9, pp. 1457–1486, 2008.

[11] C. B. Williams and R. B. Yates, “Analysis of a micro-electric generator for microsystems,” *Sensors and Actuators A: Physical*, vol. 52, no. 1–3, pp. 8–11, Mar. 1996.

[12] S. P. Beeby, M. J. Tudor, and N. M. White, “Energy harvesting vibration sources for microsystems applications ,” *Measurement Science and Technology*, vol. 17, no. 12, pp. R175–R195, Dec. 2006.

[13] T. von Buren, P. D. Mitcheson, T. C. Green, E. M. Yeatman, A. S. Holmes, and G. Troster, “Optimization of inertial micropower Generators for human walking motion ,” *IEEE Sensors Journal*, vol. 6, no. 1, pp. 28–38, Feb. 2006.

[14] D. Zhu, M. J. Tudor, and S. P. Beeby, “Strategies for increasing the operating frequency range of vibration energy harvesters: a review ,” *Measurement Science and Technology*, vol. 21, no. 2, p. 022001, Feb. 2010.

[15] J. Gireas, H. Oh, M. Huzmezan, and H. Sane, “Patent US8030807 - Electromechanical energy harvesting system,” U.S. Patent US 2009/0079200 A1.

[16] G. Piazza, R. Abdolvand, G. K. Ho, and F. Ayazi, “Voltage-tunable piezoelectrically-transduced single-crystal silicon micromechanical resonators,” *Sensors and Actuators A: Physical*, vol. 111, no. 1, pp. 71–78, Mar. 2004.

[17] D. Scheibner, J. Mehner, D. Reuter, T. Gessner, and W. Dötzel, “A spectral vibration detection system based on tunable micromechanical resonators,” *Sensors and Actuators A: Physical*, vol. 123–124, no. null, pp. 63–72, Sep. 2005.

[18] T. Petropoulos, E. Yeatman, and D. Mitcheson, “coupled resonators for power generation and sensing,” in *Micromechanics Europe*, 2004, pp. 63–72.

[19] S. M. Shahruz, “Design of mechanical band-pass filters for energy scavenging,” *Journal of Sound and Vibration*, vol. 292, no. 3–5, pp. 987–998, May 2006.

[20] F. Khameneifar, M. Moallem, and S. Arzanpour, “Modeling and Analysis of a Piezoelectric Energy Scavenger for Rotary Motion Applications,” *Journal of Vibration and Acoustics*, vol. 133, no. 1, p. 011005, 2011.

[21] “A Distributed, Wireless MEMS Technology for Condition Based Maintenance,” Apr. 1996.

[22] V. Raghunathan, C. Schurgers, and M. B. Srivastava, “Energy-aware wireless microsensor networks,” *IEEE Signal Processing Magazine*, vol. 19, no. 2, pp. 40–50, Mar. 2002.

[23] P. B. Koeneman, I. J. Busch-Vishniac, and K. L. Wood, “Feasibility of micro power supplies for MEMS,” *Journal of Microelectromechanical Systems*, vol. 6, no. 4, pp. 355–362, 1997.

[24] G. Görge, M. Kirstein, and R. Erbel, “Microgenerators for Energy Autarkic Pacemakers and Defibrillators: Fact or Fiction,” *Herz*, vol. 26, no. 1, pp. 64–68, Feb. 2001.

[25] R. Amirtharajah and A. P. Chandrakasan, “Self-powered signal processing using vibration-based power generation,” *IEEE Journal of Solid-State Circuits*, vol. 33, no. 5, pp. 687–695, May 1998.

[26] S. A. Jacobson and A. H. Epstein, “ An informal survey of power MEMS,” *Micro-Mechanical Engineering, ISMME (Japan)*, 2003.

[27] P. Glynne-Jones, M. J. Tudor, S. P. Beeby, and N. M. White, “An electromagnetic, vibration-powered generator for intelligent sensor systems,” *Sensors and Actuators A: Physical*, vol. 110, no. 1–3, pp. 344–349, Feb. 2004.

[28] C. Alippi and C. Galperti, “An Adaptive System for Optimal Solar Energy Harvesting in Wireless Sensor Network Nodes,” *IEEE Transactions on Circuits and Systems I: Regular Papers*, vol. 55, no. 6, pp. 1742–1750, Jul. 2008.

[29] V. Raghunathan, A. Kansal, J. Hsu, J. Friedman, and M. Srivastava, “Design considerations for solar energy harvesting wireless embedded systems,” in *IPSN 2005. Fourth International Symposium on Information Processing in Sensor Networks, 2005.*, 2005, pp. 457–462.

[30] I. Stark, “Thermal Energy Harvesting with Thermo Life,” in *International Workshop on Wearable and Implantable Body Sensor Networks (BSN’06)*, pp. 19–22.

[31] T. Huesgen, P. Woias, and N. Kockmann, “Design and fabrication of MEMS thermoelectric generators with high temperature efficiency,” *Sensors and Actuators A: Physical*, vol. 145–146, no. null, pp. 423–429, Jul. 2008.

[32] M. Ferrari, V. Ferrari, M. Guizzetti, D. Marioli, and A. Taroni, “ Characterization of Thermoelectric Modules for Powering Autonomous Sensors,” in *2007 IEEE Instrumentation & Measurement Technology Conference IMTC 2007*, 2007, pp. 1–6.

[33] D. M. Rowe and G. Min, “Evaluation of thermoelectric modules for power generation,” *Journal of Power Sources*, vol. 73, no. 2, pp. 193–198, Jun. 1998.

[34] S. P. Beeby, M. J. Tudor, and N. M. White, “Energy harvesting vibration sources for microsystems applications,” *Measurement Science and Technology*, vol. 17, no. 12, pp. R175–R195, Dec. 2006.

[35] M. El-hami, P. Glynne-Jones, N. M. White, M. Hill, S. Beeby, E. James, A. D. Brown, and J. N. Ross, “Design and fabrication of a new vibration-based electromechanical power generator,” *Sensors and Actuators A: Physical*, vol. 92, no. 1–3, pp. 335–342, Aug. 2001.

[36] C. B. Williams, C. Shearwood, M. A. Harradine, P. H. Mellor, T. S. Birch, and R. B. Yates, “Development of an electromagnetic micro-generator,” *IEE Proceedings - Circuits, Devices and Systems*, vol. 148, no. 6, p. 337, 2001.

[37] A. P´erez-Rodr´ıguez, C. Serre, N. Fondevilla, C. Cereceda, J. R. Morante, E. J, and J. Montserrat, “ELECTROMAGNETIC INERTIAL GENERATOR FOR VIBRATIONAL ENERGY SCAVENGING COMPATIBLE WITH Si TECHNOLOGY,” in *Eurosensors XIX (Barcelona, Spain)*, 2005, vol. 1, pp. 57–60.

[38] S. P. Beeby, M. J. Tudor, E. Koukharenko, N. M. White, T. O. Donnell, C. Saha, S. Kulkarni, and S. Roy, “Micromachined silicon Generator for Harvesting Power from Vibrations,” in *Transducers (Seoul, Korea)*, 2005, pp. 780–783.

[39] F. Khameneifar, “VIBRATION-BASED PIEZOELECTRIC ENERGY HARVESTING SYSTEM FOR ROTARY MOTION THESIS SUBMITTED IN PARTIAL FULFILLMENT OF In the,” Simon Fraser University, 2011.

[40] R. S, W. P, and P. K, “Micro-electrostatic vibration-to-electricity converters,” in *IMECE*, 2002, pp. 1–10.

[41] S. J. Roundy, “Energy scavenging for wireless sensor nodes with a focus on vibration to electricity conversion,” University of California, Berkeley, 2003.

[42] J. Twiefel, “Energy Harvesting Technologies,” S. Priya and D. J. Inman, Eds. Boston, MA: Springer US, 2009.

[43] L. Tang, Y. Yang, and C. K. Soh, “Toward Broadband Vibration-based Energy Harvesting,” *Journal of Intelligent Material Systems and Structures*, vol. 21, no. 18, pp. 1867–1897, Dec. 2010.

[44] S. Roundy and Y. Zhang, “Toward Self-tuningAdaptive Vibration Based Micro-generators,” in *Smart Materials, Nano-, and Micro-Smart Systems*, 2005, pp. 373–384.

[45] E. S. Leland and P. K. Wright, “Resonance tuning of piezoelectric vibration energy scavenging generators using compressive axial preload,” *Smart Materials and Structures*, vol. 15, no. 5, pp. 1413–1420, Oct. 2006.

[46] Y. Hu, H. Xue, and H. Hu, “A piezoelectric power harvester with adjustable frequency through axial preloads,” *Smart Materials and Structures*, vol. 16, no. 5, pp. 1961–1966, Oct. 2007.

[47] V. R. Challa, M. G. Prasad, and F. T. Fisher, “A coupled piezoelectric–electromagnetic energy harvesting technique for achieving increased power output through damping matching,” *Smart Materials and Structures*, vol. 18, no. 9, Sep. 2009.

[48] R. B. MacCurdy, T. Reissman, and E. Garcia, “Energy Management of Multi-Component Power Harvesting Systems,” in *The 15th International Symposium on: Smart Structures and Materials & Nondestructive Evaluation and Health Monitoring*, 2008, pp. 692809–692809–12.

[49] Y. Shu, “3 Energy Harvesting Technologies,” S. Priya and D. J. Inman, Eds. Boston, MA: Springer US, 2009.

[50] Z. Yang, “Connected Vibrating Piezoelectric Bimorph Beams as a Wide-band Piezoelectric Power Harvester,” *Journal of Intelligent Material Systems and Structures*, vol. 20, no. 5, pp. 569–574, Nov. 2008.

[51] J.-Q. Liu, H.-B. Fang, Z.-Y. Xu, X.-H. Mao, X.-C. Shen, D. Chen, H. Liao, and B.-C. Cai, “A MEMS-based piezoelectric power generator array for vibration energy harvesting,” *Microelectronics Journal*, vol. 39, no. 5, pp. 802–806, May 2008.

[52] S. Priya, “Modeling of electric energy harvesting using piezoelectric windmill,” *Applied Physics Letters*, vol. 87, no. 18, p. 184101, Oct. 2005.

[53] A. Abid, “A FEM-BEM interactive coupling for modeling the piezoelectric health motioring systems,” vol. 8, no. May, pp. 305–334, 2011.

[54] J. Yang, *An Introduction to the Theory of Piezoelectricity*. Boston 2005: .

[55] H. Baudry, “Screen Printing Piezoelectric Devices,” *Microelectronics International*, vol. 4, no. 3, pp. 71–74, Dec. 1987.

[56] N. M. White and J. D. Turner, “Thick-film sensors: past, present and future,” *Measurement Science and Technology*, vol. 8, no. 1, pp. 1–20, Jan. 1997.

[57] A. J. Lovinger, “ Ferroelectric polymers.,” *Science (New York, N.Y.)*, vol. 220, no. 4602, pp. 1115–21, Jun. 1983.

[58] J. F. Nye, Ed., *Physical Properties of Crystals*. Oxford University Press.

[59] M. Umeda, K. Nakamura, and S. Ueha, “Analysis of the Transformation of Mechanical Impact Energy to Electric Energy Using Piezoelectric Vibrator,” *Japanese Journal of Applied Physics*, vol. 35, no. Part 1, No. 5B, pp. 3267–3273, May 1996.

[60] B. Cavallier, H. Nouira, E. Foltête, L. Hirsinger, and S. Ballandras, “Energy Storage Capacity of Vibrating Structure: application to a Shock System », Symposium on Design, Test, Integration and Packaging of MEMS/MOEMS (DTIP 2005), Montreux, Switzerland.,” *Proceedings of DTIP 2005*, 2005.

[61] T. Starner, “Human-powered wearable computing,” *IBM Systems Journal*, vol. 35, no. 3.4, pp. 618–629, 1996.

[62] F. Antaki, G. Bertocci, C. Green, A. Nadeem “A gait powered autologous battery charging system for artificial organs,” *Artif. Internal Organs*, vol. J. 41 M588, pp. 588–595, 1995.

[63] J. Kymissis, C. Kendall, J. Paradiso, and N. Gershenfeld, “Parasitic power harvesting in shoes,” in *Digest of Papers. Second International Symposium on Wearable Computers (Cat. No.98EX215)*, pp. 132–139.

[64] N. S. Shenck and J. A. Paradiso, “Energy scavenging with shoe-mounted piezoelectrics,” *IEEE Micro*, vol. 21, no. 3, pp. 30–42, 2001.

[65] S. R. Platt, S. Farritor, K. Garvin, and H. Haider, “The Use of Piezoelectric Ceramics for Electric Power Generation Within Orthopedic Implants,” *IEEE/ASME Transactions on Mechatronics*, vol. 10, no. 4, pp. 455–461, Aug. 2005.

[66] M. J. Ramsay and W. W. Clark, “Piezoelectric Energy Harvesting for Bio MEMS Applications,” in *SPIE’s 8th Annual International Symposium on Smart Structures and Materials*, 2001, pp. 429–438.

[67] S. Roundy and P. K. Wright, “A piezoelectric vibration based generator for wireless electronics,” *Smart Materials and Structures*, vol. 13, no. 5, pp. 1131–1142, Oct. 2004.

[68] M. Tamura, “Piezo-Electric Bimorph Element,” U.S. Patent Patent JP63268279A.

[69] “IEEE Standard on Piezoelectricity,” p. 0_1, 1988.

[70] Q. M. Wang and L. E. Cross, “Constitutive equations of symmetrical triple layer piezoelectric benders.,” *IEEE transactions on ultrasonics, ferroelectrics, and frequency control*, vol. 46, no. 6, pp. 1343–51, Jan. 1999.

[71] W. Timoshenko S, Young D H, *Vibration problems in engineering*, 1974th ed. New York: ohn Wiley and Sons.

[72] H. P. Lee, “Dynamic stability of a rotating cantilever beam with in-plane base acceleration,” *Engineering Computations*, vol. 14, no. 4, pp. 471–480, Jan. 1997.

[73] H. Yoo and S. Shin, “VIBRATION ANALYSIS OF ROTATING CANTILEVER BEAMS,” vol. 212, pp. 807–828, 1998.

[74] M. Kermani, M. Moallem, and R. Patel, “Parameter selection and control design for vibration suppression using piezoelectric transducers,” *Control Engineering Practice*, vol. 12, no. 8, pp. 1005–1015, Aug. 2004.

Appendices

Appendix A.

Detail Design and Description of the experimental setup

In this section a detailed description of each component used in the experimental setup will be addressed. Figure A-1 shows a 3D rendered view of the test bed designed and fabricated for our studies. Figure A-1 and A-2 annotates each component which was used in fabricating the test bed. The following tables give a brief description of each part:

Table A-1 – Part Descriptions

Part No.	*Part Name*	*Description*
1	*Encoder*	*Detecting the angular position and angular velocity*
2	*Shaft Coupling 1*	*Eliminate large amount of parallel/angular misalignment*
3	*Shaft Coupling 2*	*Reduce shock and compensate minor misalignment*
4	*Shaft Slip – Ring*	*Acquiring Data out of rotary motion applications*

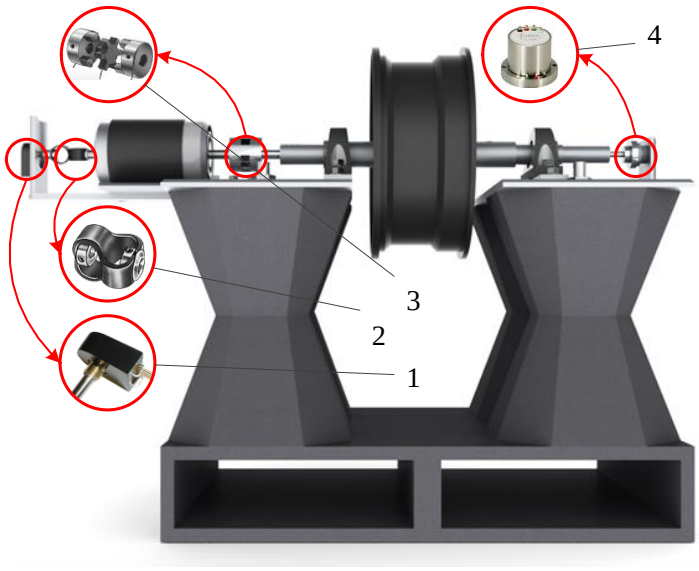

Figure A- 1. Front view of the Experimental setup (3D CAD model)

Table A-2 - Part Descriptions (continue)

Part No.	*Part Name*	*Description*
1	*Lug – Nuts*	*Securing the wheel to threaded wheel studs*
2	*Wheel*	13 *inch steel wheel*
3	*Disk*	*Assuring concentricity between the shaft and the wheel*
4	*Adapter*	*Disk connector to shaft*
5	*Wheel studs*	*Reassuring concentricity and connecting The disk to the wheel*

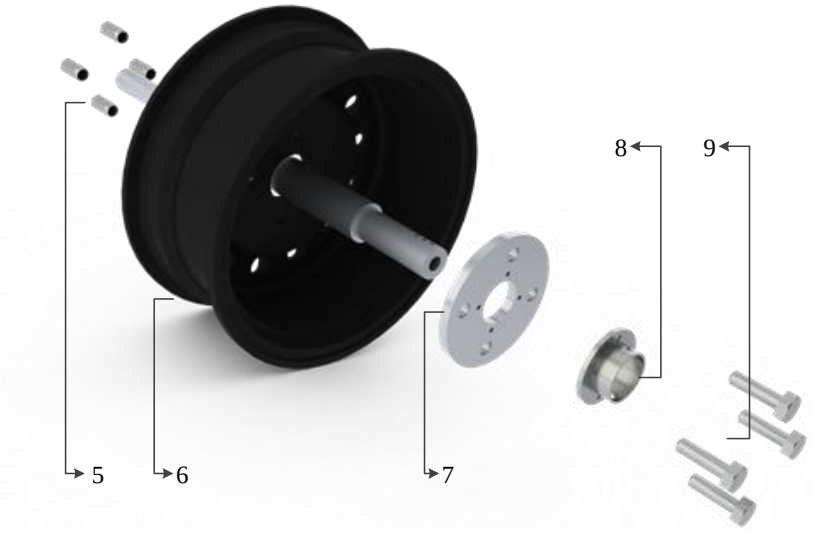

Figure A- 2. Exploded view of the wheel-shaft assembly

The shaft of this test-bed (which was particularly designed and fabricated for this project) was equipped with a hole, having a depth of half the length of the shaft. The hole was needed for transferring the wirings coming out from the slip-ring of the energy harvesting prototype (which was mounted on the wheel). The schematic of the shaft has been shown in Figure A-3.

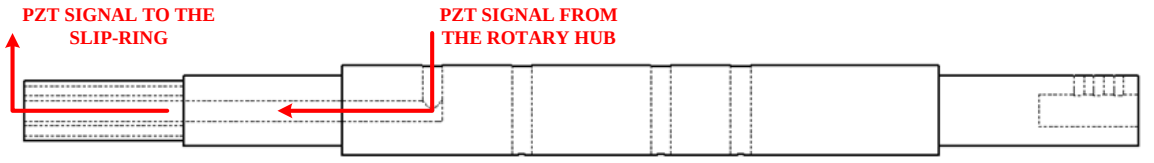

Figure A- 3. Section view of the fabricated shaft

Appendix B.

MATLAB CODE and Conjoined SIMULINK Block Diagram

The coupled partial differential equations in this project were numerically simulated by the aid of SIMULINK. Figure B-1 shows the block diagram used for our numerical analysis. Using the ODE 45 technique, the SIMUINK block diagram calculated the response of the system in the time domain and a sophisticated conjoined MATLAB code was then introduced to convert the time domain into frequency and acquire the frequency response of the problem by sweeping the frequency in between the desired limits.

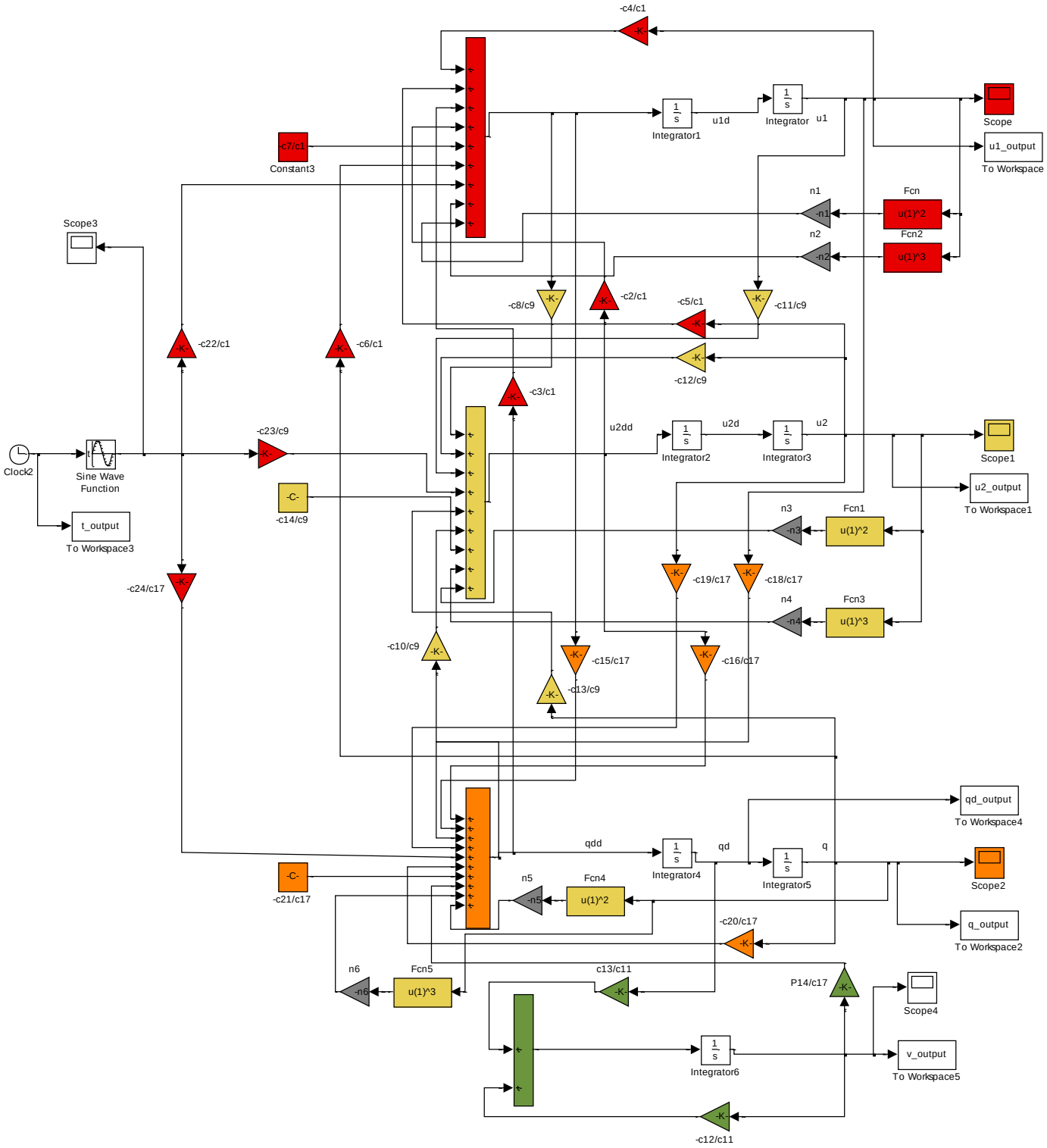

Figure B- 1. SIMULINK block diagram

Frequency Sweep Code

```
clear;
clc
%% MAX Rad/s a car can reach is 120 (simulation range for FFT)
m1=0.010;
m2=0.0125;

K1=45;
K2=45;
%% FINDING COE's OF THE MODE SHAPE EQUATION
%%%%%%%%%%%%%%%%%%%%%%%%%%%%%%%%%%%%%%%%%%%%%%%%%%%%%%%%%%%%%%%%%%%%%%%
beta=Beta(m1, m2, K1, K2); % Export from Beta.m
%%%%%%%%%%%%%%%%%%%%%%%%%%%%%%%%%%%%%%%%%%%%%%%%%%%%%%%%%%%%%%%%%%%%%%%
rho=1980;
L=0.046;
E=24*10^9;
b=0.03327;
h=0.000762;
A=b*h;
zita=0.01;
r=0.35;
g=9.813;
phimax=0.0728;
I=(b*h^3)/12;
%--------------------
H1=(K1/(E*I))-(m1*beta^4)/(rho*A);
H2=(K2/(E*I))-(m2*beta^4)/(rho*A);
%--------------------
%% FINDING a1 a2 a3 a4 ( Assumption: a2=1 )
a2=1;
a4=a2;

d1=-beta^3*cos(beta*L)-H2*sin(beta*L);
d2=beta^3*sin(beta*L)-H2*cos(beta*L);
d3=beta^3*cosh(beta*L)-H2*sinh(beta*L);
d4=beta^3*sinh(beta*L)-H2*cosh(beta*L);

a1=-a2*(d2+d4+((d3*2*H1)/beta^3))/(d1+d3);
a3=2*a2*H1/beta^3+a1;

C=[a1 a2 a3 a4]
%% FINDING COE's RELATED TO LAGRANGIAN
syms x
p=a1*sin(beta*x)+a2*cos(beta*x)+a3*sinh(beta*x)+a4*cosh(beta*x);
PHI=double(L*int(p,x,0,1))
fi=PHI;
M=double((L*int(p^2,x,0,1)))
d2=diff(p,x,2);
K=double((L*int(d2^2,x,0,1)))
d1=(diff(p,x,1))
```

```
%% PLOT THE MODE SHAPE
x=0:0.01:1/L;
p=a1*sin(beta*x)+a2*cos(beta*x)+a3*sinh(beta*x)+a4*cosh(beta*x);
dp_L=a1*b*cos(b*L)-a2*b*sin(b*L)+a3*b*cosh(b*L)+a4*b*sinh(b*L)
dp_0=a1*b+a3*b
%% PZT PROPERTIES
R=1000000;
d31=-190;
e33=1700;
Cp=(e33*b*L)/h;
APZT=(-(d31*E*b*h)/2)*dp_L;
KPZT=E*b*d31*h/14;
FPZT=KPZT*((dp_0 - dp_L));
%% SIMULINK FREQUENCY SWEEP
i=0;
forteta=1:1:120
i=i+1
freq(i)=teta;

pAr=rho*A*r;
    EIK=E*I*K;

    c1= m1 + (2*pAr*phimax)/3;
    c2= (pAr*phimax)/3;
    c3= fi*pAr*phimax;
    c4= K1 - (2*pAr*phimax*teta^2)/3;
    c5=-(pAr*phimax*teta^2)/3;
    c6=-fi*pAr*phimax*teta^2;
    c7= - pAr*phimax*r*teta^2;

    c8= (pAr*phimax)/3;
    c9=  m2 + (2*pAr*phimax)/3;
    c10= fi*pAr*phimax;
    c11= -(pAr*phimax*teta^2)/3;
    c12= K2 - (2*pAr*phimax*teta^2)/3;
    c13= -fi*pAr*phimax*teta^2;
    c14= - pAr*phimax*r*teta^2;

    c15= fi*pAr*phimax;
    c16= fi*pAr*phimax;
    c17= 2*M*pAr*phimax;
    c18= -fi*pAr*phimax*teta^2;
    c19= -fi*pAr*phimax*teta^2;
    c20= EIK*r - 2*M*pAr*phimax*teta^2;
    c21= - 2*fi*pAr*phimax*r*teta^2;

    c22=(g*m1+ g*pAr*phimax);
    c23=(g*m2+ g*pAr*phimax);
    c24=2*fi*g*pAr*phimax;
    p11=Cp;
    p12=1/(2*R);
    p13=APZT;
    p14=FPZT;
% nonlinearity terms
```

```
epsilon=0.11;
    alpha1Q=2000; %Quadratic Spring 1 COE
    alpha1C=10; %Cubic Spring 1 COE
    alpha2Q=2000; %Quadratic Spring 2 COE
    alpha2C=10; %Cubic Spring 2 COE

    n1=epsilon*alpha1Q/c1; %Quadratic Spring 1
    n2=epsilon^2*alpha1C/c1; %Cubic Spring 1
    n3=epsilon*alpha2Q/c9; %Quadratic Spring 2
    n4=epsilon^2*alpha2C/c9; %Cubic Spring 2
    n5=0;
    n6=0

sim('simulink_run');
FFTv(i)=0.2+3.5*max((v_output));
end
holdon
plot(freq, FFTv,'r');
omega_beam=sqrt((beta^4*E*I)/(rho*A))
omega1=sqrt(K1/m1)
omega2=sqrt(K2/m2)
```

Code for Finding The Mode Shape (BETA)

```
function [B1]=Beta(m1, m2, K1, K2)
format long
i=0;
j=0;
for B=2:0.001:30
    i=i+1;
    BB(i)=B;

    H1=K1/(E*I)-(m1*B^4)/(rho*A);
    H2=K2/(E*I)-(m2*B^4)/(rho*A);

    M=[0 -B^2 0 B^2;
        B^3 H1 -B^3 H1;
        -B^2*sin(B*L) -B^2*cos(B*L) B^2*sinh(B*L) B^2*cosh(B*L);
        H2*sin(B*L)+B^3*cos(B*L)          H2*cos(B*L)-B^3*sin(B*L)
H2*sinh(B*L)-B^3*cosh(B*L) H2*cosh(B*L)-B^3*sinh(B*L)];
    An(i)=(det(M));
    MM(i+1)=sign(An(i));

if abs(MM(i+1)-MM(i))==2 && j<3
        j=j+1;
        B1(j)=B;
break;
end
end
[B2, B3]=min(An);
```